UNIVERSIDADE FEDERAL DE PERNAMBUCO
CENTRO DE TECNOLOGIA E GEOCIÊNCIAS
DEPARTAMENTO DE ENGENHARIA CIVIL E AMBIENTAL
PROGRAMA DE PÓS-GRADUAÇÃO EM ENGENHARIA CIVIL

THAÍS TENÓRIO DOURADO

FINITE ELEMENT MODELS FOR NONLINEAR ANALYSIS OF ONSHORE WIND TURBINES' EMBEDDED-RING FOUNDATIONS

Recife
2022

THAÍS TENÓRIO DOURADO

FINITE ELEMENT MODELS FOR NONLINEAR ANALYSIS OF ONSHORE WIND TURBINES' EMBEDDED-RING FOUNDATIONS

Dissertation submitted to Universidade Federal de Pernambuco's Graduate Program in Civil Engineering as partial fulfilment of the requirements to obtain the Master of Civil Engineering Title.

Knowledge area: Structural Engineering.

Supervisor: Prof. Dr. Paulo Marcelo Vieira Ribeiro.

Recife

2022

Catalogação na fonte:
Bibliotecária Sandra Maria Neri Santiago, CRB-4 / 1267

D739f Dourado, Thaís Tenório.
Finite element models for nonlinear analysis of onshore wind turbines' embedded-ring foundations / Thaís Tenório Dourado. – 2022.
146 f.: il., fig., tabs.

Orientador: Prof. Dr. Paulo Marcelo Vieira Ribeiro.
Dissertação (Mestrado) – Universidade Federal de Pernambuco. CTG. Programa de Pós-Graduação em Engenharia Civil. Recife, 2022.
Inclui referências.

1. Engenharia civil. 2. Fundações de aerogeradores. 3. Modelos em elementos finitos. 4. Virola. 5. Comportamento não-linear do concreto. I. Ribeiro, Paulo Marcelo Vieira (Orientador). II. Título.

UFPE

624 CDD (22. ed.) BCTG/2022-430

THAÍS TENÓRIO DOURADO

FINITE ELEMENT MODELS FOR NONLINEAR ANALYSIS OF ONSHORE WIND TURBINES' EMBEDDED-RING FOUNDATIONS

Dissertation submitted to Universidade Federal de Pernambuco's Graduate Program in Civil Engineering, Centre of Technology and Geosciences, as partial fulfilment of the requirements to obtain the Master of Civil Engineering Title. Concentration area: Structural Engineering.

Approved in: 24/08/2022.

EXAMINATION COMMITTEE

Prof. Dr. Paulo Marcelo Vieira Ribeiro (supervisor)
Universidade Federal de Pernambuco

Prof. Dr. Tiago Ancelmo de Carvalho Pires de Oliveira (internal examiner)
Universidade Federal de Pernambuco

Prof. Dr. Raúl Darío Durand Farfán (external examiner)
Universidade de Brasília

Prof. Dr. Fernando Artur Nogueira Silva (external examiner)
Universidade Católica de Pernambuco

ACKNOWLEDGEMENTS

Firstly, I want to thank God for this opportunity and the strength to pursue and fulfil it.

Next, I wish to thank my supervisor, Prof. Paulo Marcelo Vieira Ribeiro, who is still my most significant example of dedication to teaching and research. Thank you for your kindness and patience and for sharing your enthusiasm for the new and your passion for learning.

Then, I wish to thank my family. My parents, Tânia and Marcos, for teaching me the value of knowledge and dedication and unconditionally supporting me. Aline, whose pragmatism I often lack, for helping me balance wishful thinking and reality. Ighor, for always believing in me more than I do. Lype, for the unconditional love and company. Thank you to all family members and amazing friends for understanding my absence and supporting my work.

Furthermore, I am grateful that this study was financed in part by the Coordenação de Aperfeiçoamento de Pessoal de Nível Superior - Brasil (CAPES) - Finance Code 001.

Lastly, I acknowledge UFPE for being my home for so many years. A special appreciation to all faculty workers, especially Andrea, for the availability and support whenever needed.

ABSTRACT

Wind turbines' share in the energy industry continues to grow, its renewable energy source status deeming it attractive due to environmental policies established worldwide. Most of these turbines are onshore installations and are supported by steel towers connected to reinforced concrete foundations through embedded rings, a type of structure with reported damages to the tower-foundation interface. This study presents simulation procedures for this kind of foundation concerning their structural behaviour. Emphasis is given to developing finite element models with the aid of the finite element software Abaqus. Four 3D models were developed with differing numerical assumptions so that it would be possible to understand how each affected the structural behaviour and which model better fitted the purpose of investigating the concrete around the bottom flange of the steel ring. The assumptions cover nonlinear elastic supports, contact interaction and nonlinear concrete behaviour. This research provides a valuable resource since the knowledge of the structural response of the different assumptions led to the design of a numerical model capable of reproducing some field-reported behaviours in the foundation. This model can be used to prevent deterioration in embedded-ring foundations, and future advances can guide maintenance and rehabilitation plans on existing wind turbine farms.

Keywords: wind turbine foundations; finite element models; embedded rings; nonlinear concrete behaviour.

RESUMO

A participação das turbinas eólicas no setor de energia continua a crescer, seu status de fonte de energia renovável as tornando atraentes devido às políticas ambientais estabelecidas em todo o mundo. A maioria dessas turbinas são instalações onshore e são suportadas por torres de aço conectadas a fundações de concreto armado por meio de anéis metálicos embutidos no concreto (“virolas”), um tipo de estrutura com danos relatados na interface torre-fundação. Este estudo apresenta procedimentos de simulação quanto ao comportamento estrutural desse tipo de fundação. Ênfase é dada ao desenvolvimento de modelos em elementos finitos com o auxílio do software de elementos finitos Abaqus. Foram desenvolvidos quatro modelos 3D com diferentes premissas numéricas para que fosse possível entender como cada uma afeta o comportamento estrutural e qual modelo melhor se adequa ao propósito de investigar o concreto ao redor da flange inferior do anel de aço. As premissas abrangem apoios elásticos não-lineares, contato e comportamento não-linear do concreto. Esta pesquisa fornece um recurso valioso, pois o conhecimento da resposta estrutural das diferentes premissas levou ao desenvolvimento de um modelo numérico capaz de reproduzir alguns comportamentos da fundação que foram relatados em campo. Esse modelo pode ser usado para prevenir a deterioração em fundações virola, e avanços futuros podem orientar os planos de manutenção e reabilitação em parques de turbinas eólicas existentes.

Palavras-chave: fundações de aerogeradores; modelos em elementos finitos; virola; comportamento não-linear do concreto.

LIST OF FIGURES

LIST OF TABLES

CONTENTS

1 INTRODUCTION

The object of this master's research project is inserted in the industry context, therefore acquiring multidisciplinary characteristics. The following topics will draw a frame of reference for the problem under investigation to help the reader navigate through the remaining text.

1.1 BACKGROUND

The world's current social and economic situations are moulded by a context of concern over climate change conditions. Since 1995, in Berlin, the annual Conference of the Parties (COP) has occurred with the ultimate goal of reducing the emission of harmful greenhouse gas to prevent human-provoked interference in the climate. Over the years, COP has set national goals and funds to help developing countries achieve this reduction. With the Paris Agreement, a landmark resulting from COP 21, in 2015, for the first time, legally binding nationally determined contributions (NDC) were established (UNFCCC, 2021?; UNFCCC, 2021a). As a result, the governments of 196 countries compromised to shift their economy towards more renewable and environmentally friendly processes instead of incentivising carbon-emitting activities, under the risk of suffering legal penalties if missing their NDC's.

Then in 2021, COP 26 brought an atmosphere of awareness regarding the world's harsh climate conditions and secured clarity and responsibilities about the necessary actions. This Conference established more robust and effective instruments for achieving environmental protection goals (UNFCCC, 2021a). For example, the Parties agreed to increase the support for developing countries through financial resources, technology transfer and capacity-building, with developed countries pledging to provide 100 billion dollars annually to the lesser developed ones (UNFCCC, 2021b). In addition, there was an accord to accelerate development, deployment and dissemination of technologies along with policies' adoption for the transition towards low-emission energy systems. The agreement states a focus on rapidly scaling up the deployment of clean power generation and energy efficiency measures while increasing efforts to phasedown continuous coal power and phase-out inefficient fossil fuel subsidies (UNFCCC, 2021b).

Now, energy demand is ever-increasing, and climate change efforts have increased the demand for renewable energy sources. According to IEA's Electricity Production

Report (IEA, 2019), global energy production has grown annually since 1974, apart from the reduced-demand period of the international financial crisis between 2008-2009. Complying to the rise in demand, the participation of renewable sources in this global energy generation growth was reported to amplify by British Petroleum (2021), accounting for 60% over the past five years. Even during the year 2020, the period of the Covid-19 pandemic, when overall power production fell, generation from renewables continued to grow. Indeed, it achieved its most significant increase, led mainly by wind and solar generations, which more than doubled.

Addressing wind energy specifically, it has only grown over the years, as Figure 1a shows, and its growth potential has not started to cease (GWEC, 2021). In 2020, there was a registered increment of 53% compared to 2019, totalling the installed capacity to 743 GW, and GWEC (2021) expects this steady-paced growth to continue towards a 1TW of global cumulative installations before 2025.

Some areas, of course, have more potential than others to generate wind energy and, therefore, to lead the predicted growth in wind power capacity. Brazil sits amongst the highest potential areas. In fact, it is already executing it on a large scale and shows up amid the top five markets responsible for the 93 GW growth in 2020, with a global share of 3% (Figure 1b, (GWEC, 2021)).

Figure 1 – Wind power data.

(a) Historical development of total installations of wind power.

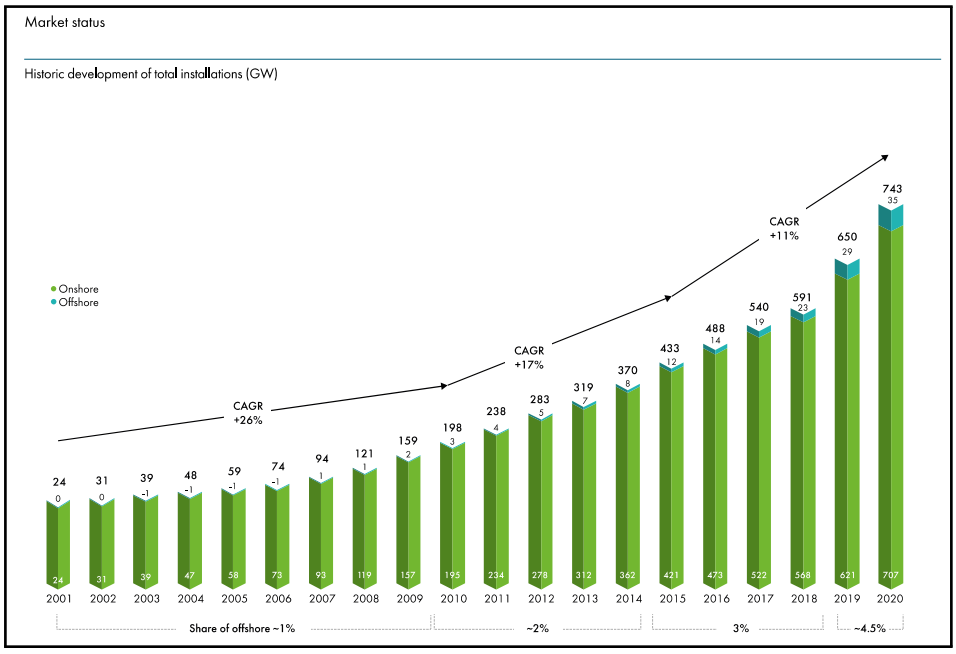

Source: GWEC (2021)

(b) New wind power capacity in 2020 and share of top five markets.

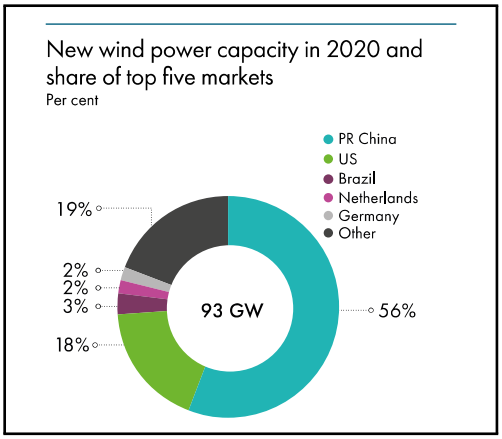

Source: GWEC (2021)

Further analysis into the Brazilian wind energy market shows how steeply it has developed over the last ten years and how much it must expand over the next five years. In November 2021, it is the second-largest source of energy production for Brazil (Figure 2), with an installed capacity of 20.1 GW distributed around 751 wind farms and 8820 operating wind turbines (ABEEólica, 2021). Ten years ago, this number was very different: less than 1 GW of capacity was installed in the country (GODOI, 2021). It is pertinent to highlight that GWEC (2021) points out the competitive prices in the energy market as one of the reasons for the escalation in capacity in 2020. Finally, the expected growth based on auctions and signed contracts is 60% until 2026, according to ABEEólica (2021).

Figure 2 – Brazilian electricity matrix.

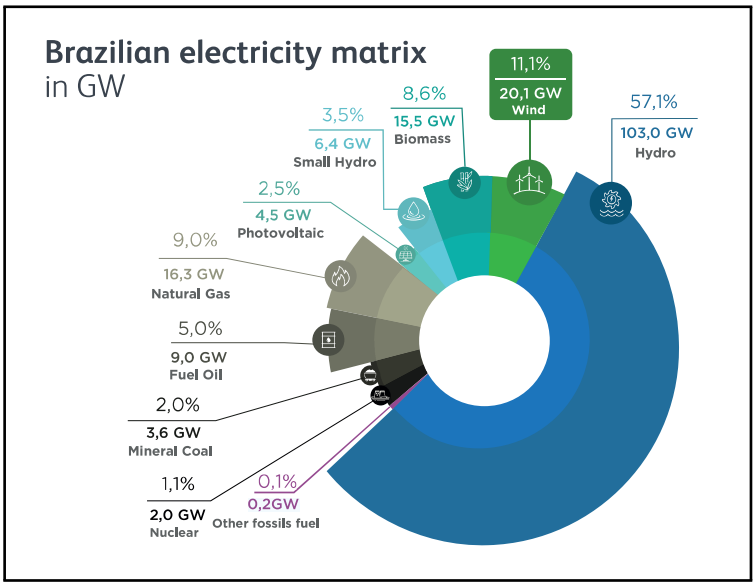

Source: ABEEólica (2021)

After this consolidation of wind energy's significance in both global and Brazilian societies, it is necessary also to get an overview of the electrical generator for this energy source. Chapter 2 describes the assembly that makes for a wind turbine in more detail. However, in broad general terms, mainly to situate the reader into the research at this initial stage, wind turbines consist of a set of components, different in size, shape and function, connected to produce electricity using the wind (see Figure 3). One module, which holds electrical and mechanical features responsible for converting movement into energy, is set on rotation by the passage of the wind through the blades. It stands high above a tower, which must support the weights and the loads resulting from the wind action over the system. This tower, in turn, must be supported by a structural foundation. This latter structure is responsible for absorbing all the loads from the ensemble mentioned above and transmitting them into the ground. It can be of distinct types, depending on the magnitude of the loads, the kind of tower, and the ground resistance where it will be set.

At last, the wind turbine foundation is the focus of this dissertation.

Figure 3 – Schematic representation of a wind turbine.

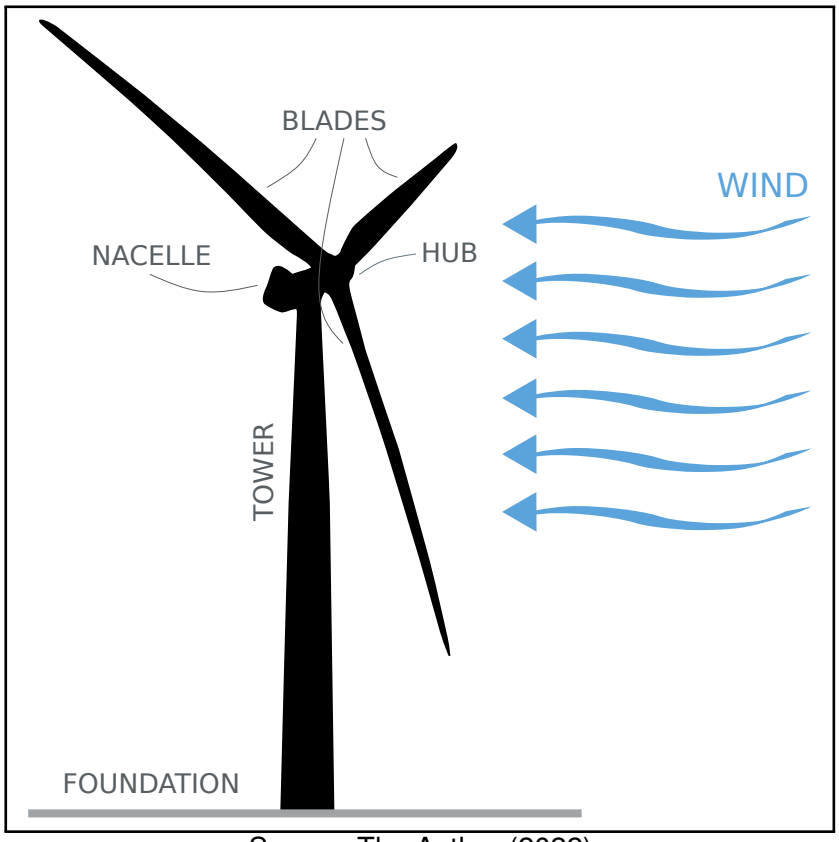

Source: The Author (2022)

1.2 OBJECTIVE

Of the available types of foundations for wind turbines, the embedded ring, conceptually and geometrically described in detail in Chapter 2, was the primary choice of the industry since the beginning (HASSANZADEH, 2012) and was present in most projects (HE et al., 2019). However, the increased stress in the foundations caused by higher-capacity wind turbines has led to the reporting of damages. Numerous researchers indicate that the concrete surrounding the bottom flange of the ring deteriorates, mainly due to relative movement between the ring and the concrete base. Their findings contain reports of excessive vertical movement of the steel structure, crushed concrete above and voids around the flange, and gaps between the structures. These recurrent damages present safety risks and high repair costs since they are temporary and associated with the interruption of electricity generation. This context induces further comprehension of those structures and their behaviour, which motivated the study presented here.

The conceptual plan in Figure 4 schematises the research's objective and means, which are based on 3D finite element models of an embedded-ring wind turbine foundation. The work aims to understand the structural behaviour of the region susceptible to damages, highlighted in the image, and the adequate degree of computational complexity and refinement. To achieve that, the author progressively built numerical models using the finite element software *Abaqus* to analyse the effect of different assumptions. Results are obtained with and without contact interaction between the ring and the concrete, fixed and elastic supports, and linear and nonlinear concrete, with reinforcement bars on the latter, and discussed.

Figure 4 – Objective and means.

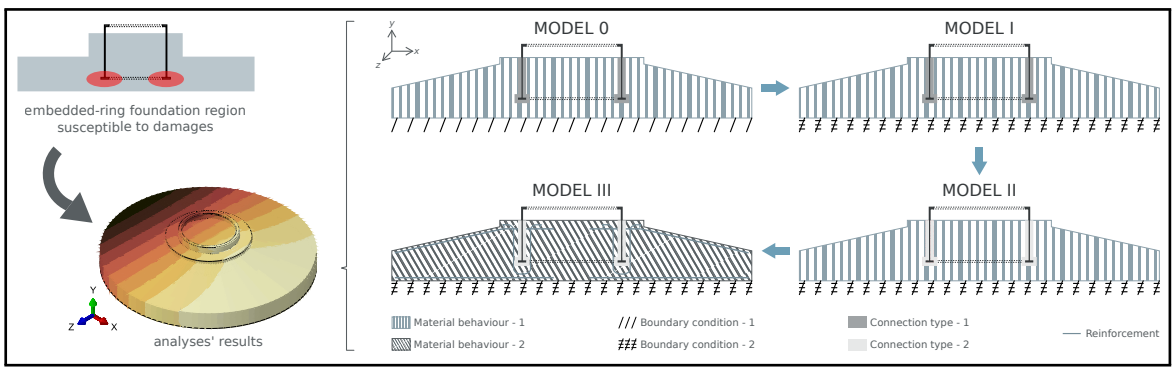

Source: The Author (2022)

1.3 SCOPE AND LIMITATIONS

The 3D finite element models, which are the scope of this project, were built after a reference project of a previously dimensioned embedded-ring foundation. As mentioned, the development of the research followed progressive levels of complexity and aimed at analysing four models: (1) a linear model, assuming perfect adherence between the concrete and the steel ring, rigidly supported by the soil; (2) another linear model with perfect adherence between the concrete and the ring, but with soil structure interaction; (3) a linear model with soil structure interaction that considered contact between the embedded ring and the concrete base; and (4) a nonlinear one, with steel reinforcement bars, contact and soil structure interaction. Simplified modelling and analyses were performed in parallel to validate material behaviour or calibrate computational features. The results of the analyses are discussed and then compared, fostering conclusions about the effect of the assumptions on the structural behaviour of the foundation model and about the ideal balance of precision and computational efficiency.

All this was not done without limitations. Primarily, it is crucial to highlight that this is an initial study with multiple challenges concerning the construction of the numerical models. The complex simulations demanded an expressive time of study, preparation and analysis, given the non-trivial nature of the work: an intricate physical problem of a particular structure subjected to a set of different types of loading that must be translated into a numerical model suitable for analysis. Therefore, the study's results are limited to the analyses of a specific embedded-ring, reinforced-concrete wind turbine foundation, which directly spreads its loads over the soil.

Additionally, the process of dimensioning the steel reinforcement, described in Section 3.2.2, suffered from a lack of consistent technical information, such as publications or guidelines on the subject, that could make for a design protocol. This reality is contextualised by Milititsky (2019) when mentioning how the expansion of wind power in Brazil brought challenges to the engineers responsible for designing the foundations since it involved characteristics and specifications different from what they had dealt with so far. The literature review found publications on the topic of wind turbine foundation design. However, they either do not cover the reinforcement design or do not go into detail about precisely what must be considered. Therefore, it is essential to highlight that the resulting reinforcement design presented in this dissertation is not

compromised to a structural design for construction purposes.

1.4 DISSERTATION OUTLINE

The following chapters will cover all the relevant aspects of developing this project. In Chapter 2, the reader will find the research context referring to wind turbines embedded-ring foundations and the reference project for the research. In Chapter 3, all the rationale (the relevant theoretical reasoning, studies and formulations) behind the numerical models. Chapter 4 dives into the numerical models themselves, explaining all the present features and parameters, presents the results and compares them amongst the models. Finally, Chapter 5 ends the work with some final remarks and recommendations for future research.

2 RESEARCH CONTEXT

This chapter will first give the reader the primary information regarding onshore wind turbines, such as the elements that constitute them and the available types. It will then explain the foundation type and problems associated with it, which are the object of this dissertation. Finally, the data that built the study case for the work will be presented.

2.1 WIND TURBINES

Different forms can be engineered to make a device convert the kinetic energy present in the air into mechanical work that will generate electricity. However, as stated by Hau (2013), practical usefulness will limit the number of significant designs. Within this framework, Hau (2013) classifies the onshore wind turbines mainly concerning their construction design. Firstly, they are divided into VAWTs (vertical axis wind turbines) and HAWTs (horizontal axis wind turbines) depending on the direction of their rotor's axis of rotation, as illustrated in Figure 5. Although representing the oldest design concept for wind turbines, the VAWTs are not competitive against the HAWTs. Its simple design allows installing mechanical and electrical equipment on the ground level. However, this advantage is rapidly overcome by the liabilities of low tip-speed ratio, inability to self-start and control power output and speed via pitching of the rotor blades, and high production cost in contrast to the HAWT system. In like manner, according to Whittlesey (2017), VAWTs have been responsible for only a tiny part of the market share of wind

Figure 5 – Wind turbine classification.

(a) VAWT - Vertical axis wind turbine. (b) HAWT - Horizontal axis wind turbine.

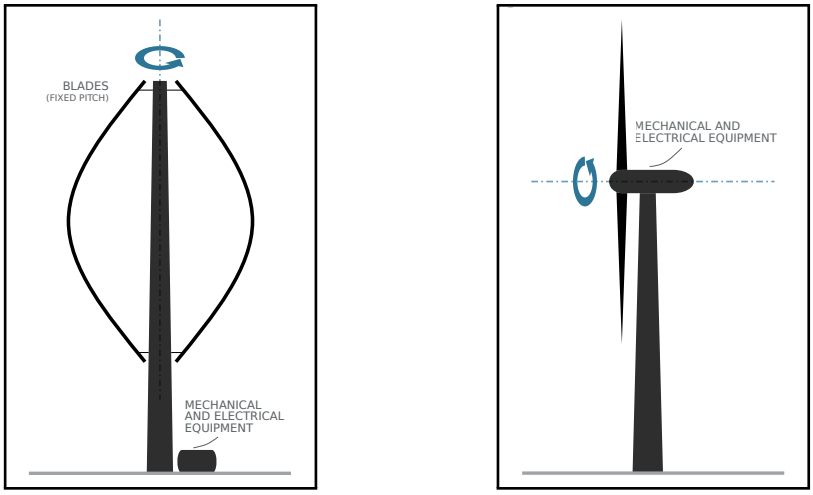

Source: The Author (2022)

energy over the years, mainly due to staying behind the HAWTs in terms of design efficiency.

Currently, the primary design concept and leader in associated technological developments is the principle of the horizontal axes. Unlike their vertical axes counterparts, they can control the rotor speed and power output through blade pitch control, protecting during extreme wind speed conditions. This research focuses on foundations used for this type of wind turbine, whose main components and specifications can be seen in the schematic image in Figure 6 and are defined below following the terms' descriptions adopted by Hau (2013):

Figure 6 – Wind turbine elements.

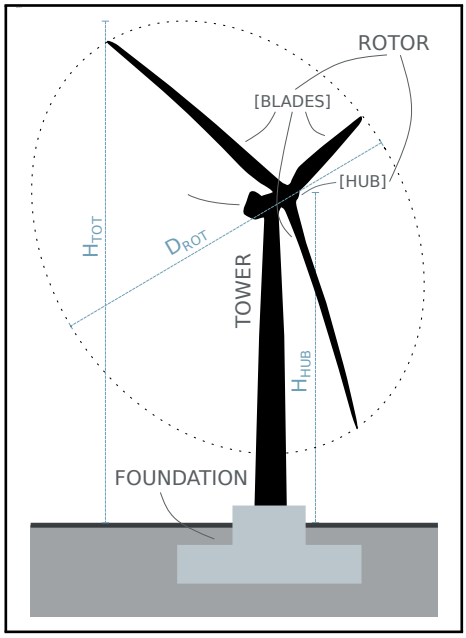

Source: Adapted from Hassanzadeh (2012)

- **Rotor:** this is the "actual wind energy converter", as the author calls it. It encompasses the blades and the shaft around which they turn, turning the wind energy into a mechanical rotation;
- **Hub:** makes the connection between the blades and the rotor shaft. It also holds the blade pitch mechanisms for wind turbines that possess this kind of control;
- **Nacelle:** harbours the drive train and electrical generator, responsible for converting the rotor's mechanical rotational motion into electrical energy;

- **Tower:** structure upon which the nacelle is mounted;
- **Foundation:** structure responsible for supporting the wind turbine and tower assembly and transmitting their loads to the ground;
- $\mathbf{D_{rot}}$**:** rotor's diameter;
- $\mathbf{H_{hub}}$**:** hub height;
- $\mathbf{H_{tot}}$**:** total height (hub height plus the rotor's radius);

The type options of onshore towers to support the nacelle are now many, mainly due to the necessity of reaching higher presented by the larger turbines being developed over time. Some common structural concepts consist of lattice towers, concrete towers, tubular steel towers and hybrid concrete-tubular steel towers (see Figure 7). Amongst those, the most commonly allotted one is the tubular steel tower, according to Hassanzadeh (2012). This system is manufactured as individual flanged tubular sections of 20 - 30m length (DNV GL, 2016), a disadvantage since transporting the units from the fabrication site to the wind energy plant is troublesome. Besides, it imposes project restrictions, such as a limit of 4 to 4.5m to the tower diameter. Also, higher hub heights will require greater diameters and thicker plates to withstand heavier loads, higher bending and torsional moments, and increase their natural frequency, making steel tubular towers expensive. However, this structure is the most suitable for a height

Figure 7 – Wind turbine tower structural concepts.

(a) Lattice tower.

Source: Wind turbine models (2014)

(b) Concrete tower.

Source: BFT International (2017)

(c) Hybrid (concrete + steel) tower.

Source: Ferhan Öztürk (2016)

(d) Tubular steel tower.

Source: Wind Insider (2021)

of up to 80m, according to Rebelo et al. (2014). It is light compared to the other alternatives, easily installed and presents low maintenance costs, justifying its use in most wind turbine projects.

The tower must then transmit all the loads acting over it and over the hub it supports onto the soil, and it does that via a structural foundation. What determines the type of the foundation are the wind turbine's size, the site's geological conditions, and the tower's configuration (HAU, 2013). Reinforced-concrete foundations are used to support tubular steel towers: generally, spread footings directly overloading the soil, if it has bearing capacity, or transferring their loads onto piles. This reinforced-concrete base attaches itself to the tower via two main strategies: (1) a tubular steel section, flanged at the bottom and inserted into the concrete (an 'embedded steel ring') or (2) a "cage" of prestressed anchor bolts (Figure 8). More on this in the next section.

Figure 8 – Types of tower-foundation connections.

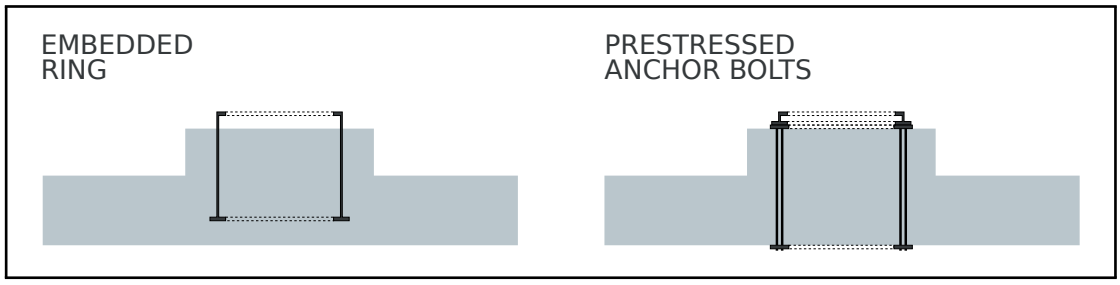

Source: The Author (2022)

2.2 EMBEDDED RING FOUNDATION

The next sections will present the embedded-ring foundation design and the literature discussion regarding the damages associated with it.

2.2.1 Design concept

The foundation this work assesses is a shallow one, based on the assumption that the structural loads will not cause the soil layers directly below it to settle excessively. If this was the case, a deep foundation could be used to reach a stiffer layer of soil and exploit the soil friction resistance (DAY, 2005), or soil enhancement techniques would need to be applied. Soil behaviour, however, is not within the scope of this research.

A standard slab foundation design for wind turbines is schematically represented in Figure 9. This foundation type stands directly beneath the structure it supports and characterises itself by transmitting the loads to the ground through the distributed stresses under its base surface (ALONSO, 2019). If the structural loads are too high, this attribute might lead to enormous and uneconomical dimensions in an effort to reach stresses compatible with the soil bearing capacity. One strategy to reduce the size of the foundation is to place it below ground level such that backfill soil may be deposited over its top surface. The weight of the soil will then counteract the overturning tendency of the foundation, allowing for smaller dimensions.

Figure 9 – Wind turbine slab foundation.

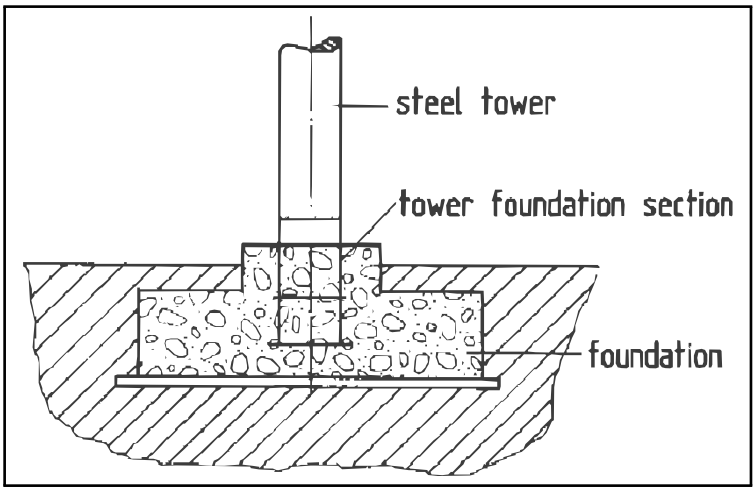

Source: Hau (2013)

Following the discussion above, Figure 10 further details the reinforced concrete structure in question according to the definition in (SHABAN, 2017) of it being a tapered

footing rigidly attached to a central pedestal. The geometry of the footing is usually circular, rectangular or octagonal and influences the layout of the bending steel reinforcement: squared bases are provided with a cartesian placement of the bars, while the circular and octagonal ones tend to receive radial placements (HASSANZADEH, 2012). The pedestal is where the tower meets the foundation and, as Shaban (2017) points out, helps protect the tower from chemical attacks and corrosion caused by contact with the soil.

Figure 10 – Tapered reinforced concrete foundation.

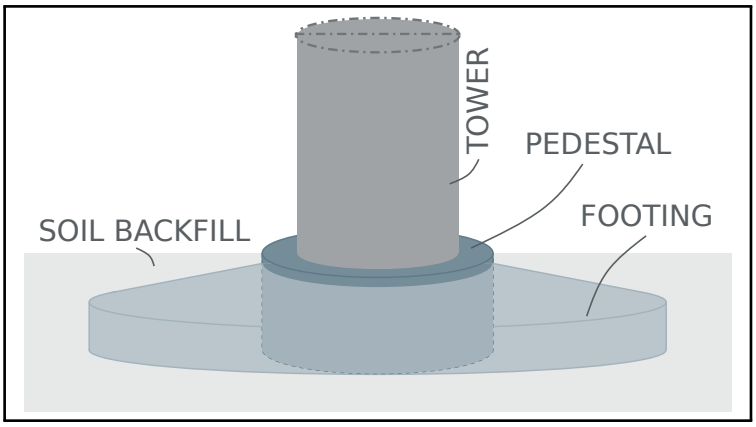

Source: The Author (2022)

Embedded into the reinforced concrete geometry is a feature of crucial importance: the element that anchors the tower to the foundation. This connection works as a load-transfer mechanism from the steel tubular tower to the concrete, and, as previously mentioned, there are two widely used design options for it: an embedded ring and an anchor cage (as per Figure 8).

The anchor cage uses prestressed anchor bolts fixed to load spreading plates on both ends (Figure 11a) to attach the tower section to the foundation. The lower plate alone is responsible for anchoring the system to the inside of the concrete due to the prevention of contact between prestressed bolts and concrete through a covering of the steel surfaces (HASSANZADEH, 2012). The top plate is fixed to the top of the pedestal and fastened to the flange of the bottom tower section with bolts (Figure 11b). Prestressing the bolts aims to improve the fatigue behaviour of the anchorage system by securing the connection even under the intense tensile effects of wind loading (MORAAL, 2019): it is the structural mechanism used to prevent concrete cracking in the anchor cage design.

Figure 11 – Anchor bolt foundation.

(a) Anchor bolts cage.

Source: Anyang Longteng Heat Treatment Material Co. (-)

(b) Detail of top plate with bolts.

Source: CTE Wind International (-)

On the other hand, the embedded-ring foundation system is based on a metallic tubular structure cast inside the reinforced concrete, over whose L-shaped top flange the tower's bottom section can be bolted (Figure 12a). This so-called ring is similar to one of the tubular sections of the steel tower, thereby often referred to as the "foundation section". A lower flange transfers the tensile and compressive forces to the reinforced concrete. In the wall of the ring, between the flanges, holes allow the crossing of longitudinal reinforcement bars (Figure 12b)) which, according to Hassanzadeh (2012), must be isolated from the steel ring with a sealant. Finally, the crack prevention mechanism in this design relies on the use of the reinforcement bars to assist in anchoring the ring to the concrete (Figure 12c).

The embedded-ring design was widespread at the beginning of wind energy development and continues to be the choice for several projects. Currie et al. (2015) mentions that some 4000 wind turbines with the embedded-ring foundation were ope-

Figure 12 – Embedded-ring foundation.

(a) Foundation under construction.

Source: Francesco Miceli (2012)

(b) Detail of longitudinal bars crossing the ring wall.

Source: Hassanzadeh (2012)

(c) Detail of reinforcement bars design.

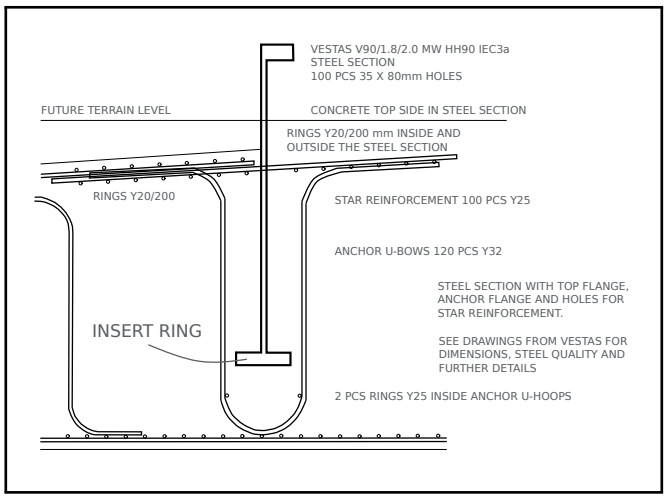

Source: Adapted from Hassanzadeh (2012)

rational in 2015, making it highly prevalent. However, today's wind turbines have a higher capacity than at the beginning, which requires them to be larger, creating a more significant structural burden on the foundation. It culminated in increased stresses that led to damages in embedded-ring foundations (HE et al., 2018). Given the popularity of the foundation system, the need for better understanding the deterioration-related problems and figuring out a way to solve them is only reinforced.

2.2.2 Associated damage

Although the exact number of embedded-ring foundation failures in wind turbine farms is unavailable for commercial reasons, the previously mentioned popularity of this foundation system points to an extensive problem, according to Currie et al. (2015). This notion is well-supported by site investigations in Canada, China, Denmark, Germany, the United Kingdom and others. For example, there are reports of (1) cracks found in almost all the 22 foundations of Nova Scotia Power's wind farm in Nuttby Mountain (HE et al., 2018; HE et al., 2019); (2) excessive vertical movement and small horizontal displacement in 37 foundations in China, after only three years of operation(HE et al., 2018; HE et al., 2019); (3) upwards movement of 20mm or more under extreme wind loads in the United Kingdom (CURRIE et al., 2015; CURRIE et al., 2013); and (4) 3mm gaps between the steel ring and the concrete, which relaxed the coupling between the elements and allowed for visible relative movement (HASSANZADEH, 2012).

The type of degradation that occurs in the boundary between tower and foun-

dation is the most common to afflict gravity foundations, according to He et al. (2019). These structures are subjected to load combinations, including shear and axial forces plus bending and torsional moments, which use the load-transfer mechanism of the ring to reach the concrete. However, Chen et al. (2021) argues that there is no sufficient stiffness constraining the ring inside the concrete to maintain its anchoring for higher capacity wind turbines. Without the proper anchor, the steel element can move within the concrete.

This resulting relative movement is intricately related to the design concept of the embedded-ring foundation. A description of why the damages appear, by Hassanzadeh (2012), starts with the loads' action on the steel ring, which then strains differentially from the concrete resulting in the gaps between both elements. Additionally, the horizontal movement of the ring stresses the concrete beyond what can be resisted by the reinforcement, leading to cracks in the concrete. Chen et al. (2021) considers this an illustration of the fact that relying on reinforcement bars alone to connect the steel ring to the concrete via bonding results in a weak anchorage system. Cyclic loading is also responsible for deterioration issues since it causes fatigue cumulative damage that increases the concrete's residual deformation and reduces the attachment's effectiveness, according to He et al. (2019). Despite that, fatigue is beyond the scope of this research, so the subject will not be developed further.

These design-related damages reduce the structure's ultimate capacity and stiffness He et al. (2018) and pave the way to further issues, such as the appearance of voids around the embedded-ring flange (CURRIE et al., 2013), the surfacing of cement slurries on the foundation and the detriment of waterproof layers (CHEN et al., 2021). In addition, they can worsen problems by allowing water to pervade the foundation's interior and then leach the concrete from the transition zones, increasing the gaps. Moreover, the shifting of the ring provoked by the cyclic loads can even create a pumping effect that carries the water inside (HASSANZADEH, 2012).

Although a complete collapse of a wind turbine due to its damaged foundation is not a customary event, the same cannot be said of the localised failures just discussed (HE et al., 2019). This scenario creates an insecure and unpredicted costly context for the wind energy industry. It is clear how deterioration of the concrete that allows for accidental movement of the embedded ring and, consequently, of the tower brings consequences to the system and, therefore, requires repair. If the repairing action

involves below-ground activity, the wind energy generation has to be interrupted (PERRY et al., 2017), incurring further financial losses. Currently, the existing cracks and gaps are usually closed with grout or epoxy resins. Although this may prove an immediate strengthening measure, it is not a permanent solution. As Chen, Xu e Li (2020) stated, since the cause of the problem, which is linked to the load-transfer mechanism, was not solved, the cracks and gaps will arise again. Furthermore, there is no data-based knowledge to specify how long the effectiveness of this solution endures (HE et al., 2018).

To counteract this recurrent use of temporary solutions, some researchers have published on the behaviour of the embedded-ring foundation damages, some even advancing on the subject and proposing permanent strategies to repair and strengthen the foundation. Next follows a discussion on their findings and contributions.

Currie et al. (2013) presented a study of a displacement data gathering system retrofitted to an existing wind turbine embedded-ring foundation. The project's goals were to establish a structural health monitoring (SHM) system to provide better knowledge regarding the steel ring's vertical displacements so that the foundation's potential failures could be avoided. The intent was to compare the displacement data acquired with SCADA's wind speed and direction. Since destructive interventions were not allowed, displacement sensors were installed at the bottom of the towers (see Figures 13a and 13b) to measure the vertical motion of the steel ring. The 2MW wind turbines being tested had been under operation for a minimum of 5 years. In subsequent publishing, (CURRIE et al., 2015), the authors present the results from the acquired data analysed against the SCADA information. They found a significant movement of the ring, especially during turbulent wind and turbine start-up and shutdown times. Besides, the displacement

Figure 13 – Contributions from Currie et al. (2013) and Currie et al. (2015).

(a) Sensors installation.

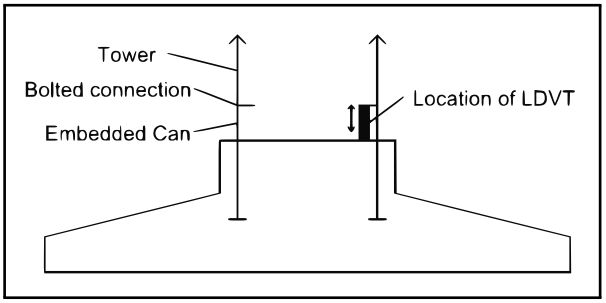

Source: Currie et al. (2013)

(b) Sensor layout schematic.

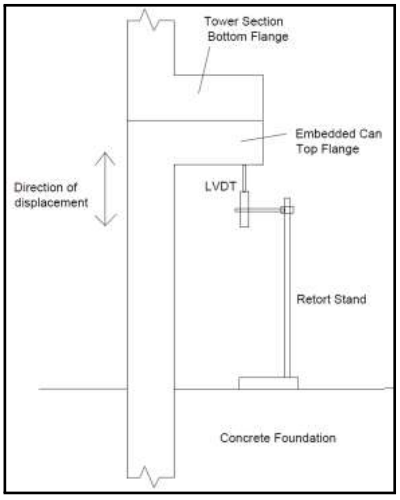

Source: Currie et al. (2013)

(c) Damages.

Source: Currie et al. (2015)

pattern varied along the ring's circumference due to changes in wind direction. As a result, this research showed a critical correlation between the wind direction and speed and the vertical displacements of the embedded ring. It also established their connection to the damages encountered in the foundation. Figure 13c identifies damages connected to the excessive movement of the ring on a site investigation (CURRIE et al., 2015).

Bai et al. (2017b) also presented field data acquisition and analysis research involving SHM. The work focused on using real-time condition monitoring to record strain, crack-opening displacement and temperature data along with ultrasonic testing to locate voids, cracks and further anomalies in the foundation. The researchers aimed to develop a better method to evaluate the structural condition of the foundation since the traditional one consists of the extraction of core samples, which affects the structural integrity. In this work, strain sensors were placed around the bottom flange of the embedded ring (Figure 14) during the construction of the foundation for a 1.5 MW turbine. During operation, any deformation in the concrete in this region caused a change in the wire length inside the sensors, which in turn was converted into an electrical signal. The main findings showed (1) a correlation of crack width variation with shifts in wind speed and direction; (2) an incident of tensile stresses on the concrete around the bottom flange, inside and outside it, produced by the steel-ring deformation; and (3) a higher value of strains on the lower region of the anchorage zone if compared to the higher zone (see the plotted results in Figure 15).

Figure 14 – Sensor arrangement from Bai et al. (2017b).

(a) Sensors in cross-section.

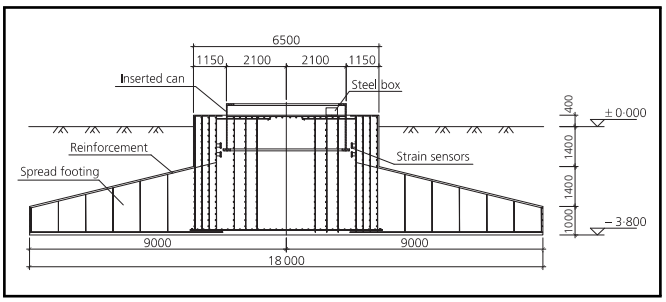

(b) Arrangement of measuring points and sensors.

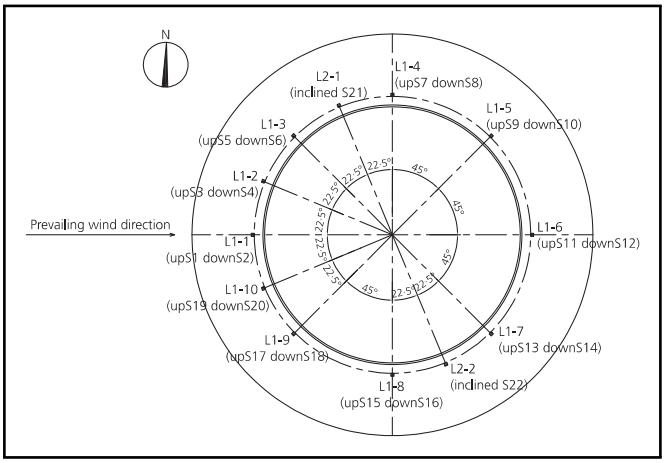

(c) Details of vertical pairs of sensors.

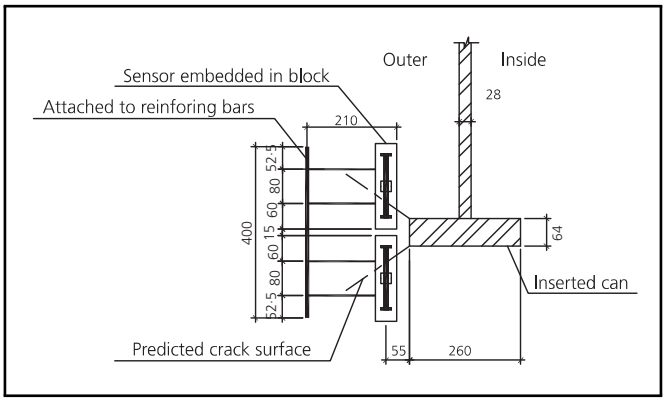

Source: Bai et al. (2017b)

Figure 15 – Results from Bai et al. (2017b).

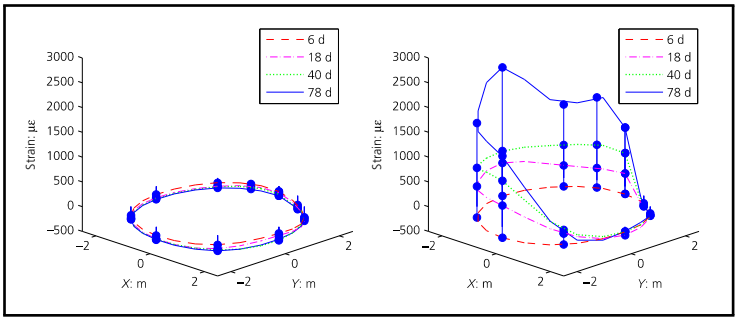

Source: Bai et al. (2017b)

In (PERRY et al., 2017), the work is again built around data acquisition systems. Subterranean fibre-optic sensors were designed, fabricated and installed to monitor foundation cracks' opening and lateral displacements during operation. The research was conducted on a gravity foundation with prestressed bolts instead of the embedded-ring design concept; therefore, the results do not apply. However, it presents an inspired approach to determining the wind loads acting on top of a wind turbine gravity foundation. Through a simple mathematical strategy, based on (KAWAI; MICHISHITA; DEGUCHI, 2008), the author considers the wind turbine as a fixed-free cantilever subjected to wind loads acting over the tower (wind profile - V(z)) and over the turbine blades (thrust - T) to derive the resulting horizontal force and overturning moment on the top of the foundation (Figure 16). This procedure was reproduced in (DOURADO; AGUIAR; RIBEIRO, 2020) to estimate the equivalent static and the dynamic wind loads, with the strategies for both situations derived and explained in detail.

Figure 16 – Wind loads contributing to overturning moment on the foundation.

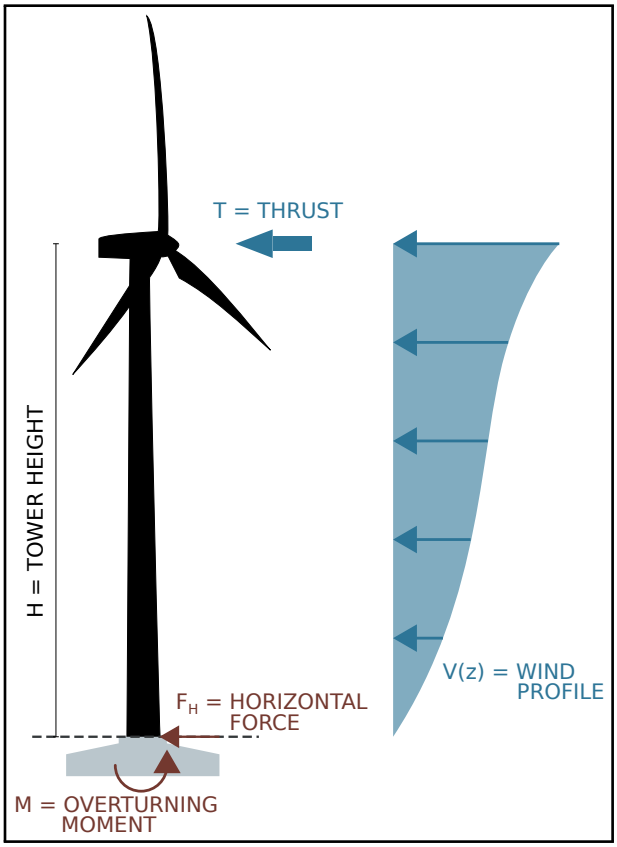

Source: Adapted from Perry et al. (2017)

Zhou, Kong e Dow (2015) presented a case study of an embedded-ring wind turbine foundation with analytical and finite element analyses to identify the causes of failure and to understand the mechanical behaviour. The researchers aimed to inform

and foster improvements to the design concept to prevent future damages. The study worked with a wind farm of 1.5MW wind turbines in China that started operation in 2010 and shut down in 2013 due to excessive damage. Site inspection found large amounts of concrete powder crushed and piled up on the pedestal of the foundation, close to the ring, resultant of the grinding movement caused by slipping of the surfaces (Figure 17a). After the foundation was cut for a deeper inspection, the concrete above the ring's flange was found to be crushed (Figure 17b), and the reinforcing bars crossing the embedded ring through its holes had sheared due to the large separation between ring and concrete (Figure 17c).

Figure 17 – Embedded-ring foundation damages presented by Zhou, Kong e Dow (2015).

(a) Concrete powder. (b) Crushed concrete. (c) Sheared reinforcement.

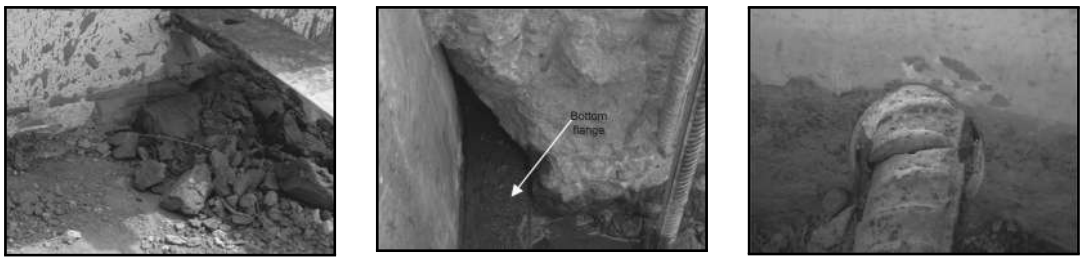

Source: Zhou, Kong e Dow (2015)

The research work analysed the bond behaviour between the steel ring and concrete surfaces to grasp how the load-transfer mechanism behaves concerning the presence or absence of slip. It found that under extreme wind loading, the bond shear between the elements is lost, causing all loads from the tower to be transferred to the bottom flange of the ring before spreading to the concrete. This situation will create normal upward or downward compressive stresses on the flange, depending on the wind direction, which will compress the concrete above or beneath the flange accordingly. The structural behaviour was analysed through a 3D finite element model built using Abaqus software that considered the nonlinear material behaviour of concrete with a damaged plasticity model and the interaction between the steel ring and the reinforced concrete through contact elements. It confirmed the fracturing and crushing of concrete over the flange plus a visible slip between the structures. To prevent these problems, the authors recommended improving the bond between the steel ring and the concrete by increasing the surface roughness and area of the ring. To achieve this, they suggested (1) welding shear studs to the embedded wall of the ring; (2) using fibre reinforced concrete; (3) increasing the punch and shear capacities of the concrete above the

embedded flange of the ring by enlarging the area of the flange and the load-carrying capacity of the concrete; and (4) welding annular steel strips immediately above the flange to block the development of the 45° diagonal shear cracks.

He et al. (2019) performed both experimental field tests and numerical modelling focused on evaluating an SHM system of strain sensors installed around the flange of the embedded ring (Figure 18). The foundation under study held a 1.5 MW wind turbine and was monitored during eight months of operation. The numerical model built using Abaqus consisted of a 3D finite element model including concrete nonlinearity, steel reinforcing bars, and contact elements between the steel ring and the reinforced concrete and was analysed under constant axial compression and cyclic overturning moment, shear and torsion to model the behaviour of the foundation and compare it with the deformation data collected with the strain sensors. The conclusions again confirmed the wind speed and direction as a central load aspect and primary responsible for localised deformation in the concrete. The pressure distribution around the bottom flange of the embedded ring showed an almost triangular pattern in operating conditions, with peaks in the centre and minimal values to the edges of the flange (Figure 19). Cracks were found both inside and outside the ring, around the bottom flange, but those on the inside closed after curing, while the ones on the outside appear to stay open and continue to increase.

Figure 18 – Strain sensors installed around the flange of the embedded ring.

Source: He et al. (2019)

Bai et al. (2017a) performed a numerical study on the fatigue behaviour of an embedded-ring foundation to investigate the local deterioration of the concrete under the effect of cyclic loads and its consequences over the entire structure. The authors developed a theoretical constitutive model for onshore wind turbine foundations under fatigue loading and built a 3D finite element model to calibrate it. The numerical model was created in Abaqus with a nonlinear material behaviour for the concrete, reinforcing

Figure 19 – Results from He et al. (2019).

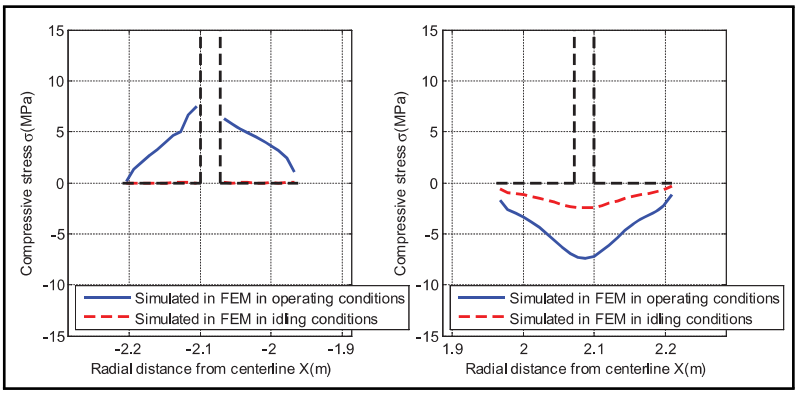

Source: He et al. (2019)

steel bars, failure surface underneath the bottom flange to input an initial fracture to the model and the exact load characterisation in (HE et al., 2019). The finite element analysis was executed for the maximum static equivalent loads to calibrate the fatigue analysis algorithm, and the findings from this initial stress state presented a pressure distribution for the region surrounding the bottom flange of the steel ring similar to the results encountered by He et al. (2019) (see Figure 20).

Figure 20 – Results from Bai et al. (2017a).

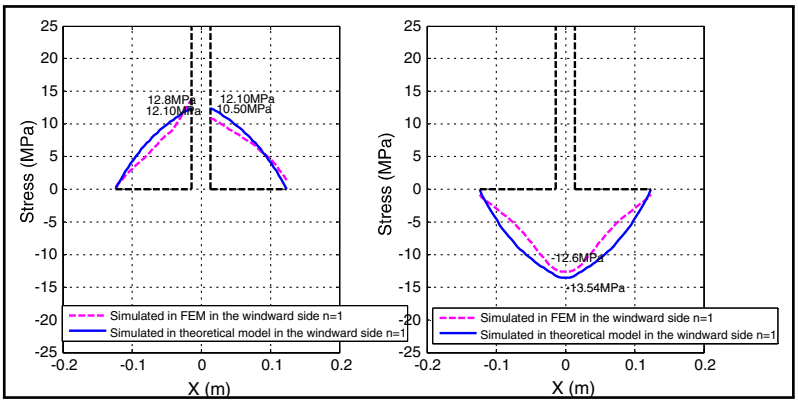

Source: Bai et al. (2017a)

He et al. (2018) developed a retrofit proposal to improve the strength of embedded-ring foundations and applied it to an existing, cracked structure. The concept of the proposal was based on external prestressing. First, high-strength grout was pumped into the void in the anchorage zone, followed by epoxy being pressurised in the gap between the ring and the concrete (see Figure 21a). These steps are meant to increase the local bearing capacity of the concrete and the bond behaviour, respectively. Then, six steel girders were installed on top of the pedestal, circling the steel ring per the scheme in Figure 21b, with prestressed anchor bolts in each extremity that were post-

bonded to the foundation (Figure 21c). The girders were covered in concrete and steel reinforcement. Through field measurements using strain sensors and strain gauges, the researchers were able to analyse the efficiency of the strategy by comparing data from the intervened foundation to an original one used as a control tool. The results showed that the external prestressing limits the crack width close to the flange and improves the stiffness of the foundation.

Figure 21 – Retrofit proposal for an embedded-ring foundation (HE et al., 2018).

(a) Details - cross-section. (b) Details - plan view.

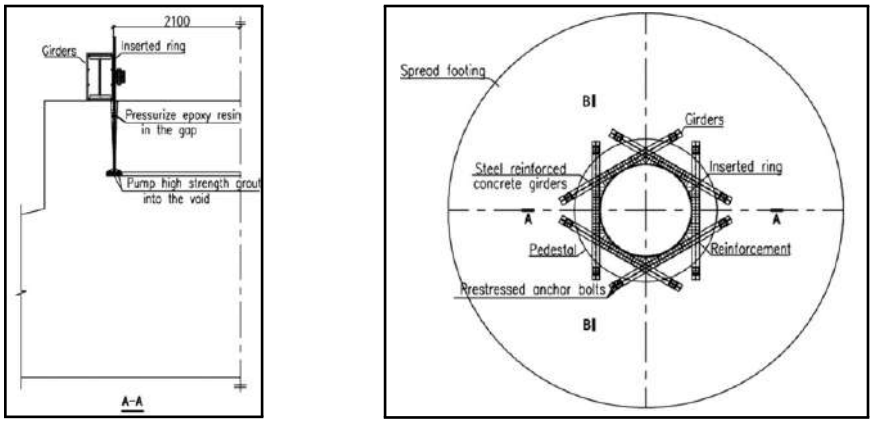

(c) Details - prestressed anchor bolts.

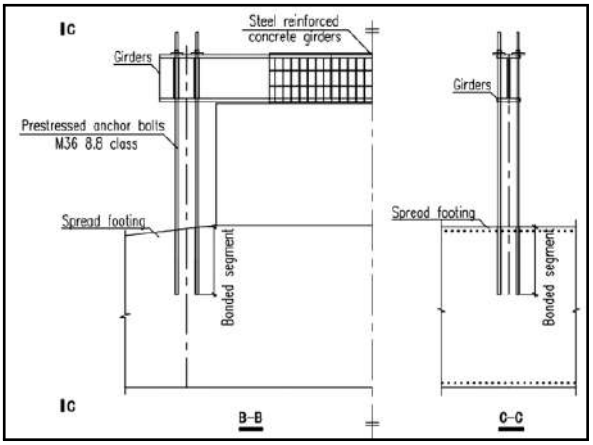

Source: He et al. (2018)

Like He et al. (2018), Chen, Xu e Li (2020) proposed a strengthening design intervention to existing embedded-ring foundations, but in this case the evaluation was performed through numerical analysis. By comparing the steel ring with the concept of embedded column footings, where the resistance to overturning moments depends mainly on the lateral contact of the concrete foundation with the steel column wall, the authors stated that the embedding depth of the steel ring in the concrete was too shallow. The research defines this as the root cause of stress concentration on the

concrete above the flange, which deteriorates the material and reduces the constraint stiffness of the pedestal. In turn, the latter leads to larger horizontal displacements of the tower and reduces the system's natural frequency. Additionally, the researchers highlight the absence of shear studs welded to the steel ring's wall, as occurs with the embedded column footings, to increase the binding force (the reader will remember that this was also present amongst the suggestions of Zhou, Kong e Dow (2015) for design improvement). Therefore, the overturning moment acting over the foundation can only be resisted by the flange's anchoring and the concrete's lateral resistance pressure against the steel wall.

To solve the abovementioned issues, the researchers proposed to (1) fill the existing gaps and cracks with high-strength epoxy resin; (2) increase the height of the pedestal until the bottom flange of the tower with a reinforced concrete cover; and (3) add circumferential prestressing using steel strands placed around the pedestal (Figure 22). They performed 3D finite element analyses in Abaqus involving concrete nonlinearity, reinforcement steel bars and contact interaction to present the structural behaviours of the foundation pre- and post-strengthening. The results showed improvement: the tensile stresses were reduced below the characteristic value, the strength on the steel bars decreased by 37.5% and the plastic region of the foundation was significantly diluted.

Figure 22 – Retrofit proposal for an embedded-ring foundation (CHEN; XU; LI, 2020).

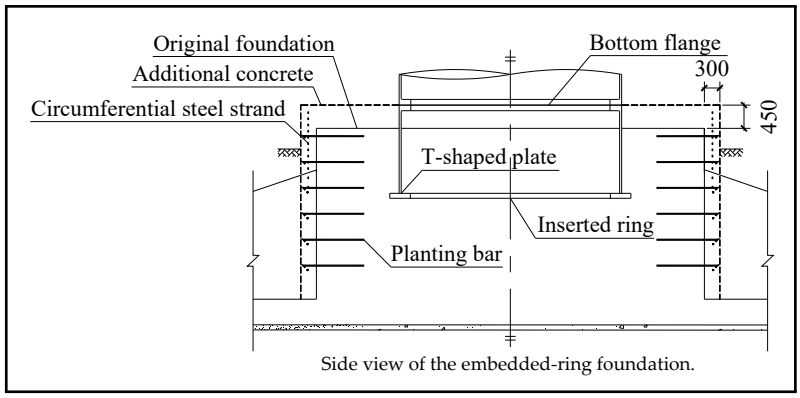

Source: Chen, Xu e Li (2020)

Subsequently, in (CHEN et al., 2021), the researchers added a feature to enhance the strengthening mechanism of the retrofit proposed in (CHEN; XU; LI, 2020): the previously mentioned welding of studs on the wall of the ring above the original pedestal (Figure 23). The aim was to increase the connection of the steel ring to the reinforced concrete foundation. To this end, the research presents a method to determine the

necessary number of studs and to estimate their contribution to resisting the overturning moment. Once more, finite element analyses were performed, and the results showed structural behaviour improvement after the intervention, with tensile plastic areas remarkably reduced. This time, the critical effects pertained to crack width and displacement reductions: the maximum crack width surrounding the flange decreased from 0.18mm to 0.08mm, while the maximum gap between the steel ring wall and the top of the original pedestal went down to 0.04mm, in the repaired foundation, from 0.4mm in the original one.

Figure 23 – Retrofit proposal for an embedded-ring foundation (CHEN et al., 2021).

(a) Overview. (b) Arrangement of studs.

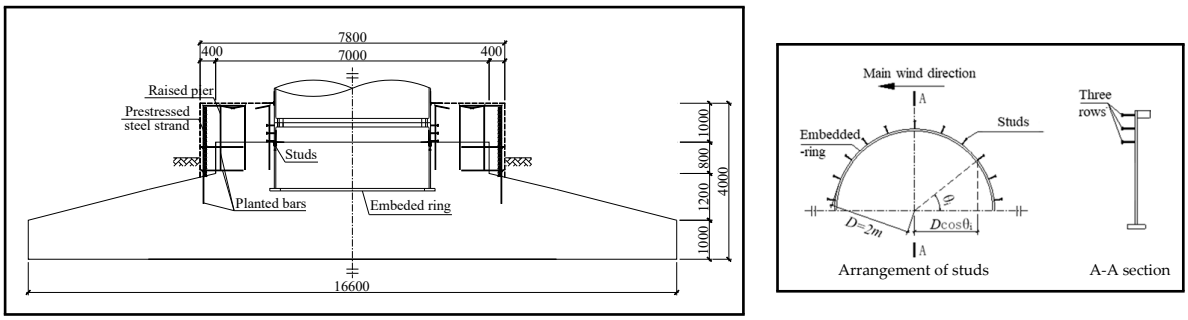

Source: Chen et al. (2021)

2.3 CASE STUDY DATA

This chapter will present all the information pertinent to the models. The goal is to build a summary of the project data for the reader that is structured, organised and easily accessible in a single section of the text. Some figures and tables from the text were replicated here (their titles reference the original placement). Part of the data stems from (SVENSSON, 2010), the reference project regarding the foundation geometry, material properties and supplier's loads. The pieces of information unavailable in (SVENSSON, 2010) were determined or assumed based on theoretical reasonings detailed in Chapter 3.

Figure 24 shows the geometry of the foundation slab (informed by Svensson (2010)). It is assumed to support the same wind turbine as it does in the referenced project: a Vestas V-90 of 2MW. Relevant turbine information extracted from the product's brochure (Vestas, 2009) appear in Table 1 for contextualization.

Figure 24 – Foundation geometry.

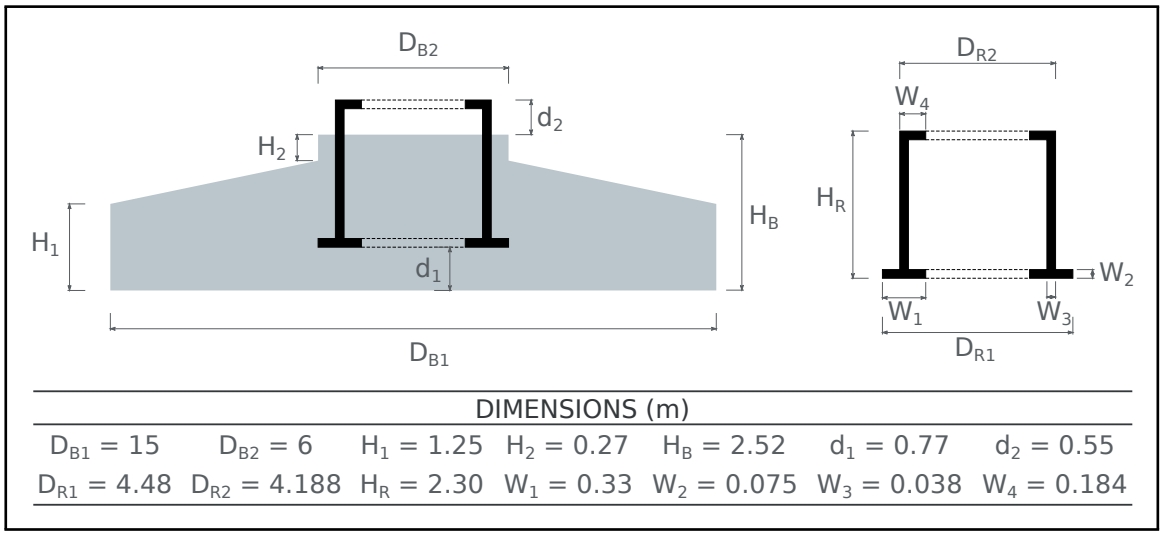

Source: The Author (2022)

Table 1 – V90 - 2MW wind turbine specifications.

Operating data		**Rotor**		**Tower**	
Rated power	2000 kW	Rotor diameter	90 m	Type	Steel
Cut-in wind speed	4 m/s	Swept area	6362 m²	Height	80 m
Rated wind speed	12 m/s	Blade length	44 m	Weight	148000 kg
Cut-out wind speed	25 m/s	Blade weight	6700 kg	**Nacelle**	
		Hub weight	18000 kg	Weight	18000 kg

Source: Vestas (2009)

The concrete and steel material properties are presented in Tables 2 and 3, respectively. The strength grades for both concrete and reinforcement bars were considered the same as in (SVENSSON, 2010). The type of steel for the steel ring, which has linear behaviour assumed throughout the research, was chosen based on the frequent material properties encountered in the literature. The parameters common to both tables are the Young's modulus (E), the Poisson's ratio (ν) and the density (ρ). Besides those, there is the mean cylinder compressive strength of concrete (f_{cm}), its uniaxial tensile strength (f_t) and fracture energy (G_F), and the yield stress of steel (f_y) for the reinforcement bars. Section 3.3 dives into determining the listed values that led to the materials' behaviours described in Figures 25 and 26.

Table 2 – Physical and mechanical properties of the concrete. *[ORIGINAL: TABLE 11]*

	E (MPa)	ν (-)	f_{cm} (MPa)	f_t (MPa)	G_F (kN/m)	ρ (kg/m³)
C30/C37	32837	0.2	38	2.03	0.06619	2400

Source: The Author (2022)

Table 3 – Physical and mechanical properties of the steel. *[ORIGINAL: TABLE 12]*

	Structural Elements	E (MPa)	ν (-)	f_y (MPa)	ρ (kg/m³)
Q345B	Steel ring	206000	0.3	(-)	7850
B500B	Reinforcement bars	200000	0.3	435	7800

Source: The Author (2022)

Figure 25 – Stress-strain and damage parameter-strain curves of concrete.

(a) Compressive behaviour. *[ORIGINAL: FIGURE 54]* (b) Tensile behaviour. *[ORIGINAL: FIGURE 53]*

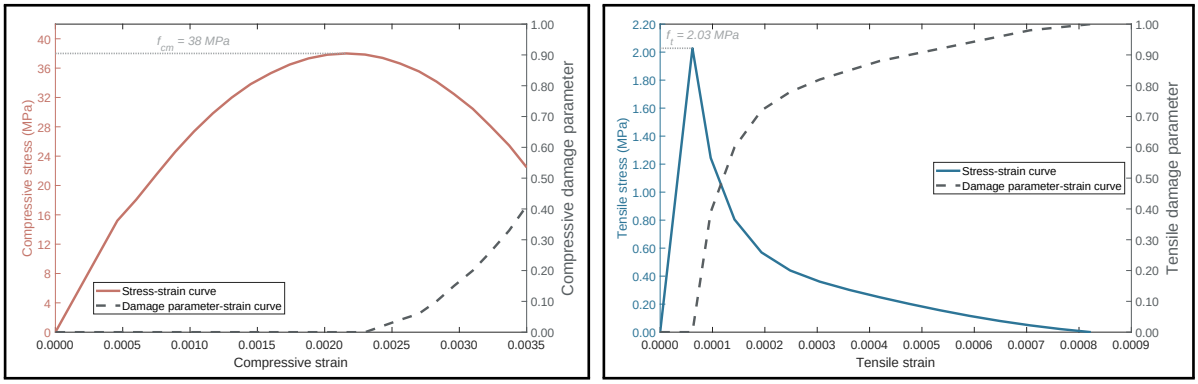

Source: The Author (2022)

Figure 26 – Stress-strain curve for the reinforcement bars steel. *[ORIGINAL: FIGURE 55]*

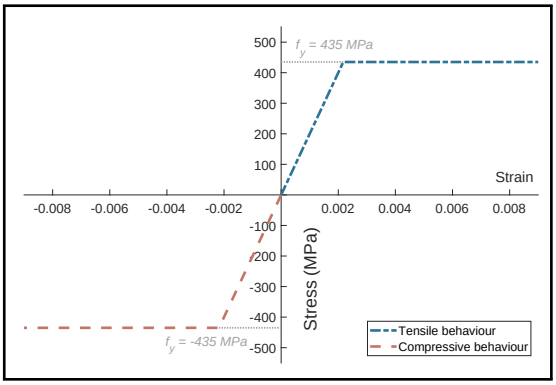

Source: The Author (2022)

Table 4 holds the soil properties relevant for the simulations: the specific weight (γ) and the vertical (k_V) and horizontal (k_H) moduli of subgrade reaction. The values

adopted derive from (RODRIGUES, 2019) and Section 3.1 explains the soil-structure interaction considered in the model and how these moduli were applied.

Table 4 – Physical and mechanical properties of the soil.

	γ (kN/m³)	k_V (kN/m³)	k_H (kN/m³)
Practically rigid soil	18	160000	32000

Source: Rodrigues (2019)

Figure 27 displays a schematic of loads on the foundation. The wind turbine loads (Table 5) were considered to be the same as in (SVENSSON, 2010), already in their ultimate limit state values and acting on top of the foundation ring. Besides those, there are also the foundation self-weight and the weight from the soil backfill (Table 6).

Figure 27 – Loads.

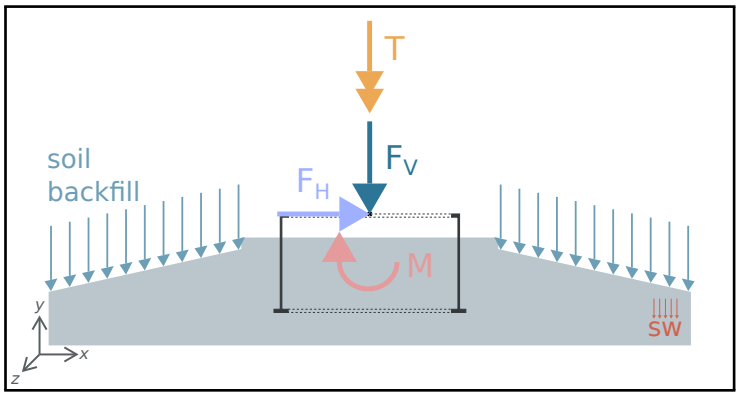

Source: The Author (2022)

Table 5 – Wind turbine loads. *[ORIGINAL: TABLE 7]*

F_V (kN)	F_H (kN)	M (kN.m)	T (kN.m)
3510	797	63825	1642

Source: Svensson (2010)

Table 6 – Weight loads. *[ORIGINAL: TABLE 8]*

Self-weight - sw (kN)	Soil backfill weight (kN/m²)
7636.8	14.4

Source: The Author (2022)

The steel reinforcement design and detailing procedures are described in Section 3.2.2. Figure 28 describes the steel bars present in a numerical model, their diameters and how they are arranged inside the foundation.

Figure 28 – Arrangement of the steel reinforcement bars.

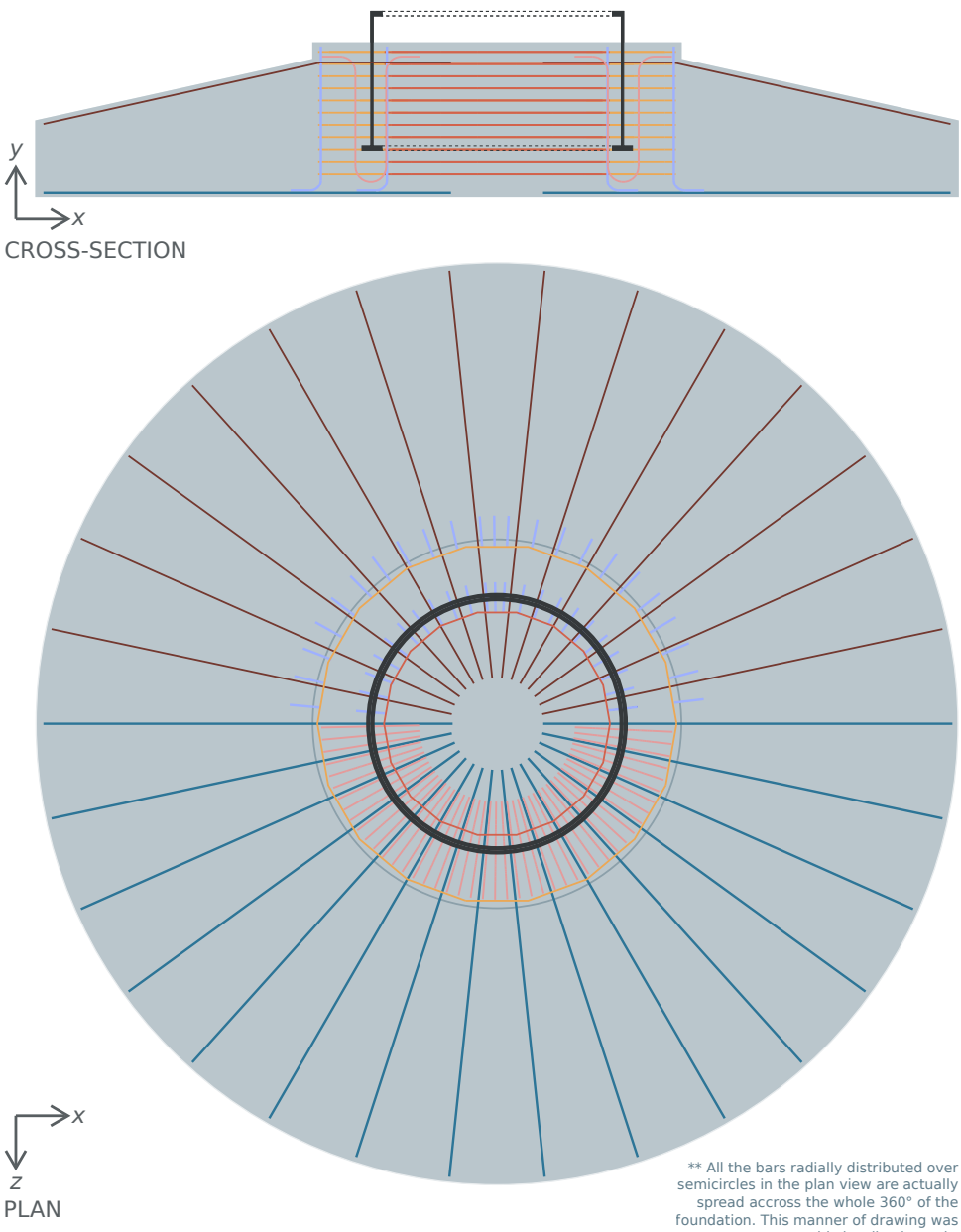

REINFORCEMENT BARS	SIZE (mm)	
Longitudinal - footing (bottom)	40	30 bars
Longitudinal - footing (top)	25	30 bars
Longitudinal (pedestal)	40	46 bars (each circle)
Stirrups (inside)	25	every 200mm
Stirrups (outside)	25	every 200mm
U-hoops	32	90 hoops

Source: The Author (2022)

3 THEORETICAL REASONING

This chapter will present the theoretical base behind the numerical models divided into four main sections of study: (1) the soil-structure interaction; (2) the embedded-ring foundation structural design; (3) the material models; and (4) the finite element method.

3.1 SOIL-STRUCTURE INTERACTION

Soil-structure interaction (SSI) regards the interdisciplinary fields around the static and dynamic events caused by the association of an accommodating soil with a stiff structure (KAUSEL, 2010). Differently from considering the foundation as supported by a rigid surface, the SSI allows the behaviour of the structure to be studied considering that it moves along with the soil. An analysis with SSI aims to provide the actual displacements of the foundation-structure set and their internal forces (VELLOSO; LOPES, 2011). As Rebello (2008) puts it, when the foundation is dimensioned following the traditional procedure, it is taken as a separate entity from the soil. Therefore, there is a lack of compatibility between the structure's strains and the soil's. When compatibility exists, meaning that the SSI is considered, the stresses are redistributed over the foundation.

There are two common ways to implement the SSI in a finite element structural analysis. One is to model the soil mass as a semi-infinite mesh of finite elements attached to the structure (see Figure 29a). This continuum strategy follows the Elasticity Theory and allows the consideration of complex characteristics of soil behaviour. Another method is Winkler's model, where the soil is discretely represented by springs (see Figure 29b). It is a greater simplification of the soil behaviour than its continuum

Figure 29 – Soil representation models.

(a) Continuum. (b) Winkler.

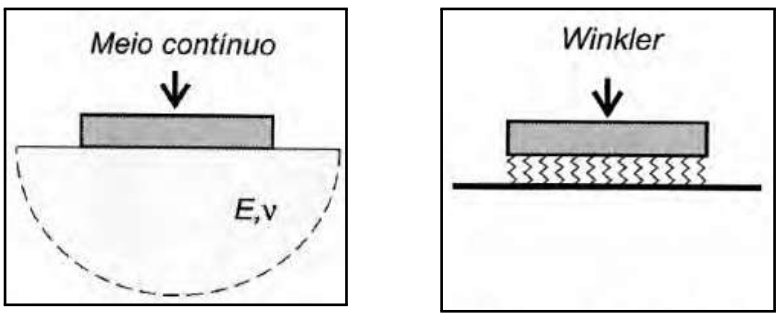

Source: Velloso e Lopes (2011)

counterpart. However, given the difficulty in acquiring the elastic parameters of the soil, it is regarded as presenting results as reliable as the more sophisticated and computationally expensive elastic continuum model by Berberian (2016) *APUD* (RODRIGUES, 2019). Therefore, this work chose Winkler's model to implement SSI in the analysis. After a brief overview of the model's theory, the SSI configuration as it was implemented in the research will be presented.

Contact pressures - the resulting stresses on the soil-structure interface (see Figure 30) - are proportional to the settlements in Winkler's model. This proportionality relationship is translated through the modulus of subgrade reaction, k_V, which defines the elastic behaviour of the soil. In the model, the idealised springs work independently amongst themselves. Each one will displace only due to a force applied directly above the node it supports, but not the one its neighbour does (Figure 31), establishing the force-displacement relationship of the spring coefficient. This lack of interaction confines the deformation of the foundation only to the loaded regions and poses a deficiency in the model. Following an American Concrete Institute (ACI) recommendation indicated by Rodrigues (2019), it can be diminished by doubling the k_V value for the boundary of the structure. This strategy minimises the discontinuity effect of the foundation settlement.

Figure 30 – Contact pressures.

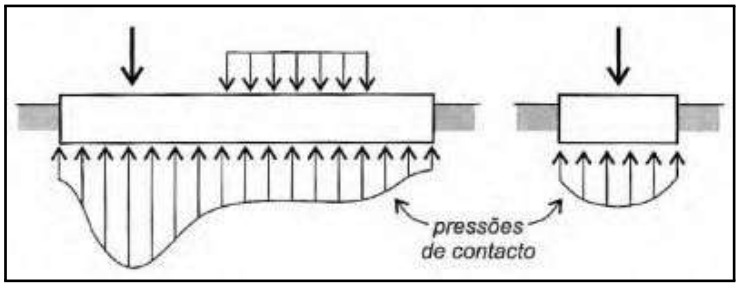

Source: Velloso e Lopes (2011)

Figure 31 – Spring behaviour.

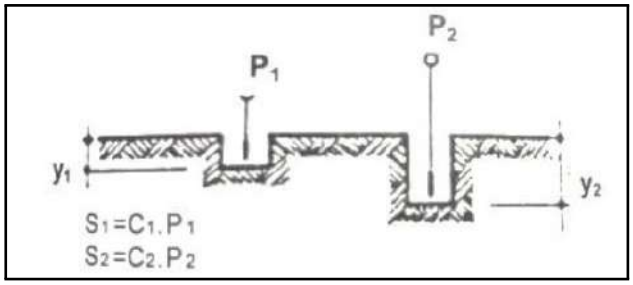

Source: Berberian (2016 apud RODRIGUES, 2019)

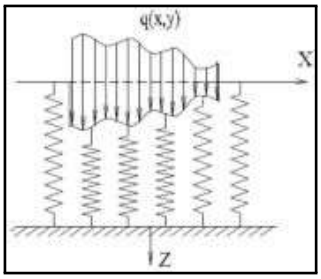

Source: Chandra (2014)

The horizontal modulus of subgrade reaction (k_H) can be appraised from a relationship between the vertical modulus (k_V) and the Poisson coefficient (ν):

$$k_H = k_V \cdot \nu \tag{1}$$

where ν ranges from 0,125 to 0,5 for sand soils and from 0,20 to 0,40 for clay soils, according to Rodrigues (2019). Considering the dense study performed by the researcher, where he assessed the influence that the variability of the subgrade reaction modulus posed on the contact stresses and internal forces of the foundation, the parameters and conditions for the SSI used in the present work were based on the conclusions presented. They are displayed in Figure 32 below, values and descriptions to follow, and refer to a practically rigid soil, with ν = 0.2. Note that the parameters informed are the *moduli* of subgrade reaction of each surface or edge: *Abaqus* will convert the values applied to entire regions to the spring stiffness coefficients of each node present in the region.

Figure 32 – Schematic of SSI configuration in the models.

(a) Springs in horizontal directions.

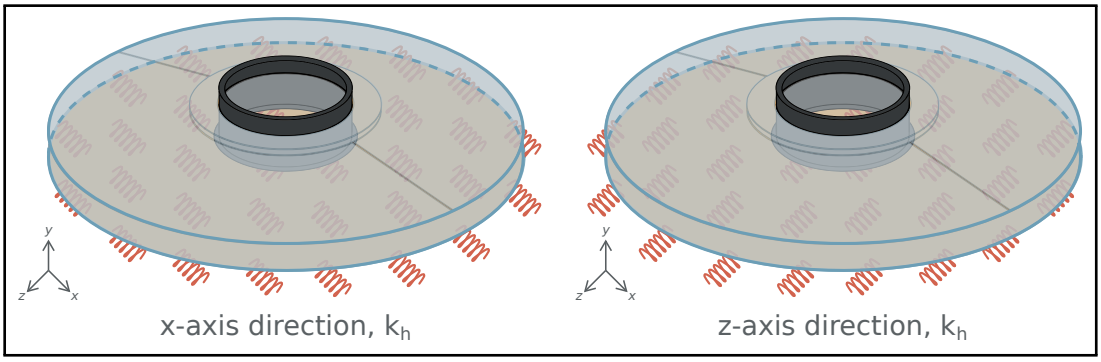

(b) Springs in vertical direction.

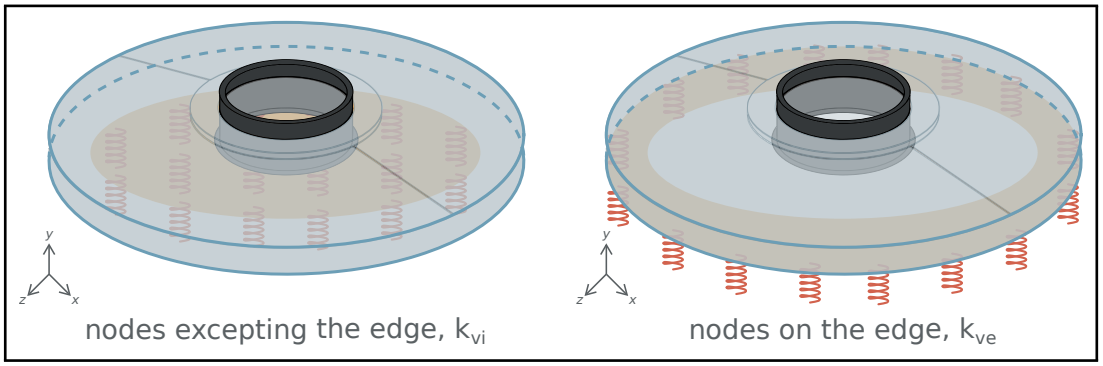

Source: The Author (2022)

Adopted parameters:

$k_H = 32000\,kN/m^2/m$: horizontal modulus of subgrade reaction for the entire bottom surface of the foundation, constraining movement in both *x* and *z* horizontal directions;

$k_{Vi} = 160000\,kN/m^2/m$: vertical modulus of subgrade reaction for the base of the foundation, excepting the boundary;

$k_{Ve} = 320000\,kN/m^2/m$: vertical modulus of subgrade reaction for the boundary of the foundation bottom.

A crucial aspect of the SSI is that the soil reaction must only be active under compression. In practical terms of the analysis, this meant implementing nonlinear springs in *Abaqus* that could behave differently depending on the nature of the stress (Section 4.1.1 will bring the procedure in detail). However, according to the results in the study performed by Rodrigues (2019), applying horizontal springs only to the compressed region of the foundation made no significant difference to the analysis versus horizontally constraining the entire area. For that reason, only the vertical springs were programmed to cease reaction under tensile forces.

3.2 EMBEDDED-RING FOUNDATION STRUCTURAL DESIGN

Designing a structural foundation involves both geotechnical and structural aspects. Therefore, the following topics will first comment on the main geotechnical features required to establish the preliminary geometry and then describe the process undertaken to design the steel reinforcement.

Regarding the loading, wind loads are taken as static-equivalent and, together with the weight of the turbine-tower set, transported to the top of the foundation for the design (Figure 33a). The result is the set of loads displayed in Figure 33b with corresponding values in Table 7. Those were given by (SVENSSON, 2010) as design values for the Vestas V-90, 2MW wind turbine. Additionally, weights must be considered from the foundation itself and from the soil backfill (Table 8). Figure 34a shows an abstraction of the backfill configuration over the foundation. For simplicity, a uniform load distribution was considered (see Figure 34b). The self-weight was internally calculated and applied to the analyses through the finite element software (the value in Table 8 is, therefore, a hand-calculation estimate).

Figure 33 – Wind and turbine loads on top of the foundation.

(a) Schematic: from the turbine to the foundation. (b) Resulting loads on the foundation top.

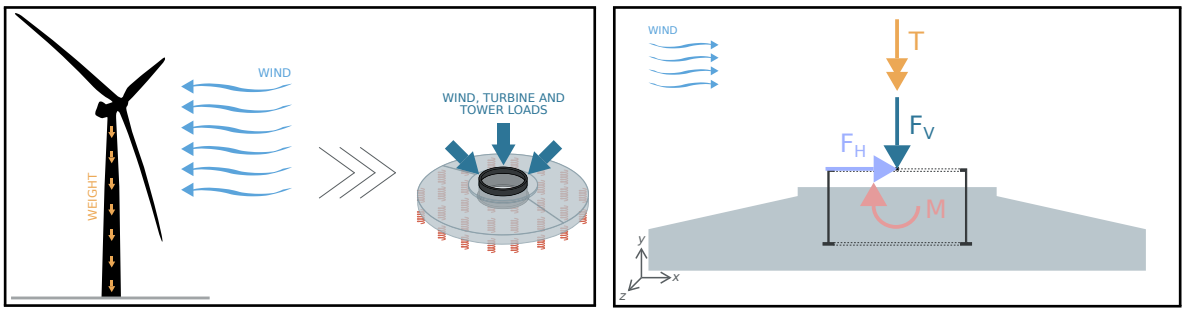

Source: The Author (2022)

Table 7 – Wind turbine loads.

F_V (kN)	F_H (kN)	M (kN.m)	T (kN.m)
3510	797	63825	1642

Source: Svensson (2010)

Table 8 – Weight loads.

Self-weight - sw (kN)	Soil backfill weight (kN/m²)
7636.8	14.4

Source: The Author (2022)

Figure 34 – Soil backfill load.

(a) Real backfill load distribution. (b) Uniform backfill load distribution.

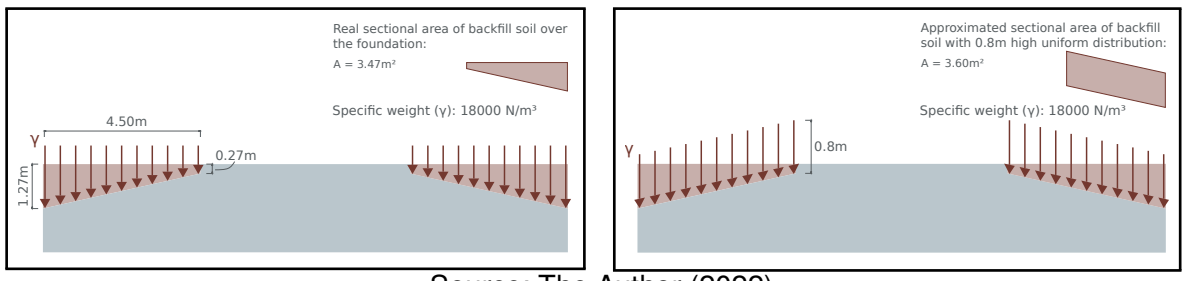

Source: The Author (2022)

3.2.1 General aspects

The geotechnical design stage verifies the deformations and bearing capacity of the soil upon which the foundation will be mounted. Since the foundation dimensions studied in this work were previously defined by Svensson (2010), this phase will not

be detailed here. Instead, only key aspects regarding bearing capacity and stability analysis will be covered for context.

To start with, Day (2005) defines bearing capacity failure as the type caused by excess shear stresses in the soil compared to its shear strength. Then, via an expression (Equation 2) derived by Terzaghi (DAY, 2005), dependent on soil parameters, foundation dimensions and load values, the bearing capacity of the soil ($\boldsymbol{q_{ult}}$) supporting a shallow foundation can be estimated. Following that, the chosen dimensions can be verified by calculating the actual pressure on the ground ($\boldsymbol{\sigma_{ultsoil}}$) through Equation 3 and comparing it with $\boldsymbol{q_{ult}}$ ($\boldsymbol{\sigma_{ultsoil}} < \boldsymbol{q_{ult}}$).

$$q_{ult} = cN_c + \frac{1}{2}\gamma_t D_f N_q \tag{2}$$

$$\sigma_{ultsoil} = \frac{Q_{ult}}{BL} \tag{3}$$

where:

$\boldsymbol{q_{ult}}$: ultimate bearing capacity;

$\boldsymbol{Q_{ult}}$: vertical concentric load;

$\boldsymbol{\sigma_{ultsoil}}$: acting pressure on the ground;

$\boldsymbol{B}$: width;

$\boldsymbol{L}$: length;

γ_t: total unit weight of the soil ;

$\boldsymbol{D_f}$: vertical distance from ground surface to bottom of foundation;

$\boldsymbol{c}$: soil cohesion;

$\boldsymbol{N_c}$, $\boldsymbol{N_\gamma}$, $\boldsymbol{N_q}$: dimensionless bearing capacity factors.

Besides the soil shear capacity, the foundation dimensions must be verified to safeguard it against overturning. Many methods are available for this, one of which guarantees the load eccentricity, $\boldsymbol{e}$, keeps within a specific region limited by a fraction of the foundation width or diameter. The exact fraction value varies with standards and researchers. Rodrigues (2019) mentions how the CFMS (*Comité Français de Mécanique*

des Sols et de Géotechnique) sets a minimum requisite of 50% of the foundation area under compression. Considering that specification, the equivalent eccentric load, P, should be positioned no further than r_2 from the foundation's centre (Figure 35). r_1, in Figure 35, corresponds to the middle quarter rule for circular sections, according to which the entire base will be compressed if $e < r_1 = R/4$ (Region A). r_2, according to Rodrigues (2019), corresponds to $0.589R$. Therefore, if $0 < e = 0.589R$ (Region B), the foundation should remain grounded even though parts might lose their grip on the soil.

Figure 35 – Load eccentricity in a shallow circular foundation.

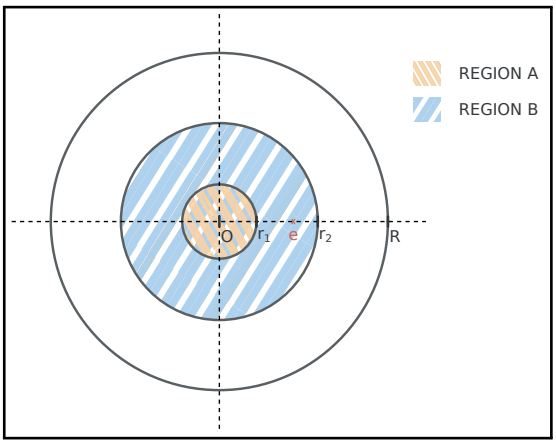

Source: Adapted from Spernau (2008 apud RODRIGUES, 2019)

The geotechnical design establishes the preliminary dimensions for the foundation: it sets the geometry on which the structural design, presented in the next section, will be performed.

**The content of the following pages is not to be considered part of a construction project. The intended goal was to dimension steel reinforcement bars to strengthen the foundation's capacity to resist internal stresses. Construction processes and effects were not taken into account.*

3.2.2 Steel reinforcement design

The steel reinforcement design process was carried out separately for the pedestal and the footing. The first was assumed to be a reinforced concrete column, following (SHABAN, 2017), whose reinforcement was determined through standardised procedures. On the other hand, the latter was dimensioned using sectional internal stresses obtained from the finite element model itself. Both procedures will be described now.

3.2.2.1 Pedestal

According to Shaban (2017), the reinforcement design of the pedestal can mirror the process devised for reinforced concrete columns. Following the prescriptions in ABNT (2014), the design process focused on determining the longitudinal and transverse reinforcements needed to resist bending with axial force (other possible failure agents such as torsion, pull-out and bursting forces were neglected in this study).

First, it was necessary to verify that the second-order effects could be ignored and to determine the bending moment value to be considered acting on the section (remember that the loads from (SHABAN, 2017) were already factored), according to the schematic summary in Figure 36). Then, the longitudinal reinforcement for the column was dimensioned with the help of educational software P-Calc (Sander David Cardoso Junior, -). The circular section was assumed to have a concrete cover, c, of 50mm, and two circles of longitudinal bars, one outside and another inside the embedded ring, both encircled by transverse reinforcement. This layout aligns with common design practice, according to (SHABAN, 2017).

Figure 36 – Loads for the longitudinal reinforcement.

(a) Pedestal. (b) Isolated member. (c) Pedestal section.

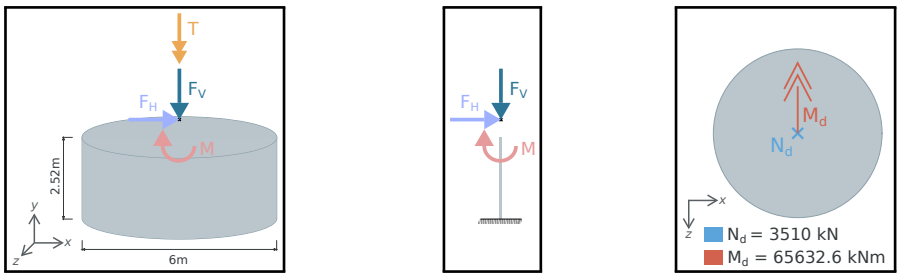

Source: The Author (2022)

When the numbers of longitudinal bars and their diameters are assigned, the software determines the strength interaction diagram for the current section. It can then check if the designed section can resist the pair of axial force and bending moment. The result comprised 46 longitudinal bars of 40mm for each circle, totalling 92 steel bars. Their anchorage development length was also determined in accordance with ABNT (2014), as was the transverse reinforcement. Since the amount of shear force the concrete alone could resist surpassed the value of the applied force, the reinforcement was necessary only to confine the longitudinal bars. Thus, 25mm bars were placed around the longitudinal bars' circles every 200mm. Figure 37 displays the final section arrangement.

Figure 37 – Reinforcement bars arrangement in the pedestal.

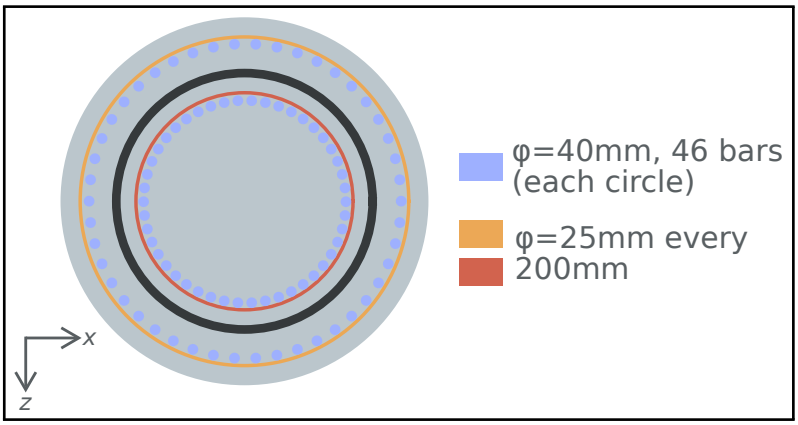

Source: The Author (2022)

3.2.2.2 Footing

The behaviour of reinforced concrete was assumed to follow the well-established diagram (Figure 38) that ignores tensile resistance and simplifies the compressive distribution of stresses on the concrete to a rectangle. To apply this concept, sections were defined in *Abaqus* along the *x-axis* of the foundation from which the resulting stresses should be extracted and manipulated to function as the applied axial loads and bending moments. 'Model I' was the one used to obtain those stresses (a preliminary summary of each model's assumptions was shown in Figure 4, and details on their differences will be presented in Section 4.1): a linear model with soil structure interaction and perfect adherence between the concrete and the embedded ring.

Figure 38 – Adopted reinforced concrete behaviour.

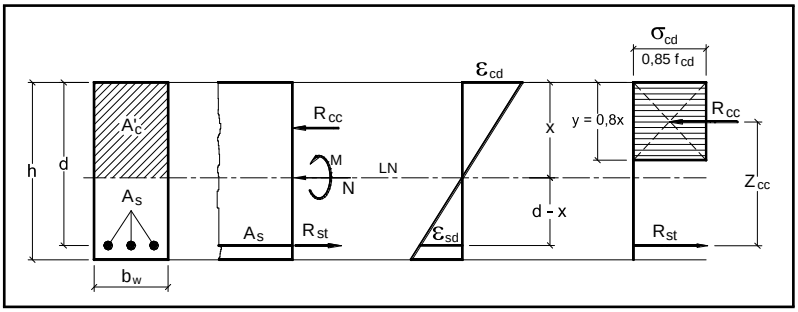

Source: Bastos (2020)

The sections are identified in Figure 39. σ_{xx} (normal to the sections, $S11$ for *Abaqus*) and τ_{xy} (shearing the section, $S12$) stresses were collected for all the elements in each of the sections: σ_{xx} for the longitudinal reinforcement and τ_{xy} for the transverse bars. Then, the sectional stress data was turned into equivalent normal forces and bending moments.

Figure 39 – Sections for longitudinal reinforcement design.

(a) Loads and *x-axis* directions on model.

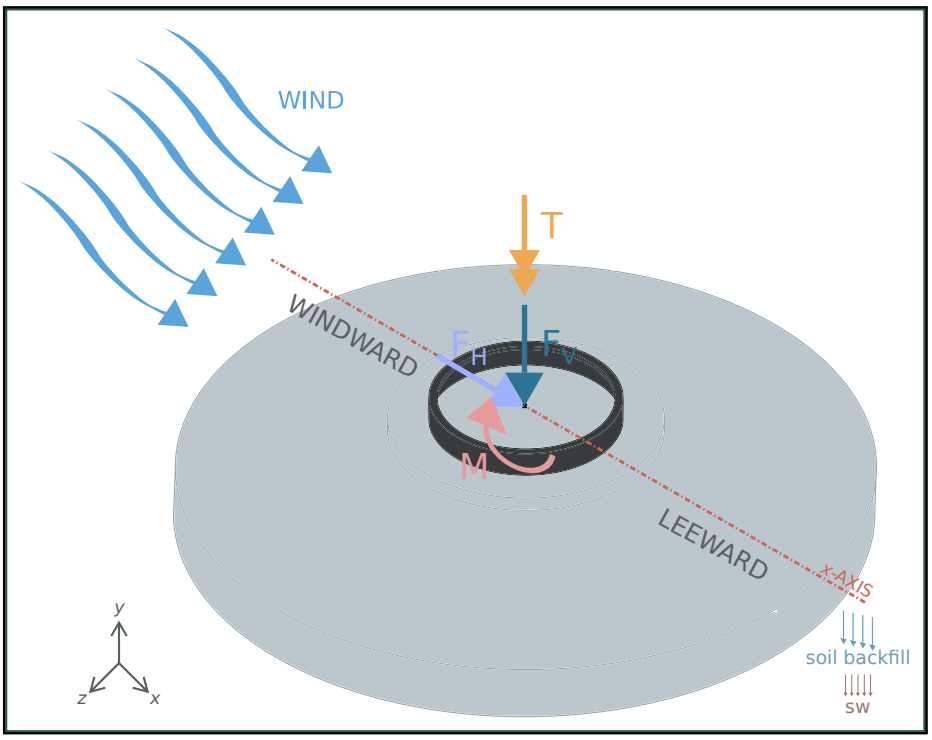

(b) Sections positioning.

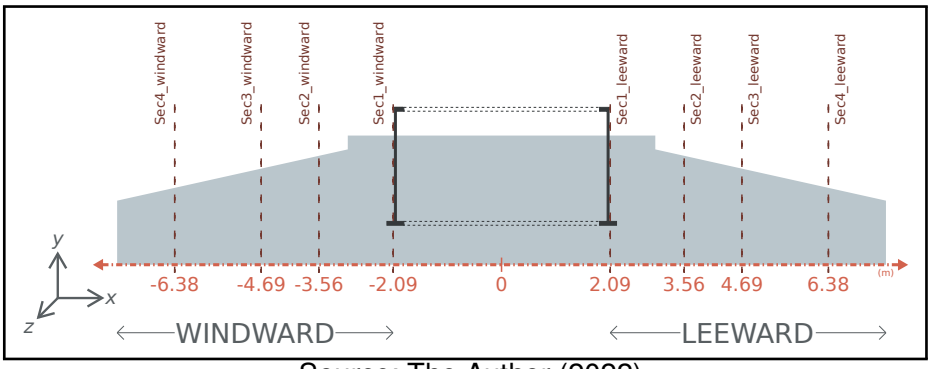

Source: The Author (2022)

For the longitudinal reinforcement, the σ_{xx} ($S11$) stress distributions in each section (Figure 40) were first transformed into nodal forces and finally into resulting axial loads (N) and bending moments (M) (Figure 41). With these values at hand, the reinforcement could be calculated based on the theory above of reinforced concrete sections under bending and axial loads. Looking at Figures 39a and 41, it is easy to understand the reason why the bending moments for the leeward sections are positive while the ones for the windward sections are negative: the direction of the wind loads. Because of that, the leeward sections will be used to dimension the positive (inferior) rebars and the ones on the windward side to the negative (superior) bars (Figure 42). The same rationale was applied by Rodrigues (2019).

Figure 40 – Sectional radial stresses - σ_{xx} $(S11)$.

(a) Windward sections.

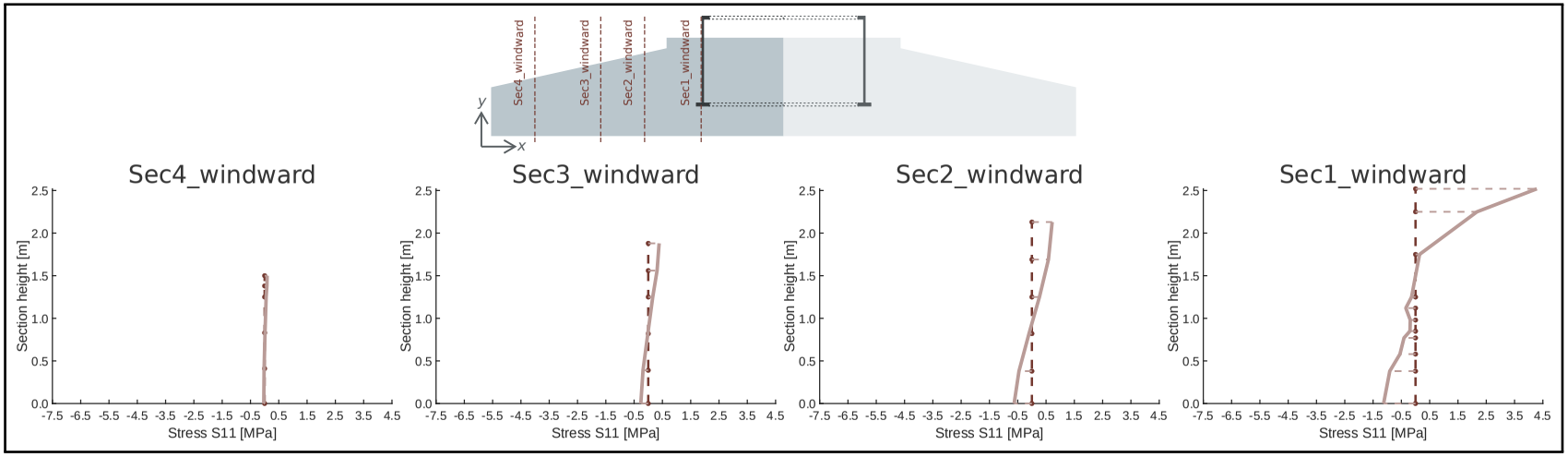

(b) Leeward sections.

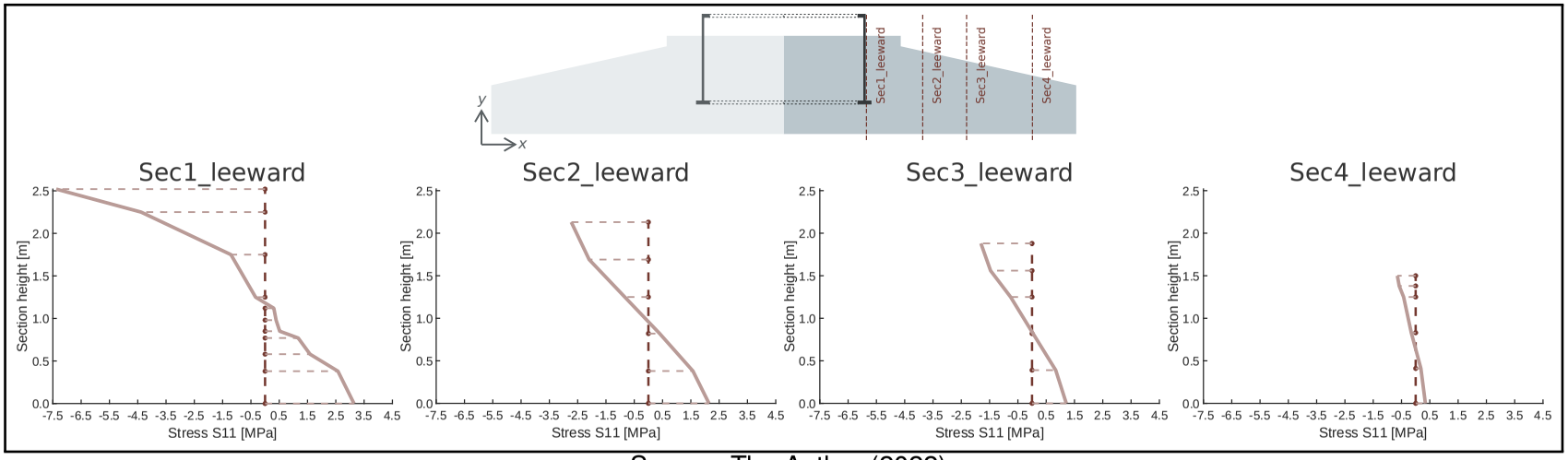

Source: The Author (2022)

Figure 41 – Sectional axial loads (N) and bending moments (M).

(a) Windward sections.

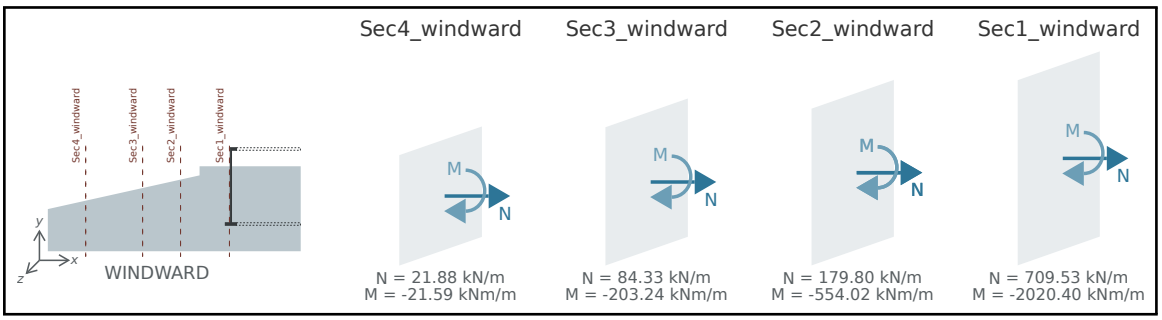

(b) Leeward sections.

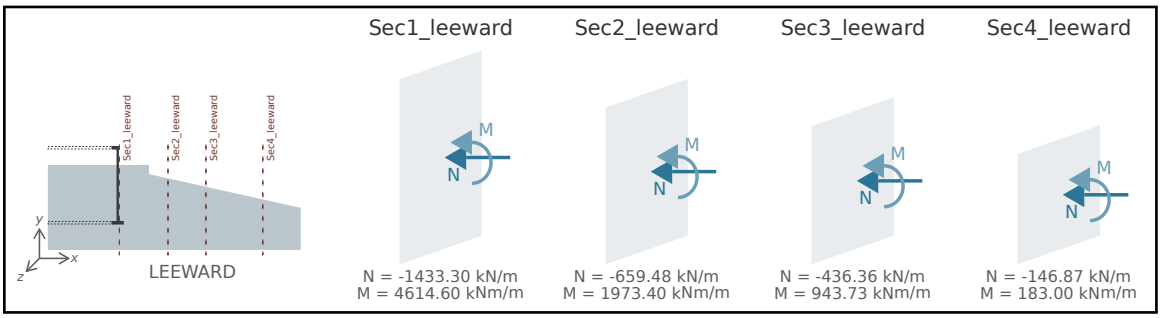

Source: The Author (2022)

Figure 42 – Positive and negative rebars.

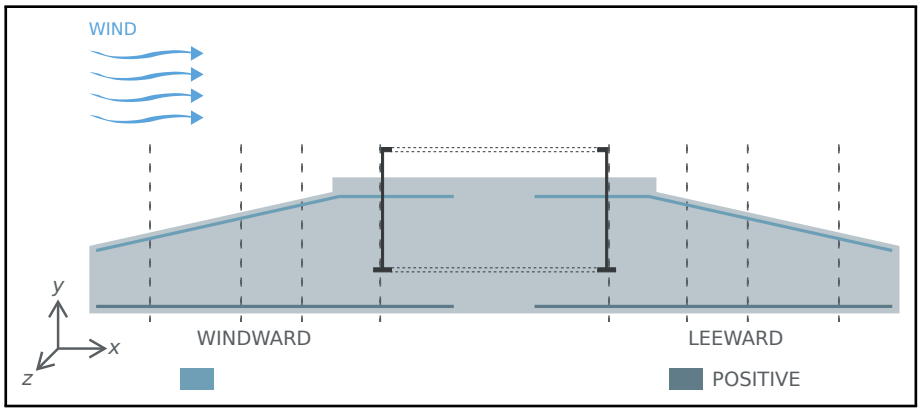

Source: The Author (2022)

Table 9 shows the resulting necessary area of steel required for each section and the number of bars it equalled for each corresponding circumference, considering 25mm bars for the negative and 40mm bars for the positive reinforcement. The same number of bars will be placed from the centre to the foundation's edge for simplification purposes. Therefore, 30 bars of 25mm were placed radially on the top of the footing, while 30 bars of 40mm were distributed on the bottom (Figure 43).

Regarding the transverse reinforcement, the shear stresses, τ_{xy} ($S12$), were also transformed into the total shear force acting over the section. However, the values

were so small that only section *'Sec1_leeward'* required reinforcement and was still less than the minimum rate set by ABNT (2014). Therefore, the transverse rebars were ignored for the footing.

Table 9 – Necessary steel reinforcement.

	Windward sections				**Leeward sections**			
Bars' diameter (mm)	ϕ **= 25**				ϕ **= 40**			
Section steel (cm²/m)	0.08	1.60	4.12	11.02	28.40	14.84	7.04	1.20
# bars per circumference	1	10	19	30	30	27	17	4
Total # of bars	**30 bars**				**30 bars**			

Source: The Author (2022)

Figure 43 – Arrangement of longitudinal reinforcement.

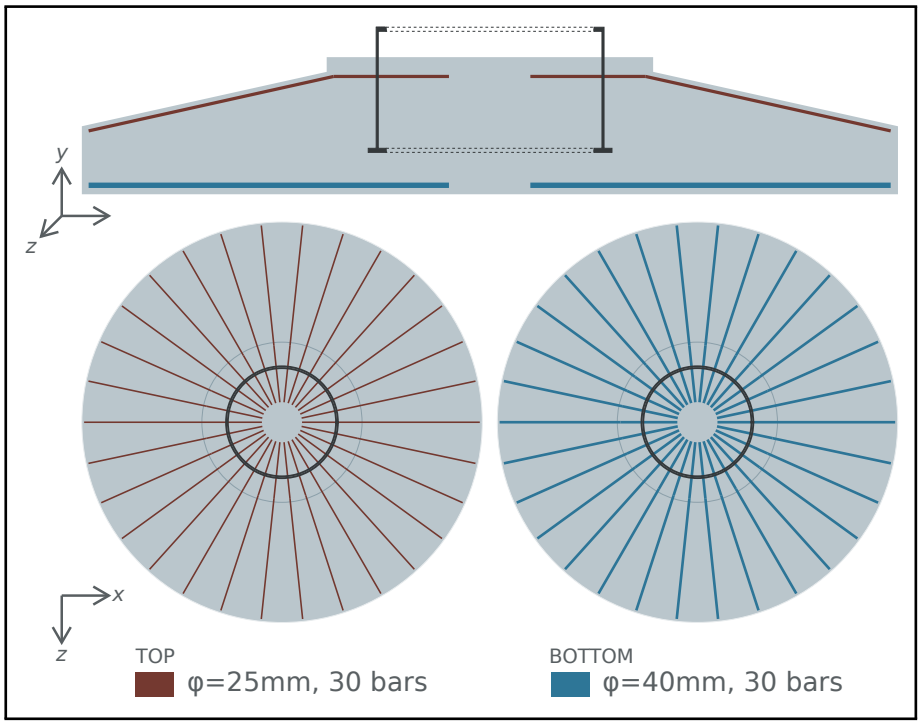

Source: The Author (2022)

3.2.2.3 Embedded-ring anchorage

An additional type of steel reinforcement appears in embedded-ring foundations to assist in its load-transfer mechanism. It takes the form of a hoop and wraps the bottom of the ring to provide anchorage for it onto the concrete (Figure 44). The determination of this type of reinforcement for the foundation model followed the rationale presented by

Svensson (2010), based on theories of Mechanics of Materials. As a result, 90 U-hoops were distributed around the steel ring, as illustrated in Figure 45.

Figure 44 – Project detail - U-hoop.

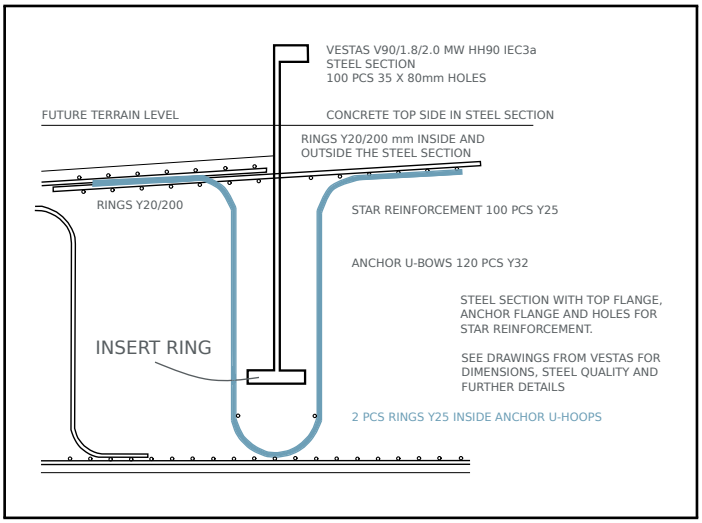

Source: Adapted from Hassanzadeh (2012)

Figure 45 – Arrangement of reinforcement with U-hoops.

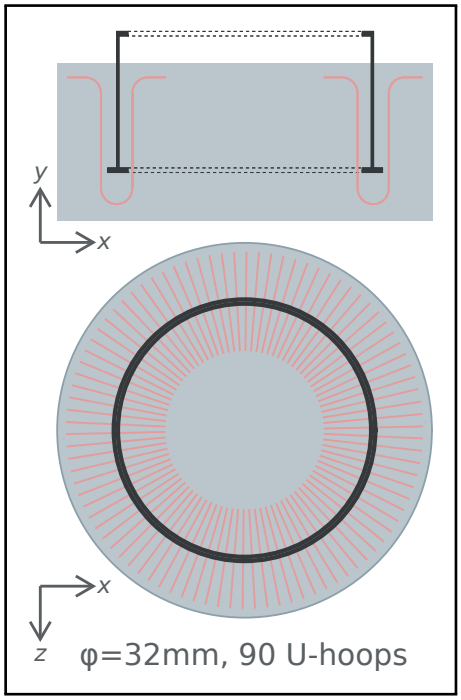

Source: The Author (2022)

3.3 MATERIAL MODELS

This section will address the physical behaviours of the concrete and the steel when subjected to stresses and deformations. For that, the constitutive model adopted

for each material will be presented.

3.3.1 Concrete

Several theoretical models are available to describe concrete's nonlinear physical behaviour. The reason lies in its complexity being a quasi-brittle material, therefore subjected to abrupt failure following a fracture process (Figure 46), which hampers the collection of post-peak experimental data. Combined with its heterogeneity and highly manually dependent resistance tests, it is improbable to have a single model that fits every analysis purpose.

Figure 46 – Quasi-brittle material behaviour.

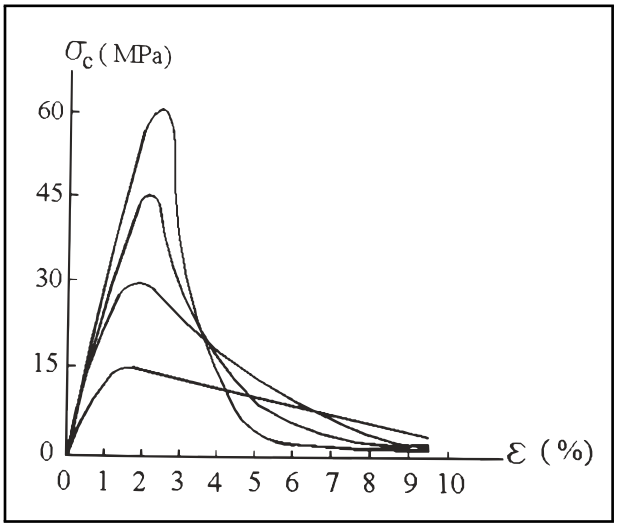

Source: Assan (2010)

In this work, a plasticity-based damage model was chosen due to (1) its capacity to represent the loss of stiffness in the concrete; (2) its customary application in finite element analyses of wind turbine foundations; and (3) its availability in the finite element software used for the numerical modelling (*Abaqus*). For easiness, the model used will be referred to as CDP (concrete damaged plasticity), its denomination in *Abaqus*.

3.3.1.1 CDP: a damage-plasticity model

Plasticity covers load-inflicted displacements and deformations that cannot be recovered by unloading. The flow plasticity theory, used in the CDP, works with the relationship between a stress state and a corresponding strain rate, not directly between stress and strain states. Building a plasticity-based constitutive model requires the

definition of a yield surface, a flow rule (the plastic stress-strain law) and a hardening rule. The first can be generally defined as:

$$F(\boldsymbol{\sigma}) \leq 0 \tag{4}$$

to mean a loading function that bounds all stress states and allows for no stress values outside this bound (BORST et al., 2012). Stress states verifying the inequality sign are inside the yield contour (Figure 47) and only cause elastic deformations. On the other hand, the states for the equality sign are on the yield contour and establish the onset of plastic deformations.

Figure 47 – Yield surface in three-dimensional stress-space (*von Mises* yield criterion).

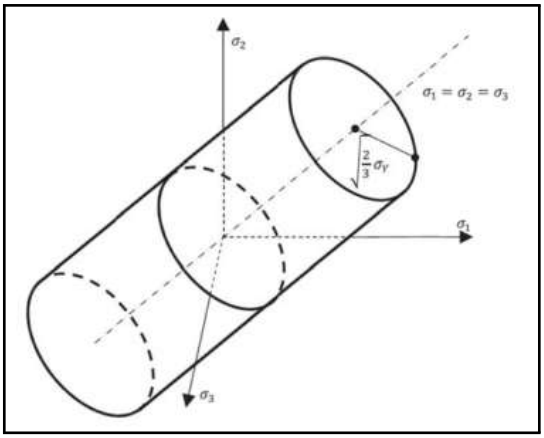

Source: Adeeb (2020)

However, the unrecoverable deformations will only occur if the stress state on the yield contour remains thus for at least one virtual time increment, following Prager's consistency condition. The implication is that not only

$$F(\boldsymbol{\sigma}) = 0 \tag{5}$$

must happen, but also

$$\dot{F}(\boldsymbol{\sigma}) = 0. \tag{6}$$

With $\boldsymbol{n}$ the gradient of the yield function,

$$\boldsymbol{n} = \frac{dF}{d\boldsymbol{\sigma}}, \tag{7}$$

and therefore perpendicular to the yield surface at the stress point in question, Equation 6 can be written as:

$$\boldsymbol{n} : \dot{\boldsymbol{\sigma}} = 0. \tag{8}$$

When plastic deformations start, the stress-strain elastic relation,

$$\boldsymbol{\sigma} = \boldsymbol{D^e} : \varepsilon, \tag{9}$$

where $\boldsymbol{D^e}$ is the elastic stiffness tensor, only works for the elastic domain:

$$\boldsymbol{\sigma} = \boldsymbol{D^e} : \varepsilon^{\boldsymbol{e}}. \tag{10}$$

Since the total strain ε is made up of both elastic (ε^e) and plastic (ε^p) strains,

$$\boldsymbol{\varepsilon} = \boldsymbol{\varepsilon^e} + \boldsymbol{\varepsilon^p}, \tag{11}$$

the stress-strain relation can be written as:

$$\boldsymbol{\sigma} = \boldsymbol{D^e} : (\boldsymbol{\varepsilon} - \boldsymbol{\varepsilon^p}). \tag{12}$$

Regarding the plastic strain rate ($\dot{\varepsilon}^p$), it is defined as a product of a scalar that sets its magnitude (the plastic multiplier, $\dot{\lambda}$), with a vector that sets the direction of the plastic flow ($\boldsymbol{m}$):

$$\dot{\boldsymbol{\varepsilon}}^{\boldsymbol{p}} = \dot{\lambda}\boldsymbol{m}. \tag{13}$$

If Equation 12 is differentiated with respect to a virtual time and both sides of it are premultiplied by $\boldsymbol{n}$, combining the result with Equations 13 and 8 allows for the magnitude of the plastic flow to be written as:

$$\dot{\lambda} = \frac{(\boldsymbol{n} : \boldsymbol{D^e} : \dot{\boldsymbol{\varepsilon}})}{(\boldsymbol{n} : \boldsymbol{D^e} : \boldsymbol{m})}. \tag{14}$$

Finally, from Equation 14, it is possible to obtain a linear flow rule:

$$\dot{\boldsymbol{\sigma}} = (\boldsymbol{D}^e - \frac{(\boldsymbol{D}^e : \boldsymbol{m}) \otimes (\boldsymbol{D}^e : \boldsymbol{n})}{\boldsymbol{n} : \boldsymbol{D}^e : \boldsymbol{m}}) : \dot{\boldsymbol{\varepsilon}}. \tag{15}$$

Flow rules can be associated or nonassociated. The first follows the normality rule, meaning the plastic flow direction ($\boldsymbol{m}$) is collinear to the gradient to the yield surface ($\boldsymbol{n}$). It implies that the plastic flow is normal to the surface. Considering the collinearity of the direction vectors $\boldsymbol{m}$ and $\boldsymbol{n}$ in Equations 13 and 7, the plastic flow can be written as:

$$\dot{\boldsymbol{\varepsilon}}^{\boldsymbol{p}} = \dot{\lambda}\frac{dF}{d\boldsymbol{\sigma}}. \tag{16}$$

For nonassociated flow rules, which agrees better with the behaviour of soils, rocks and concrete (BORST et al., 2012), the normality rule does not apply. Instead, what occurs for a majority of them is the existence of a scalar-valued function, $G(\boldsymbol{\sigma})$, referred to as the plastic potential function, whose gradient is collinear to the plastic flow direction, $\boldsymbol{m}$:

$$\boldsymbol{m} = \frac{dG}{d\boldsymbol{\sigma}}. \tag{17}$$

Therefore, the nonassociated plastic flow can be defined in terms of the potential flow as:

$$\dot{\boldsymbol{\varepsilon}}^{\boldsymbol{p}} = \dot{\lambda}\frac{dG}{d\boldsymbol{\sigma}}. \tag{18}$$

The last main requisite for a model based on plasticity, the hardening rule, controls the evolution of the yield surface: unless it is a perfectly-plastic case, the yield surface may change size, shape and position. Through so-called hardening parameters, which change during plastic deformation, the yield function starts to depend upon the loading history and not only on the stress states:

$$F(\boldsymbol{\sigma}, k) \leq 0. \tag{19}$$

In Equation 19, k represents the possible hardening parameters, which may be scalars or higher-order tensors. If k is a scalar, the hardening rule (Equation 19) will cause the yield surface to expand uniformly without translating or rotating, characterising isotropic hardening (Figure 48a). If $\boldsymbol{k}$ is a second-order tensor, such that $F = F(\boldsymbol{\sigma} - \boldsymbol{k})$, the yield surface will translate while maintaining its shape and orientation, characterising

kinematic hardening (Figure 48b). If, however, $\boldsymbol{k}$ assumes different values depending on the loading history or range of stress, the evolution of the yield surface is extremely load-path dependent, which will cause nonuniform size changes in the surface, characterising independent hardening (Figure 48c).

Figure 48 – Hardening rules.

(a) Isotropic hardening.

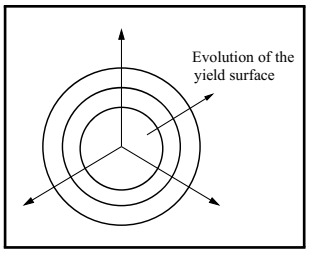

Source: Borst et al. (2012)

(b) Kinematic hardening.

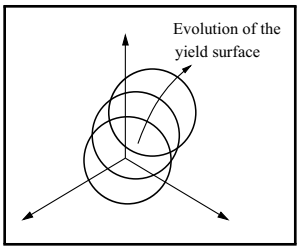

Source: Borst et al. (2012)

(c) Independent hardening.

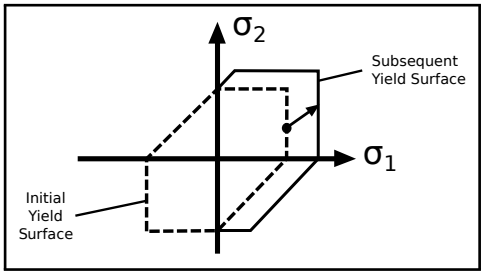

Source: Ohtani e Chen (1988)

Meanwhile, damage mechanics assimilate material degradation by reducing elastic stiffness. An internal variable, called damage parameter (d), increases monotonically by an evolution law that captures the disintegration of the material. It characterises the system's state by assuming values from 0, when the structure is intact, to 1, when it has completely lost its strength. The stress-strain relation in this branch of mechanics is defined as:

$$\boldsymbol{\sigma} = (1 - d)\boldsymbol{D}^{e}\boldsymbol{\varepsilon}, \tag{20}$$

where $\boldsymbol{D}^{e}$ is the stiffness tensor for the intact material, $\boldsymbol{\sigma}$ is the stress tensor, and ε is the strain tensor. The effective stress, $\overline{\boldsymbol{\sigma}}$, which is defined as the stress acting only over the intact material located between cracks (BORST et al., 2012), is defined as:

$$\overline{\boldsymbol{\sigma}} = \boldsymbol{D}^{e}\varepsilon. \tag{21}$$

Therefore, Equation 20 can be written as:

$$\boldsymbol{\sigma} = (1 - d)\overline{\boldsymbol{\sigma}}. \tag{22}$$

The damage field provides two primary methods to reproduce concrete cracks (BORST et al., 2012): discrete and smeared. The first focuses on the values of tensile nodal forces against the maximum tensile resistant force to determine when a crack occurs. If affirmative, the node in question is “duplicated”, and a subsequent geometrical discontinuity is created (see Figure 49a). This continuous change of the mesh topology is an issue, mainly due to the high computational cost associated with the multiplication of nodes (KWAK; FILIPPOU, 1990).

Distinctively, the smeared crack model does not alter the mesh topology to consider fracture in a structure, thus maintaining the continuity of the displacement field. Moreover, instead of representing a single crack, it spreads several thinly-spaced cracks in one element perpendicularly to the principal stress direction, as shown in Figure 49b (KWAK; FILIPPOU, 1990). However, since the method assumes that the cracked solid is a continuum still, stress and strain relations still apply. In this context, the mechanism used to account for the loss of strength is substituting the initial isotropic relation when cracking arises by an orthotropic one. This technique is more computationally efficient than the discrete crack model (BORST et al., 2012). However, it creates a tendency for the inelastic strains to localise along a row of finite elements, causing energy dissipation to depend on the element size, meaning that this method is also mesh-dependent, which must be abated by a ‘localisation limiter’ (EARIJ et al., 2017).

Figure 49 – Crack models.

(a) Discrete crack. (b) Smeared crack.

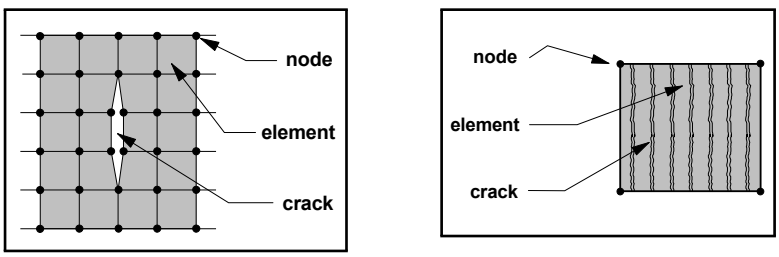

Source: Adapted from Kwak e Filippou (1990)

Finally, according to Borst et al. (2012), a plasticity-based damage model can be built by assuming that (1) plasticity only applies to the intact matrix material and that (2)

the stress-strain relation is governed by Equation 23 below, similar to Equation 20 with the exception that the elastic strain is the one present:

$$\boldsymbol{\sigma} = (1 - d)\boldsymbol{D^e}\boldsymbol{\varepsilon^e}. \tag{23}$$

The effective stress then becomes:

$$\overline{\boldsymbol{\sigma}} = \boldsymbol{D^e}\boldsymbol{\varepsilon^e}, \tag{24}$$

and, to fulfil the assumptions, is the one to be considered for the yield function (in Equation 19) and the flow rule (in Equation 18) instead of the Cauchy stress tensor $\boldsymbol{\sigma}$.

In the CDP, the association between the two fields is sealed by the hardening variables, which characterise the deterioration in tension and compression independently (independent hardening): $\widetilde{\varepsilon}_t^p$ and $\widetilde{\varepsilon}_c^p$, tensile and compressive equivalent plastic strains, respectively. They control both the evolution of the yield surface and the degradation of the elastic stiffness, considered isotropic, and increase in value to represent microcracking or crushing in the concrete.

The yield surface in the model is the one by Lubliner et al. (1989) (with modifications by Lee e Fenves (1998) to consider different evolution of strength under tension and compression). It is represented in Figure 50 and defined in terms of the effective stress ($\overline{\boldsymbol{\sigma}}$) and hardening variables ($\widetilde{\varepsilon}_t^p$, $\widetilde{\varepsilon}_c^p$) by Equation 25.

$$F = \frac{1}{1-\alpha}[\overline{q} - 3\alpha\overline{p} + \beta(\widetilde{\varepsilon}_t^p, \widetilde{\varepsilon}_c^p)\widehat{\overline{\sigma}}_{max} - \gamma - \widehat{\overline{\sigma}}_{max}] - \overline{\sigma}_c(\widetilde{\varepsilon}_c^p) \tag{25}$$

where:

$\overline{p} = -\frac{1}{3}\,tr(\overline{\boldsymbol{\sigma}})$: hydrostatic stress;

$\overline{q} = \sqrt{\frac{3}{2}\parallel dev(\overline{\boldsymbol{\sigma}}) \parallel}$: *von Mises* equivalent stress;

$\widehat{\overline{\sigma}}_{max}$: maximum principal effective stress;

$\overline{\sigma}_t(\widetilde{\varepsilon}_t^p)$: effective tensile cohesion stress;

$\overline{\sigma}_c(\widetilde{\varepsilon}_c^p)$: effective compressive cohesion stress;

$\alpha = \frac{(\frac{\sigma_{b0}}{\sigma_{c0}}) - 1}{2(\frac{\sigma_{b0}}{\sigma_{c0}}) - 1}; 0 \leq \alpha \leq 0.5$: dimensionless material constant;

$\frac{\sigma_{b0}}{\sigma_{c0}}$: ratio of initial biaxial compressive yield stress to initial uniaxial compressive yield stress (*default value: 1.16*);

$\beta = \frac{\overline{\sigma}_c(\widetilde{\varepsilon}_c^p)}{\overline{\sigma}_t(\widetilde{\varepsilon}_t^p)}(1-\alpha) - (1+\alpha)$: dimensionless material constant;

$\gamma = \frac{3(1-K_c)}{2K_c - 1}$: dimensionless material constant;

$K_c = \frac{q_{(TM)}}{q_{(CM)}}; 0.5 < K_c \leq 1$: ratio between second stress invariants on the tensile $q_{(TM)}$ and compressive $q_{(CM)}$ meridians, at initial yield for any value of the hydrostatic stress, such that the maximum principal stress is negative, $\widehat{\sigma}_{max}$<0 (*default value: 2/3*);

Figure 50 – CDP yield surfaces.

(a) Yield surfaces in the deviatoric plane for different values of K_c.

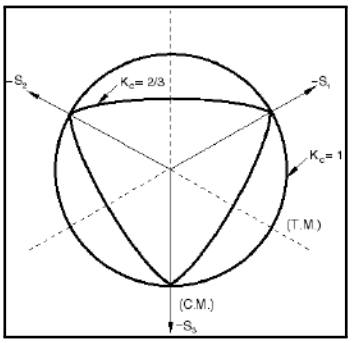

(b) Yield surface in plane stress.

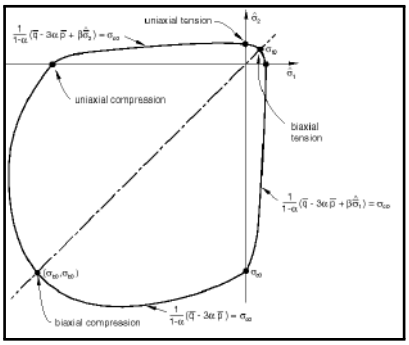

Source: Simulia (2017)

The potential flow adopted by the CDP is the nonassociated one:

$$\dot{\boldsymbol{\varepsilon}}^{\boldsymbol{p}} = \dot{\lambda}\frac{dG(\overline{\boldsymbol{\sigma}})}{d\overline{\boldsymbol{\sigma}}}, \tag{26}$$

with the *Drucker–Prager* hyperbolic function as the plastic potential flow, $G(\overline{\boldsymbol{\sigma}})$. This potential ensures that the flow direction is always uniquely defined (SIMULIA, 2017). It is described below:

$$G = \sqrt{(\epsilon\,\sigma_{t0}\,tan\psi)^2 + \overline{q}^2} - \overline{p}\,tan\psi, \tag{27}$$

where:

ψ: dilation angle in degrees measured in the *p–q* plane at high confining pressure (*value used: 40º, common in the literature*);

ϵ: eccentricity, which defines the rate at which the function approaches the asymptote (the flow potential tends to a straight line as the eccentricity tends to zero) *(default value: 0.1)*;

σ_{t0}: uniaxial tensile stress at failure (*from material entry data*);

3.3.1.2 CDP's uniaxial stress-strain behaviour and damage evolution

Now, assuming uniaxial loading conditions, which can be expanded to multiaxial, the CDP's stress-strain behaviour under tension and compression, along with its relationship regarding the hardening variables and damage evolution, will be described. Concerning the initial (undamaged) elastic stiffness, the CDP considers it to be the same (E_0) for both stress behaviours.

- Tensile behaviour

For the tensile behaviour of concrete, the model assumes a linear-elastic stress-strain relation until the failure stress is reached ($\boldsymbol{\sigma_{t0}}$). Then, the post-failure behaviour is modelled through tension stiffening to consider the strain-softening behaviour of the cracked concrete and to model the stress transfer between the reinforcement and the concrete. It can be done through a stress-cracking strain relation or a stress-cracking displacement relation. For a reason addressed at the end of this topic, this work was carried out with a stress-cracking strain ($\boldsymbol{\sigma_t}$ - $\boldsymbol{\varepsilon_t^{ck}}$) option, as pictured by Figure 51. Consider the following relations that sprung from the last section:

$$\varepsilon_{t0}^{e} = \frac{\sigma_t}{E_0}, \tag{28}$$

$$\varepsilon_{t,d}^{e} = \frac{\sigma_t}{[(1-d_t)E_0]}, \tag{29}$$

$$\widetilde{\varepsilon}_t^{ck} = \varepsilon_t - \varepsilon_{t0}^{e}, \tag{30}$$

$$\widetilde{\varepsilon}_t^{p} = \varepsilon_t - \varepsilon_{t,d}^{e}, \tag{31}$$

where:

ε_{t0}^{e}: elastic strain (undamaged);

$\varepsilon_{t,d}^{e}$: elastic strain (damaged);

$\tilde{\varepsilon}_{t}^{ck}$: cracking strain;

$\tilde{\varepsilon}_{t}^{p}$: equivalent plastic strain for cracked concrete.

From Equations 30 and 31, $\tilde{\varepsilon}_{t}^{p}$ can be written as:

$$\tilde{\varepsilon}_{t}^{p} = \tilde{\varepsilon}_{t}^{ck} + \varepsilon_{t0}^{e} - \frac{\sigma_t}{(1-d_t)E_0} = \tilde{\varepsilon}_{t}^{ck} - \frac{\sigma_t}{E_0}\left(\frac{1}{1-d_t} - 1\right) = \tilde{\varepsilon}_{t}^{ck} - \frac{d_t}{1-d_t}\varepsilon_{t0}^{e}. \tag{32}$$

Regarding the tensile damage evolution, it is directly determined by the tensile post-failure stress-cracking strain relationship (σ_t - ε_{t}^{ck}), and d_t is computed through:

$$d_t = 1 - \left(\frac{\sigma_t}{f_t}\right). \tag{33}$$

Figure 51 – CDP tensile behaviour.

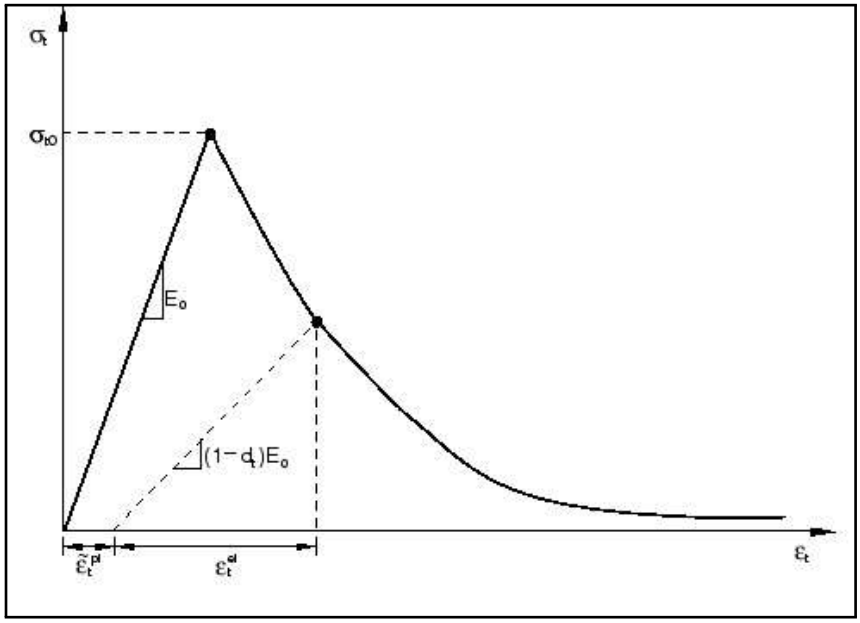

Source: Simulia (2017)

When a stress-cracking displacement relation is used to define tension stiffening, *Abaqus* calculates the plastic displacement, u_t^p, via the cracking displacement, u_t^{ck}, through Equation 34 below:

$$u_t^p = u_t^{ck} - \frac{d_t}{(1-d_t)}\frac{\sigma_t l_0}{E_0}, \tag{34}$$

where the specimen length, l_0, is taken as one unit length (SIMULIA, 2017). However, for the SI units applied in the models, l_0=1m while u_t^{ck} will have small orders of magnitude, resulting in negative plastic displacements that forbid the execution of the analysis.

- Compressive behaviour

Regarding the compressive behaviour, the CDP assumes a linear stress-strain relation until the stress lands at the initial yield (σ_{c0}), followed by stress hardening (from σ_{c0} until the ultimate stress - σ_{cu}) and strain softening (from σ_{cu} onwards). Figure 52 displays the stress-strain (σ_c - ε_c^{in}) behaviour, and the terms present in the image are defined in the following expressions.

$$\varepsilon_{c0}^{e} = \frac{\sigma_c}{E_0}, \tag{35}$$

$$\varepsilon_{c,d}^{e} = \frac{\sigma_c}{[(1-d_c)E_0]}, \tag{36}$$

$$\tilde{\varepsilon}_c^{in} = \varepsilon_c - \varepsilon_{c0}^{e}, \tag{37}$$

$$\tilde{\varepsilon}_c^{p} = \varepsilon_c - \varepsilon_{c,d}^{e}, \tag{38}$$

where:

ε_{c0}^{e}: elastic strain (undamaged);

$\varepsilon_{c,d}^{e}$: elastic strain (damaged);

$\tilde{\varepsilon}_c^{in}$: inelastic (crushing) strain;

$\tilde{\varepsilon}_c^{p}$: equivalent plastic strain for crushed concrete.

From Equations 37 and 38, $\tilde{\varepsilon}_c^{p}$ can be written as:

$$\tilde{\varepsilon}_c^{p} = \tilde{\varepsilon}_c^{in} + \varepsilon_{c0}^{e} - \frac{\sigma_c}{(1-d_c)E_0} = \tilde{\varepsilon}_c^{in} - \frac{\sigma_c}{E_0}\left(\frac{1}{1-d_c} - 1\right) = \tilde{\varepsilon}_c^{in} - \frac{d_c}{1-d_c}\varepsilon_{c0}^{e}, \tag{39}$$

assuming that $\tilde{\varepsilon}_c^{p} = 0$ for $\sigma_c \leq \sigma_{cu}$

Regarding the compressive damage evolution, it is also directly determined by the compressive stress–strain relationship ($\boldsymbol{\sigma_c}$ - ε_c^{in}) , and $\boldsymbol{d_c}$ is calculated through:

$$d_c = 1 - (\frac{\sigma_c}{f_{cm}}). \tag{40}$$

Figure 52 – CDP compressive behaviour.

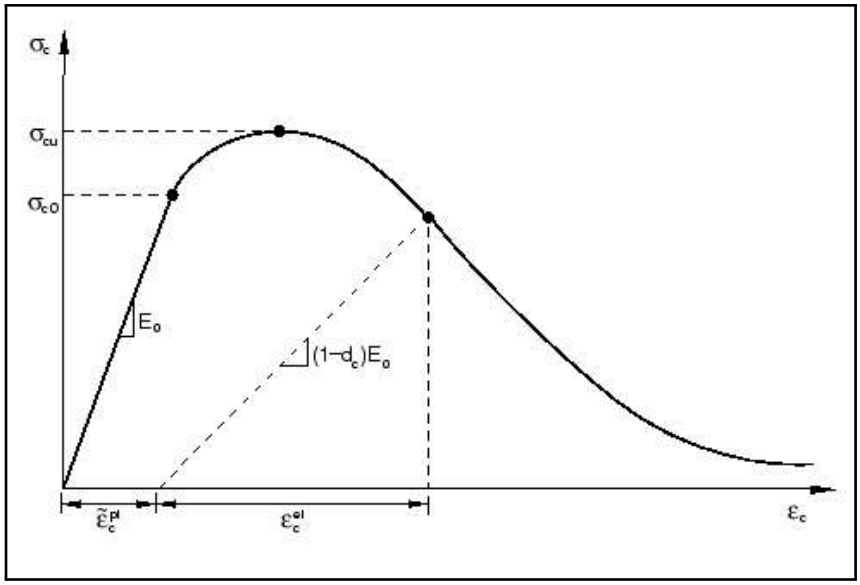

Source: Simulia (2017)

3.3.1.3 C30/37 concrete stress-strain relationships

Now that the CDP has been explained, the text will show how the uniaxial stress-strain curves and damage evolution for the C30/37 concrete were determined. These data must be input into Abaqus (the detailed procedure will be shown in section 4.1.1) to model the nonlinear material performance. The C30/37 concrete properties were taken from Eurocode 2 (BSI, 2004) and can be found in Table 10. Tensile behaviour will be described first, followed by the compressive.

Table 10 – Concrete properties from Eurocode 2.

C30/37		
f_{ck} (MPa)	Characteristic cylinder compressive strength	30
f_{cm} (MPa)	Mean cylinder compressive strength	38
f_{ctm} (MPa)	Mean tensile strength	2.9
E_c (MPa)	Young's modulus	32837

Source: BSI (2004)

- C30/37 tensile behaviour

The post-peak stress-strain relation was determined via the exponential law of Cornelissen et al. (1968) *APUD* (EARIJ et al., 2017) for tension softening:

$$\frac{\sigma_t}{f_t} = [1 + (c_1\frac{w_t}{w_{cr}})^3]\, exp(-c_2\frac{w_t}{w_{cr}}) - \frac{w_t}{w_{cr}}(1 + c_1^3)\, exp(-c_2), \text{ with } w_{cr} = 5.14\frac{G_F}{f_t}, \quad (41)$$

where:

$\boldsymbol{\sigma_t}$: tensile stress normal to crack direction;

$\boldsymbol{f_t}$: uniaxial tensile strength;

$\boldsymbol{w_{cr}}$: crack-opening displacement at complete release of stress;

$\boldsymbol{c_1}$: 3.00 (material constant);

$\boldsymbol{c_2}$: 6.93 (material constant);

$\boldsymbol{G_F}$: total fracture energy of concrete required to create a stress-free crack over a unit surface;

The stress-cracking strain relation ($\boldsymbol{\sigma_t}$ - $\boldsymbol{\varepsilon_t^{ck}}$) is achieved by considering the correspondence of the crack–opening displacement, $\boldsymbol{w_t}$, to the product between the characteristic length, $\boldsymbol{l_{ch}}$, and the cracking–strain, $\boldsymbol{\varepsilon_t^{ck}}$,

$$w_t = l_{ch}\, \varepsilon_t^{ck}. \quad (42)$$

According to Earij et al. (2017), Equation 42 is a localisation limiter since it connects the concrete constitutive relation with a mesh size property, therefore reducing the concrete fracture energy dependency on the element size. $\boldsymbol{l_{ch}}$ stems from the element geometry and formulation. For a 3D element, it is defined as the largest between its four main diagonals (SIMULIA, 2017). Determining a single value of $\boldsymbol{l_{ch}}$ for the entire mesh of different-sized concrete elements involves an averaging process. Therefore, this work obtained $\boldsymbol{l_{ch}}$ directly from *Abaqus* in a pre-analysis for accuracy and efficiency.

Figure 53 displays the stress-strain and damage parameter-strain curves obtained with Equation 41. $\boldsymbol{f_t}$ was taken as $\boldsymbol{f_{ctk,0.05} = 0.7 f_{ctm}}$ and $\boldsymbol{G_F}$ was estimated

through the CEB-FIP 1990 Model Code expression available at (EARIJ et al., 2017) that considers the base value of the fracture energy, G_{F0}, dependent on the maximum aggregate size: $G_F = G_{F0}(0.1 f_{cm})^{0.7}$. For that, the value of G_{F0} was assumed to be 0.026 N/mm (based on (EARIJ et al., 2017)).

Figure 53 – Concrete tensile behaviour.

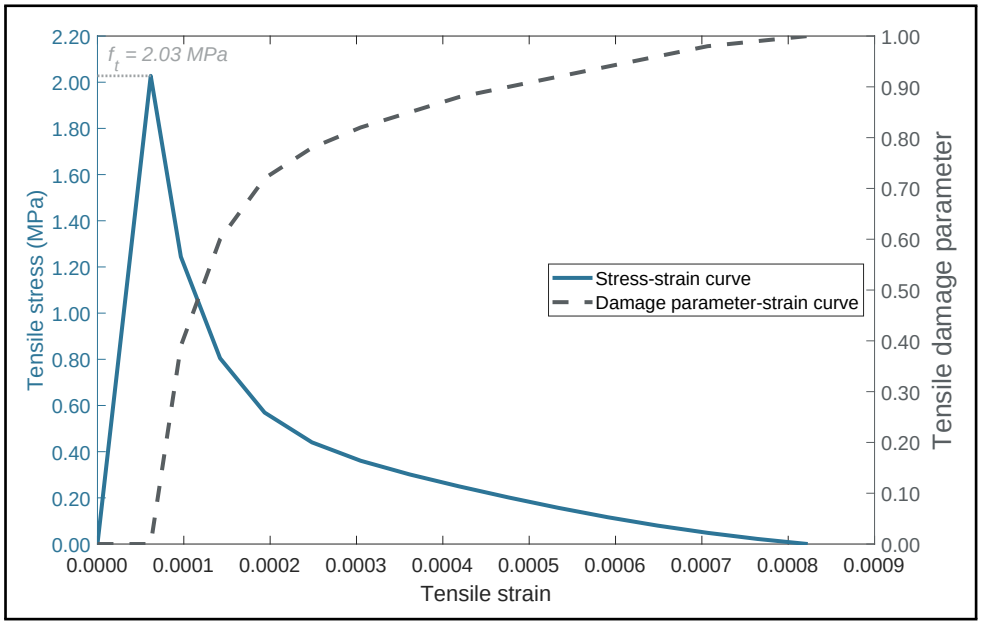

Source: The Author (2022)

- C30/37 compressive behaviour

The stress-strain relation from Eurocode 2 was the one used to determine the compressive behaviour:

$$\frac{\sigma_c}{f_{cm}} = \frac{k\eta - \eta^2}{1 + (k-2)\eta}, \tag{43}$$

with

$$\eta = \frac{\varepsilon_c}{\varepsilon_{c1}}, \quad k = 1.05 E_c \frac{\varepsilon_{c1}}{f_{cm}}, \quad \varepsilon_{c1} = 0.7 {f_{cm}}^{0.31},$$

and

σ_c: compressive stress;

ε_c: compressive strain;

ε_{c1}: compressive strain at peak stress;

Still following Eurocode 2, the ultimate strain, ε_{cu}, is taken as 0.0035 and the stress value for the proportionality limit as 40% of the f_{cm}.

Figure 54 displays the stress-strain and damage parameter-strain curves obtained with Equation 43.

Figure 54 – Concrete compressive behaviour.

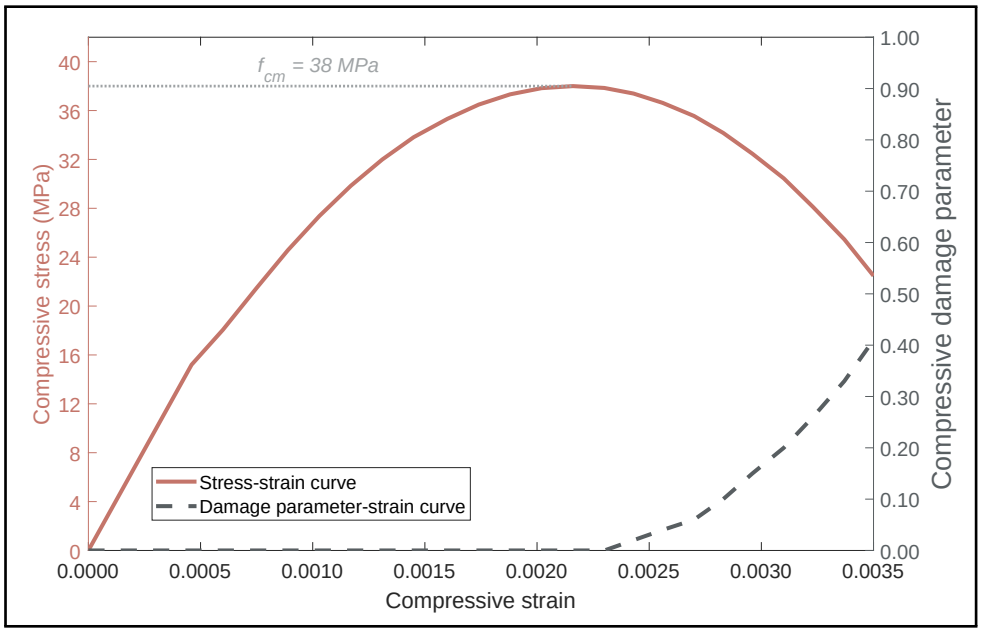

Source: The Author (2022)

Table 11 presents a summary of the parameters used to determine the tensile and compressive behaviours.

Table 11 – Physical and mechanical properties of the concrete.

	E_c (MPa)	ν (-)	f_{cm} (MPa)	f_t (MPa)	G_F (kN/m)	ρ (kg/m³)
C30/C37	32837	0.2	38	2.03	0.06619	2400

Source: The Author (2022)

3.3.2 Steel

In this research, the steel for the embedded ring was considered to perform linearly only. Since the main interest rested on the reinforced concrete's behaviour and the embedded ring's displacement, there was no need for this additional complexity in the analyses. Furthermore, it could incur stress concentrations and hinder the effectiveness of the models.

For the steel reinforcement bars, the work adopted an elastic perfectly-plastic behaviour. It was the same model applied by Chen, Xu e Li (2020), Chen et al. (2021)

when studying the wind turbine embedded-ring foundation and by Menin, Trautwein e Bittencourt (2009) when analysing numerical simulations of reinforced concrete structures with a smeared crack concrete model. Following Svensson (2010), a B500B steel was chosen for the reinforcement bars, while a Q345B steel was chosen for the ring based on recurrent literature properties.

The stress-strain relationship is exemplified by Figure 55, where it is possible to see how the material deforms proportionately to the stress ($E = E_s$) until reaching its yield stress (f_y). Then it enters the plastic phase and deforms under constant stress value. Finally, table 12 shows the necessary parameters to input the steel behaviour into Abaqus.

Figure 55 – Steel behaviour.

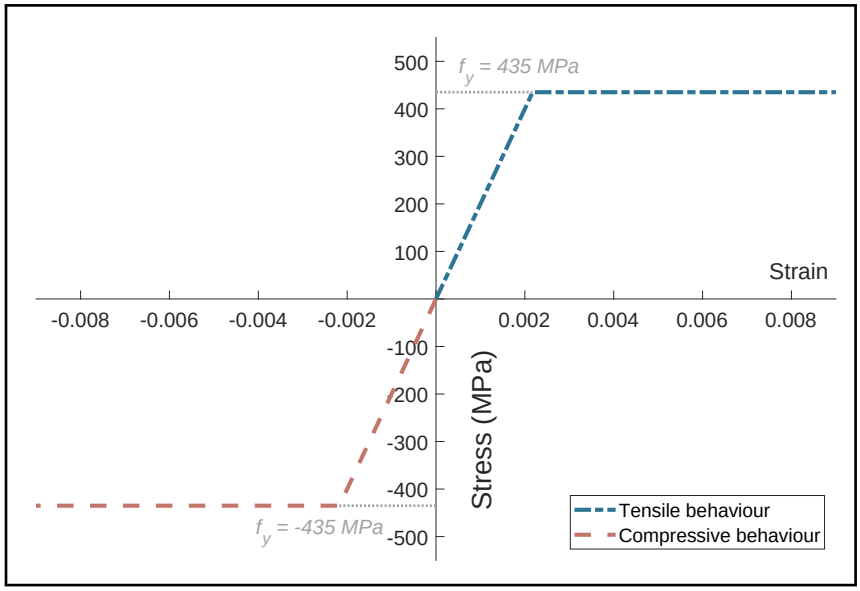

Source: The Author (2022)

Table 12 – Physical and mechanical properties of the steel.

	Structural Elements	E_s **(MPa)**	ν **(-)**	f_y **(MPa)**	ρ **(kg/m³)**
Q345B	Steel ring	206000	0.3	(-)	7850
B500B	Reinforcement bars	200000	0.3	435	7800

Source: The Author (2022)

3.4 FINITE ELEMENT METHOD

Modelling involves translating the behaviour of a real-life situation into a mathematical model. This action creates a representational tool with results that can be

analysed and interpreted. As Kreyszig (2011) puts it, this model is the formulation of a mathematical expression made out of variables, functions and equations that could reproduce the behaviour in question. Moreover, since many physical concepts are conveyed through derivatives, the models usually incur differential equations, which can be quite complex to solve.

An example is the behavioural distribution of stresses and displacements in a structure. Excluding simple structural systems, performing structural analysis using conventional analytical models is usually too intricate or unfeasible. An alternative is to approximate the solution using numerical models, of which the finite element method (FEM) is an example. By discretising the structural system into small units (the finite elements), the method approximates the system's analytical solution of differential equations to the combined solutions of more straightforward, algebraic ones about each unit.

Regarding the design of the numerical modelling, Soriano (2009) suggests a progressive approach: start attacking the problem with a simple model before implementing higher sophistication. The models in this work were produced following this line of thought, as portrayed by the schematic in Figure 56 (further details in Chapter 4).

Figure 56 – Progressive modelling approach.

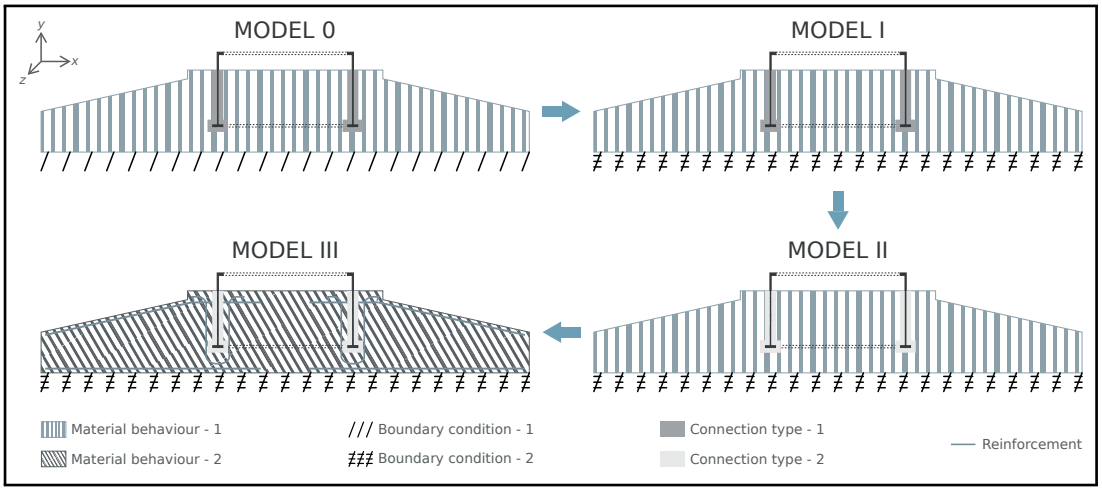

Source: The Author (2022)

The following topics will cover basic concepts of the FEM and particularities regarding its application in this work. Since the research was conducted in a finite element analysis software with element technologies already established, the mathematical formulation to follow is done in generic form to provide base knowledge regarding the project's scope.

3.4.1 Basic concepts

The FEM process is based on the substitution of the continuum of a structure by elements interconnected at points (nodes) via discretisation, as in Figure 57. These elements will be associated with a displacement function and a constitutive relation. Given the method's characteristic of interconnectivity, the behaviour of any element can be assuredly determined from all the others that comprise the structure through a set of simultaneous algebraic equations.

Figure 57 – Discretisation in FEM.

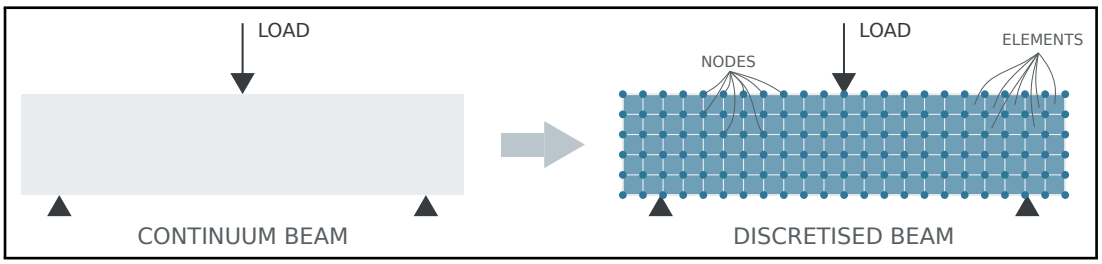

Source: The Author (2022)

The text now provides an overview of the problem structure based on the conceptualisation of the FEM by Zienkiewicz e Taylor (2005). The method is used to solve the problem of finding an unknown function, $\boldsymbol{u}$, which is the solution to a set of differential equations (Equation 44) in a particular domain ($\boldsymbol{\Omega}$) with specific boundary conditions (Equation 45) (boundary: $\boldsymbol{\Gamma}$).

$$A(u) = \left\{ \begin{array}{c} A_1(u) \\ A_2(u) \\ \dots \\ \dots \\ \dots \end{array} \right\} = 0 \tag{44}$$

$$B(u) = \left\{ \begin{array}{c} B_1(u) \\ B_2(u) \\ \dots \\ \dots \\ \dots \end{array} \right\} = 0 \tag{45}$$

Being a numerical method, it provides an approximate solution, $\widehat{\boldsymbol{u}}$:

$$u \approx \widehat{u} = \sum_{a=1}^{n} N_a \widetilde{u}_a = N\widetilde{u}, \tag{46}$$

where $\boldsymbol{N}$ are shape functions of independent variables usually defined locally for elements, and most of the $\widetilde{\boldsymbol{u}}_{\boldsymbol{a}}$ parameters are unknown. Those unknowns shall be obtained from an integral-form approximating equation, with known integrable functions $\boldsymbol{G_b}$ and $\boldsymbol{g_b}$, so that the approximation can be obtained element by element for posterior assemblage:

$$\int_{\Omega} G_b d\Omega + \int_{\Gamma} g_b d\Gamma = \sum_{e=1}^{m} \left(\int_{\Omega_e} G_b d\Omega + \int_{\Gamma_e} g_b d\Gamma \right) = 0, \text{ with } b = 1 \text{ to } n, \tag{47}$$

where $\boldsymbol{\Omega_e}$ is the domain of each element and $\boldsymbol{\Gamma_e}$ the part of the boundary of each element. Applying an approximation procedure to Equation 47 such as Galerkin, the system of approximating equations turns into a set of linear equations of the form:

$$\boldsymbol{K}\widetilde{\boldsymbol{u}} = \boldsymbol{f}, \tag{48}$$

with

$$K_{ab} = \sum_{e=1}^{m} K_{ab}^{e}, \quad f_a = \sum_{e=1}^{m} f_a^e.$$

Considering the structural system in Figure 58 and assuming a linear behaviour, Equation 48 takes the following form for element (1):

$$\boldsymbol{K^1 u^1} = \boldsymbol{f^1}. \tag{49}$$

$$f^1 = \left\{ \begin{array}{c} f_1^1 \\ f_2^1 \\ f_3^1 \end{array} \right\}$$

is the vector of nodal forces of element (1), induced by nodal displacements. f_1^1, f_2^1 and f_3^1 are the vectors of the force components in global coordinates for each node:

$$f_1^1 = \left\{ \begin{array}{c} f_{1x} \\ f_{1y} \end{array} \right\}; \quad f_2^1 = \left\{ \begin{array}{c} f_{2x} \\ f_{2y} \end{array} \right\}; \quad f_3^1 = \left\{ \begin{array}{c} f_{3x} \\ f_{3y} \end{array} \right\}$$

which show the number of degrees of freedom (DOFs) per node of the system is two. The same is valid for the vector of nodal displacements of the element:

$$u^1 = \left\{ \begin{array}{c} u_1^1 \\ u_2^1 \\ u_3^1 \end{array} \right\},$$

where

$$u_1^1 = \left\{ \begin{array}{c} u_1 \\ v_1 \end{array} \right\}; \quad u_2^1 = \left\{ \begin{array}{c} u_2 \\ v_2 \end{array} \right\}; \quad u_3^1 = \left\{ \begin{array}{c} u_3 \\ v_3 \end{array} \right\}.$$

Figure 58 – A typical structure built up from interconnected elements.

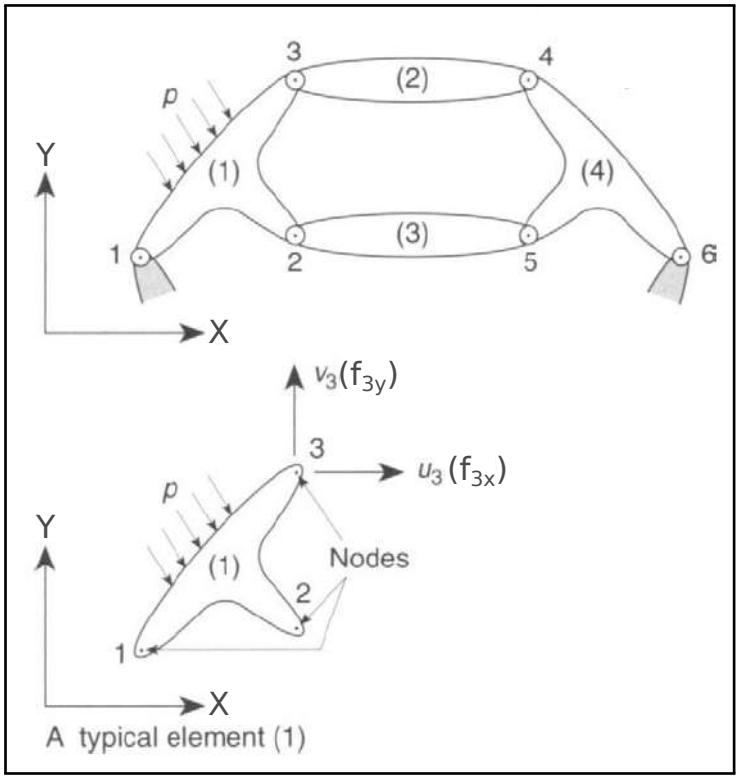

Source: Adapted from Zienkiewicz e Taylor (2005)

K^1 is referred to as the stiffness matrix of element (1). For a general element (e) with m nodes, the force and displacement vectors can be written, respectively, as:

$$f^e = \begin{Bmatrix} f_1^e \\ f_2^e \\ \dots \\ \dots \\ \dots \\ f_m^e \end{Bmatrix},$$

$$u^e = \begin{Bmatrix} u_1^e \\ u_2^e \\ \dots \\ \dots \\ \dots \\ u_m^e \end{Bmatrix},$$

and the element stiffness matrix as:

$$\boldsymbol{K^e} = \begin{bmatrix} K_{11}^e & K_{12}^e & \dots & K_{1m}^e \\ K_{21}^e & \dots & \dots & \dots \\ \dots & \dots & \dots & \dots \\ \dots & \dots & \dots & \dots \\ \dots & \dots & \dots & \dots \\ K_{m1}^e & \dots & \dots & K_{mm}^e \end{bmatrix}$$

where each f_a^e and u_a^e possesses the same number of DOFs and each K_{ab}^e are square submatrices of size DOFs x DOFs.

After having visualised the general concept and procedure of the FEM, let us now comment on specific steps and particularities of the elements present in the analyses.

- Type and size of elements

Defining the element type and size is a subject dependent on an engineering assessment of the structure (LOGAN, 2016). Regarding the type, elements will mainly differ in their geometry and order of interpolation function. Some basic first-order element shapes are shown in Figure 59, ranging from one- to three-dimension forms. Figure 60,

on the other hand, presents some of these shapes as second-order elements regarding their interpolation function. These have mid-side nodes, useful for curved geometries.

Figure 59 – Element shapes.

(a) One dimensional element. (b) Two-dimensional elements. (c) Three-dimensional elements.

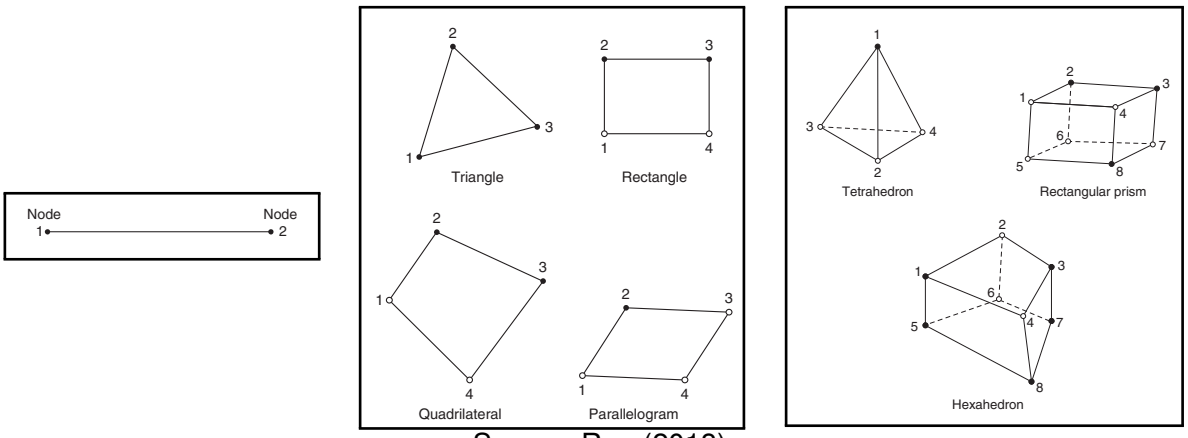

Source: Rao (2018)

Figure 60 – Second-order elements.

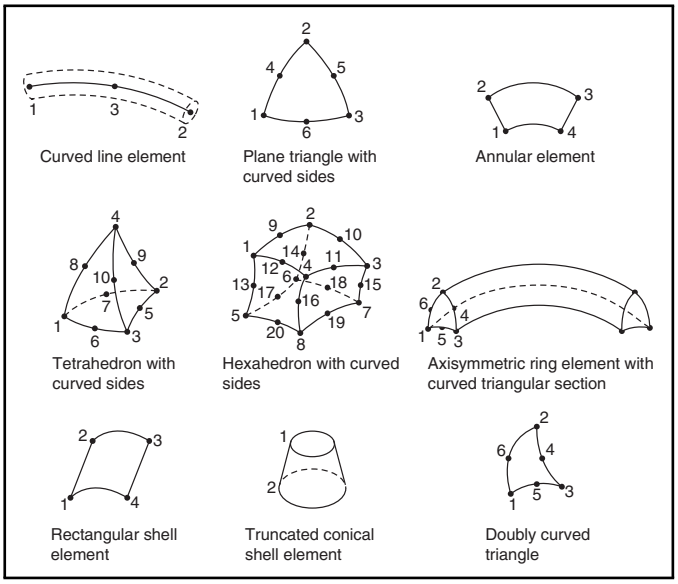

Source: Rao (2018)

The choice of element for a wind turbine foundation will depend on the engineering assumptions adopted for the analysis. For example, linear analysis of 2D plate elements is the industrial practice in the Netherlands for the steel reinforcement design process, according to Moraal (2019).

However, the foundation is a structure submitted to considerable loads with a high central section (the pedestal), therefore characterised as too complex to have its stress distributions over the height simplified to the level of horizontal plane geometry.

Moreover, the foundation interaction with the embedded ring would be compromised. That is why a 3D analysis was deemed fitter for this research.

A hexahedron element, a three-dimensional element with eight corner nodes, commonly known as “brick”, is the base element for the concrete and the steel ring. Each node can displace spatially, and Figure 61a presents the brick element arbitrarily oriented regarding the global axes *X*, *Y* and *Z*, where *rst* represents the local system of coordinates.

On the other hand, the reinforcement bars were modelled with space truss elements, one-dimensional bars that can only resist axial forces and deform in the axial direction. This characteristic makes it the ideal element for the research’s assumption of perfect bond between the bars and the concrete. Figure 61b presents the bar element arbitrarily oriented regarding the global axes *X*, *Y* and *Z*. The local axis, *x*, is aligned with the axial direction of the bar, u_1 and u_2 are the nodal axial displacements, and ℓ is the length of the element.

Figure 61 – Elements used in the analyses.

(a) Brick element. (b) Space truss element.

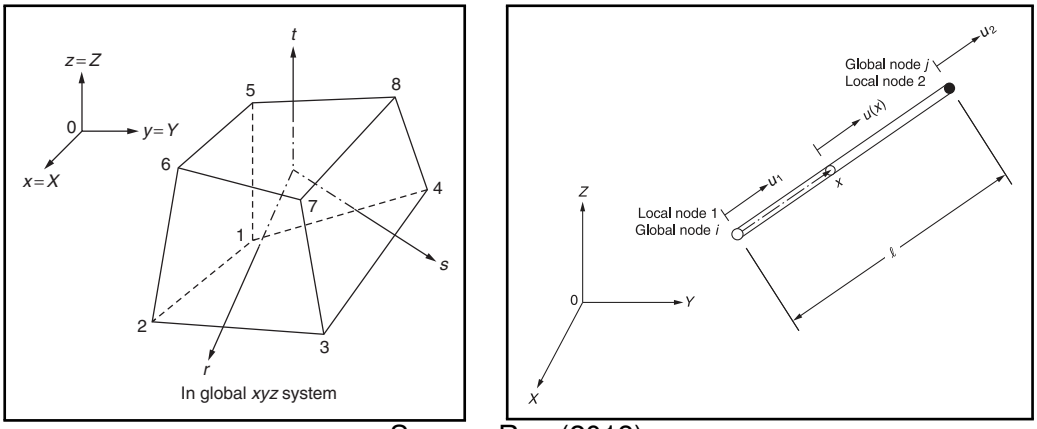

Source: Rao (2018)

When it comes to size, the choice will directly affect the convergence of the solution: smaller elements are associated with a more accurate response but also incur longer computation time (RAO, 2018). That is why some situations might require different element sizes for different parts of a structure. For example, Figure 62 depicts the use of this strategy with smaller-sized elements confined to the boundaries of the hole, a region where stress concentrations occur.

Figure 62 – Meshing strategy for stress concentration.

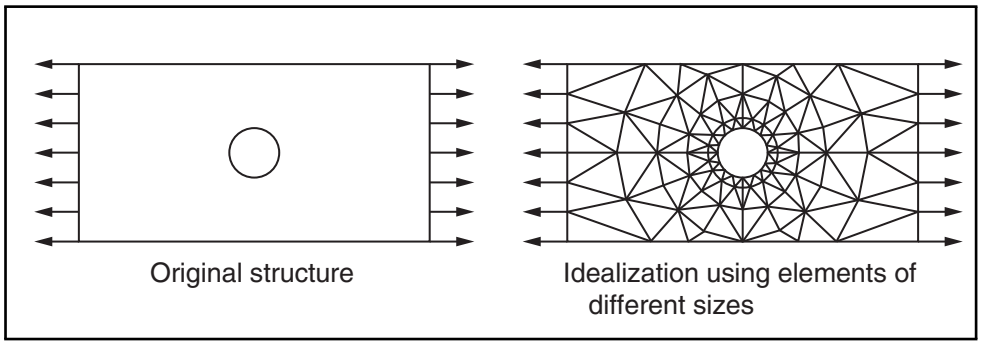

Source: Rao (2018)

- Displacement function

The approximate solution is the displacement function that must be defined to approximate the deformed shape of the element ($\widehat{u}$). It can be a polynomial written around the element's nodal displacements, its order depending on the DOFs.

The brick element is usually taken as isoparametric, which makes the displacement function derivation easier (RAO, 2018) and the element a unit cube in local coordinates (Figure 63). This strategy requires first an association between the local and global coordinates, achieved through the following process:

Figure 63 – Hexahedron element in the natural coordinate system (isoparametric).

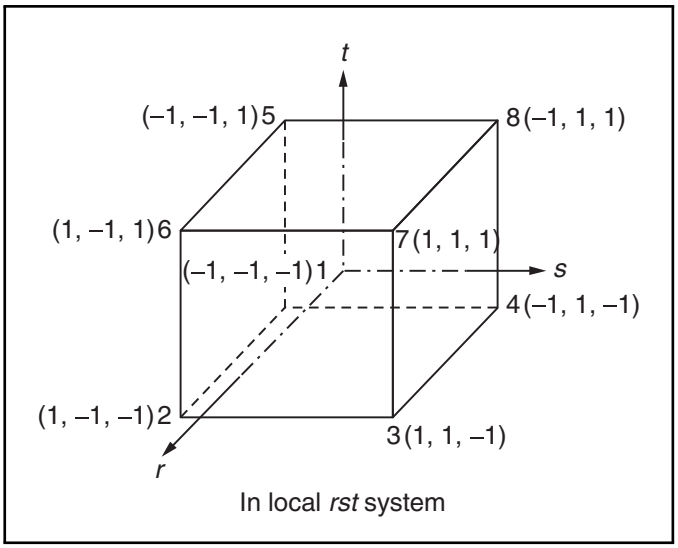

Source: Rao (2018)

$$\left\{ \begin{array}{c} x \\ y \\ z \end{array} \right\} = \left\{ \begin{array}{c} \sum_{i=1}^{8} N_i x_i \\ \sum_{i=1}^{8} N_i y_i \\ \sum_{i=1}^{8} N_i z_i \end{array} \right\}, \tag{50}$$

where

$$N_i(r,s,t) = \frac{1}{8}(1 + r \cdot r_i)(1 + s \cdot s_i)(1 + t \cdot t_i), \text{ with } i = 1 \text{ to } 8$$

Equation 50 can also be written as:

$$\left\{ \begin{array}{c} x \\ y \\ z \end{array} \right\} = \boldsymbol{N} \left\{ \begin{array}{c} x_1 \\ y_1 \\ z_1 \\ ... \\ ... \\ ... \\ x_8 \\ y_8 \\ z_8 \end{array} \right\}, \tag{51}$$

with

$$\boldsymbol{N} = \left[\begin{array}{ccccccccccc} N_1 & 0 & 0 & N_2 & 0 & 0 & & N_8 & 0 & 0 \\ 0 & N_1 & 0 & 0 & N_2 & 0 & ... & 0 & N_8 & 0 \\ 0 & 0 & N_1 & 0 & 0 & N_2 & & 0 & 0 & N_8 \end{array} \right]$$

The linear displacement function can use the same shape functions to characterise the hexahedron geometry, and so the brick element displacement equation becomes:

$$\widehat{\boldsymbol{u}} = \boldsymbol{N}\ \boldsymbol{u}, \tag{52}$$

where:

$$\boldsymbol{u} = \left\{ \begin{array}{c} \boldsymbol{u_1} \\ \boldsymbol{u_2} \\ \boldsymbol{u_3} \\ \boldsymbol{u_4} \\ \boldsymbol{u_5} \\ \boldsymbol{u_6} \\ \boldsymbol{u_7} \\ \boldsymbol{u_8} \end{array} \right\},$$

and

$$\boldsymbol{u_1} = \left\{ \begin{array}{c} u_1 \\ v_1 \\ w_1 \end{array} \right\};\ \boldsymbol{u_2} = \left\{ \begin{array}{c} u_2 \\ v_2 \\ w_2 \end{array} \right\};\ ...\ ;\ \boldsymbol{u_8} = \left\{ \begin{array}{c} u_8 \\ v_8 \\ w_8 \end{array} \right\}.$$

As for the space truss elements, the shape functions for Equation 52, to form the linear displacement function, are:

$$\boldsymbol{N} = \left[\begin{array}{cc} (1 - \frac{x}{l}) & \frac{x}{l} \end{array} \right] \tag{53}$$

and:

$$\boldsymbol{u} = \left\{ \begin{array}{c} \boldsymbol{u_1} \\ \boldsymbol{u_2} \end{array} \right\},$$

with

$$\boldsymbol{u_1} = \left\{ \begin{array}{c} u_1 \\ v_1 \\ w_1 \end{array} \right\} \text{ and } \boldsymbol{u_2} = \left\{ \begin{array}{c} u_2 \\ v_2 \\ w_2 \end{array} \right\}.$$

- Stress-strain and strain-displacement relations

Constitutive information is included in the mathematical model through the associations of stress-strain and strain-displacement relations. For this, we must first consider Hooke's law for linear-elastic behaviour:

$$\boldsymbol{\sigma} = \boldsymbol{D}\ \boldsymbol{\varepsilon}, \tag{54}$$

where $\boldsymbol{\sigma}$ is the stress vector, ε is the strain vector, and $\boldsymbol{D}$ is the elasticity matrix of the material. Considering a material whose deformations are spatially analysed, Equation 54 can be extended as:

$$\begin{pmatrix} \sigma_x \\ \sigma_y \\ \sigma_z \\ \tau_{xy} \\ \tau_{yz} \\ \tau_{zx} \end{pmatrix} = \frac{E}{(1-2\nu)(1+\nu)} \begin{bmatrix} 1-\nu & -\nu & -\nu & 0 & 0 & 0 \\ -\nu & 1-\nu & -\nu & 0 & 0 & 0 \\ -\nu & -\nu & 1-\nu & 0 & 0 & 0 \\ 0 & 0 & 0 & \frac{1-2\nu}{2} & 0 & 0 \\ 0 & 0 & 0 & 0 & \frac{1-2\nu}{2} & 0 \\ 0 & 0 & 0 & 0 & 0 & \frac{1-2\nu}{2} \end{bmatrix} \begin{pmatrix} \epsilon_x \\ \epsilon_y \\ \epsilon_z \\ \gamma_{xy} \\ \gamma_{yz} \\ \gamma_{zx} \end{pmatrix} \tag{55}$$

The kinetic expressions, which relate strains to displacements in the material:

$$\begin{aligned} \epsilon_x &= \frac{\partial u}{\partial x} \qquad & \gamma_{xy} &= \frac{\partial u}{\partial y} + \frac{\partial v}{\partial x} \\ \epsilon_y &= \frac{\partial v}{\partial y} \qquad & \gamma_{yz} &= \frac{\partial v}{\partial z} + \frac{\partial w}{\partial y} \\ \epsilon_z &= \frac{\partial w}{\partial z} \qquad & \gamma_{zx} &= \frac{\partial w}{\partial x} + \frac{\partial u}{\partial z} \end{aligned} \tag{56}$$

can also be written in matrix notation:

$$\begin{pmatrix} \epsilon_x \\ \epsilon_y \\ \epsilon_z \\ \gamma_{xy} \\ \gamma_{yz} \\ \gamma_{zx} \end{pmatrix} = \begin{bmatrix} \frac{\partial}{\partial x} & 0 & 0 \\ 0 & \frac{\partial}{\partial y} & 0 \\ 0 & 0 & \frac{\partial}{\partial z} \\ \frac{\partial}{\partial y} & \frac{\partial}{\partial x} & 0 \\ 0 & \frac{\partial}{\partial z} & \frac{\partial}{\partial y} \\ \frac{\partial}{\partial z} & 0 & \frac{\partial}{\partial x} \end{bmatrix} \begin{pmatrix} \widehat{u} \\ \widehat{v} \\ \widehat{w} \end{pmatrix}. \tag{57}$$

If we consider that

$$\boldsymbol{B_i} = \begin{bmatrix} \frac{\partial}{\partial x} & 0 & 0 \\ 0 & \frac{\partial}{\partial y} & 0 \\ 0 & 0 & \frac{\partial}{\partial z} \\ \frac{\partial}{\partial y} & \frac{\partial}{\partial x} & 0 \\ 0 & \frac{\partial}{\partial z} & \frac{\partial}{\partial y} \\ \frac{\partial}{\partial z} & 0 & \frac{\partial}{\partial x} \end{bmatrix}, \tag{58}$$

and that

$$\boldsymbol{B} = [[\boldsymbol{B_1}]\ [\boldsymbol{B_2}]\ ...\ [\boldsymbol{B_8}]], \tag{59}$$

then we get the kinetic relation for a brick element:

$$\boldsymbol{\varepsilon} = \boldsymbol{B}\ \widehat{\boldsymbol{u}}. \tag{60}$$

**The process of obtaining the $\boldsymbol{B_i}$ matrices involves evaluating derivatives of composite functions since $N_i = N_i(r, s, t)$. The detailed procedure can be found in (RAO, 2018).*

The process for the space truss element is more straightforward than for the 3D, since stress and strain only occur in the axial direction of the element. With $\boldsymbol{D}$ = E and the linear shape functions in Equation 53, the derivative operator for the truss element is constant valued:

$$\boldsymbol{B} = \begin{bmatrix} (-\frac{1}{l}) & \frac{1}{l} \end{bmatrix}. \tag{61}$$

Finally, Equation 62 below is the general form for obtaining the stiffness matrix of the element, $\boldsymbol{K^e}$:

$$\boldsymbol{K^e} = \int_{\Omega} \boldsymbol{B}^T \boldsymbol{D} \boldsymbol{B}\ d\Omega. \tag{62}$$

Presuming it is in the global coordinates of the system, each $\boldsymbol{K^e}$ will assume its position in the global stiffness matrix, $\boldsymbol{K}$, following the example schematic drawn by Zienkiewicz e Taylor (2005) in Figure 64. Then, the solution of the initial problem comes down to solving the resulting system of nodal equilibrium equations of the structure.

Figure 64 – General pattern of $\boldsymbol{K}$ assemblage.

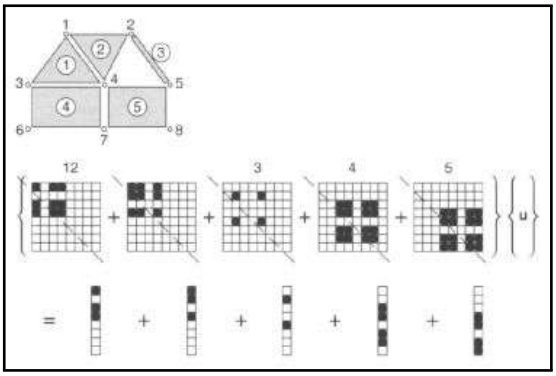

Source: Zienkiewicz e Taylor (2005)

3.4.2 Concrete nonlinearity and steel reinforcement

This topic will discuss how implementing the more advanced features of nonlinear concrete behaviour and steel reinforcement bars affect the finite element rationale presented. The material models for concrete and steel were developed separately in Section 3.3 so that the reinforced concrete structure can be represented with independent elements for each material.

The reader will remember that the assumed nonlinear behaviour for the concrete, the CDP, has different scenarios for tensile and compressive situations and uses both plasticity and damage fundamentals to shape the mechanics of concrete degradation. The smeared crack model was adopted regarding the damage mechanics and cracks' reproduction.

Phillips e Zienkiewicz (1976) presented a smeared crack approach to perform nonlinear finite element analyses in reinforced concrete structures. Reaffirming that the most significant aspect of the concrete nonlinear behaviour is tensile cracking, the authors introduced finite element equations in association with numerical tools for nonlinear analysis. They did so with isoparametric elements under plane and axisymmetric conditions but highlighted the research's applicability for three dimensions. Again, the text will not dive deep into the formulations, given the use of third-party software, but will provide the necessary knowledge for a good understanding of the analyses.

Regarding the steel reinforcement bars, whose elastic perfectly-plastic behaviour was defined in Section 3.3.2, there are three strategies to model them into reinforced concrete (KWAK; FILIPPOU, 1990). First, through a distributed model, which requires a composite concrete-steel constitutive relation and assumes the reinforcement as smeared over the concrete element. Then, the discrete model, where one-dimensional elements with two or three DOFs in each node are superimposed on the concrete mesh. Finally, the embedded model, adopted in the research, where one-dimensional bar elements of axial-only displacements are built into the concrete element and present a perfect bond with the concrete. The bar's displacements can then be obtained from the host element's displacement field (PHILLIPS; ZIENKIEWICZ, 1976).

In a reinforced concrete structure modelled with embedded bars, the resulting element stiffness matrix assembles the concrete and steel elements' stiffness matrices. Given the perfectly elasto-plastic behaviour of the steel and the uniaxial behaviour of the bar element, $\boldsymbol{K}^e$ for the steel bars is the same as a stiffness matrix for linear-elastic

space truss elements,

$$\boldsymbol{K}^{e} = \frac{AE}{l}\begin{bmatrix} 1 & -1 \\ -1 & 1 \end{bmatrix}, \tag{63}$$

with $\boldsymbol{K}^{e}$ in local coordinates and $\boldsymbol{A}$ the cross-sectional area of the bar, with the exception that E will change if the bar yields: $E = E_s$ before yielding; and $E = 0$ after yielding.

The concrete element stiffness matrix, on the other hand, deserves more attention. As discussed in Section 3.3.1.1, the crack formation in the adopted model is registered through changes to the constitutive relation that represent the material, not to the mesh topology. Also, let us consider how constitutive laws ($f(\sigma, \varepsilon) = 0$) effectively connect kinematic to kinetic variables that, for elastic materials, define behaviour that depends on the current deformation state (REDDY, 2015). Therefore, if the law in question allows an evaluation of stress for a given strain, we can write (PHILLIPS; ZIENKIEWICZ, 1976):

$$d\boldsymbol{\sigma} = \boldsymbol{D_t}(\boldsymbol{u})d\boldsymbol{\varepsilon}. \tag{64}$$

where $\boldsymbol{D_t}$ is the tangent (instantaneous) elasticity matrix. The nonlinear constitutive behaviour is reflected in the elasticity's dependence on the displacement value: the physical parameter is no longer constant as it was in Section 3.4.1, Equations 54 and 55. It results in the following expression for obtaining the element's stiffness matrix:

$$\boldsymbol{K}^{e}(\boldsymbol{u}) = \int_{V} \boldsymbol{B}^{T}\boldsymbol{D_t}(\boldsymbol{u})\boldsymbol{B}\; dV. \tag{65}$$

and in nonlinear algebraic equations for the elements:

$$\boldsymbol{K}^{e}(\boldsymbol{u}^{e})\,\boldsymbol{u}^{e} = \boldsymbol{f}^{e}. \tag{66}$$

If $\boldsymbol{K}^{e}$ is a function of the unknown variable, $\boldsymbol{u}^{e}$, it cannot be evaluated directly, nor can the system be solved. A viable strategy is calculating $\boldsymbol{K}^{e}(\boldsymbol{u}^{e(1)})$, where $\boldsymbol{u}^{e(1)}$ is an initially prescribed approximate solution. These element matrices can then be assembled to form a global stiffness matrix, $\boldsymbol{K}$, evaluated with the global vector of prescribed solutions, $\boldsymbol{u}^{(1)}$. The result is the transformation of the system of nonlinear equations (Equation 66) to a linear system:

$$\boldsymbol{K}(\boldsymbol{u}^{(1)})\,\boldsymbol{u}^{(2)} = \boldsymbol{F}, \tag{67}$$

where now $\boldsymbol{u}^{(2)}$ is the unknown approximate solution. This process is executed iteratively until its level of precision is deemed adequate. There are several numerical iterative procedures in the literature. Since *Abaqus* applies the Newton-Raphson method through the analyses presented in this work, it is the one to be briefly described next.

3.4.2.1 Newton-Raphson

It has already been established that one way to solve nonlinear systems is to iteratively find solutions to approximated linear equations until the constitutive, compatibility and equilibrium conditions are respected within a pre-determined error. Within this context, Newton-Raphson's method applies the concept of residual forces to linearise the nonlinear equations. Consider the following Equations:

$$\boldsymbol{K}(\boldsymbol{u})\,\boldsymbol{u} = \boldsymbol{F}, \tag{68}$$

$$\boldsymbol{R}(\boldsymbol{u}) = 0, \tag{69}$$

$$\boldsymbol{R}(\boldsymbol{u}) = \boldsymbol{K}(\boldsymbol{u})\,\boldsymbol{u} - \boldsymbol{F}, \tag{70}$$

where $\boldsymbol{R}(\boldsymbol{u})$ is the residual force. The idea is to compare the equivalent nodal forces, $\boldsymbol{K}(\boldsymbol{u})\boldsymbol{u}$, to the applied loads, $\boldsymbol{F}$, and measure the lack of equilibrium.

Plotting the equilibrium path ($R(u, F) = 0$) for one iteration (Figure 65) allows the graphic indication of the following terms:

$$\boldsymbol{K_t} = \left.\frac{\partial \boldsymbol{R}}{\partial \boldsymbol{u}}\right|_{\boldsymbol{u}^{(1)}} \rightarrow \text{tangent stiffness}, \tag{71}$$

$$\boldsymbol{K}(\boldsymbol{u}^{(1)}) \rightarrow \text{secant stiffness}. \tag{72}$$

Now consider that $\boldsymbol{u}^{(r-1)}$ is an approximate, known solution in iteration $(r-1)$, and the goal is to encounter the next solution: $\boldsymbol{u}^{(r)}$. The process starts with an expansion

Figure 65 – Load-displacement curve.

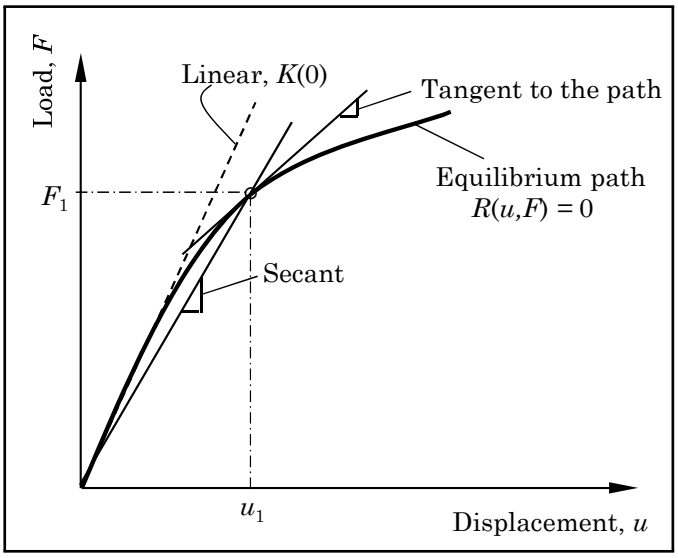

Source: Reddy (2015)

of $\boldsymbol{R}(\boldsymbol{u})$ in Taylor's series around $\boldsymbol{u}^{(r-1)}$:

$$\boldsymbol{R}(\boldsymbol{u}) = \boldsymbol{R}(\boldsymbol{u}^{(r-1)}) + \left.\frac{\partial \boldsymbol{R}}{\partial \boldsymbol{u}}\right|_{\boldsymbol{u}^{(r-1)}} \boldsymbol{\delta u} + \frac{1}{2}\left.\frac{\partial^2 \boldsymbol{R}}{\partial \boldsymbol{u^2}}\right|_{\boldsymbol{u}^{(r-1)}} (\boldsymbol{\delta u})^2 + ... = 0, \tag{73}$$

with

$$\boldsymbol{\delta u}^{(r)} = \boldsymbol{u}^{(r)} - \boldsymbol{u}^{(r-1)} \tag{74}$$

the increment. If terms of $\boldsymbol{\delta u}$ higher than first-order are considered negligible, and the tangent definition from Equation 71 is used, Equation 73 becomes:

$$\boldsymbol{R}(\boldsymbol{u}) = \boldsymbol{R}(\boldsymbol{u}^{(r-1)}) + \boldsymbol{K_t}(\boldsymbol{u}^{(r-1)})\boldsymbol{\delta u}^{(r)} = 0. \tag{75}$$

Therefore,

$$\boldsymbol{\delta u}^{(r)} = -(\boldsymbol{K_t}(\boldsymbol{u}^{(r-1)}))^{-1}\boldsymbol{R}(\boldsymbol{u}^{(r-1)}), \tag{76}$$

where, in the case of convergence, the residual force reduces toward zero with each iteration. If Equation 70 is applied to Equation 76, the increment can then be calculated in terms of $\boldsymbol{K_t}$, $\boldsymbol{K}$ and $\boldsymbol{F}$:

$$\boldsymbol{\delta u}^{(r)} = (\boldsymbol{K_t}(\boldsymbol{u}^{(r-1)}))^{-1}(\boldsymbol{F} - \boldsymbol{K}(\boldsymbol{u}^{(r-1)})\boldsymbol{u}^{(r-1)}). \tag{77}$$

After determining the increment for the ongoing iteration, $\boldsymbol{\delta u}^{(r)}$, it rests only to add it to the solution from the previous iteration to get the current one (Equation 78). A convergence criterion must be defined to determine when the iteration stops, such as the maximum allowed difference between two consecutive values of $\boldsymbol{u}$ (alias, the maximum increment size).

$$\boldsymbol{u}^{(r)} = \boldsymbol{u}^{(r-1)} - \boldsymbol{\delta u}^{(r)} \tag{78}$$

A particular aspect of the Newton-Raphson method is that the tangent matrix is only updated after some iterations have occurred and altered the residual force. Therefore, it is a more cost-effective procedure than the Newton method, which promotes the matrix update at every iteration (REDDY, 2015).

Finally, Figure 66 presents a load-displacement plot for a solution obtained with the method, highlighting iterative steps and terms of interest discussed above.

Figure 66 – Load-displacement curve – Newton-Raphson.

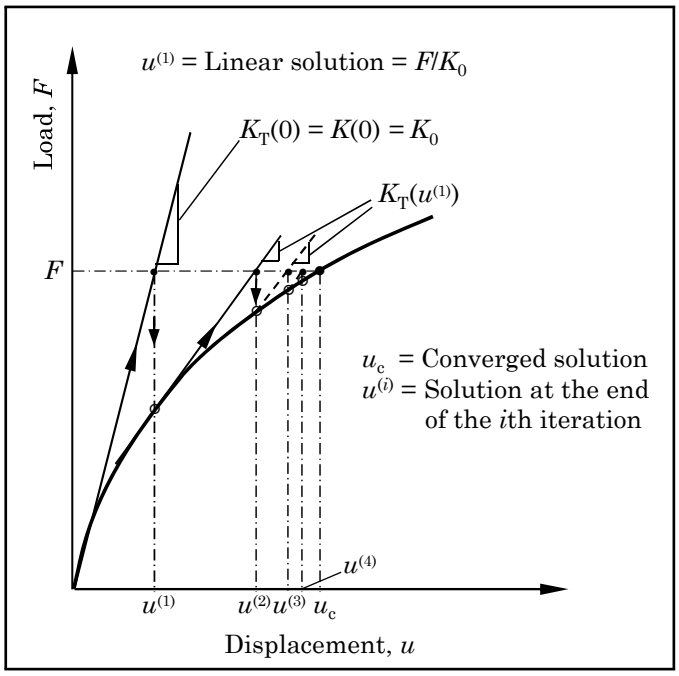

Source: Reddy (2015)

Hence, when the Newton-Raphson method is used, solving the nonlinear problem constitutes iteratively solving a system of linear equations. Thus, after the onset of cracks, the only change to the stiffness matrix of the concrete is the definition of orthotropic material to substitute the isotropic relations of the uncracked concrete, accomplished through modifications of $\boldsymbol{D_t}$ (PHILLIPS; ZIENKIEWICZ, 1976). Altogether, $\boldsymbol{D_t}$ is essen-

tially an instantaneous elasticity matrix that captures abrupt changes between elastic states, and the nonlinear analysis is solved by transitioning successively from one state to the other.

4 NUMERICAL MODELS AND RESULTS

Before presenting the data for each specific model, features common to developing all of them and critical data analyses will be presented in the following section, Section 4.1. Afterwards, the text will present a summary description of each model, followed by their results. Section 4.6 concludes by analysing and discussing those results.

All the models were built and analysed with the third-party finite element software *Abaqus*, version 2017, on the same computer with an Intel(R) Core(TM) i7-6500U CPU @ 2.50GHz 2.59 GHz processor and 12GB of installed RAM. Additionally, all contour and symbol graphs were exported from *Abaqus* with a deformation scale factor of 50.

**The colour spectra used for the contour graphs were the Berlin and Lajolla colourmaps from the 'Scientific color maps' (CRAMERI, 2018), a "Suite of scientific, colour-vision deficiency friendly and perceptually uniform colour maps that prevent both excluding readers and significant visual errors, which would otherwise visually distort the underlying data and mislead the reader".*

4.1 NUMERICAL MODELLING ASPECTS

This section will present a detailed description of the models' development and a mesh convergence analysis.

4.1.1 Methodology

As previously mentioned, the research's methodology followed a line of model development with a progressive increase in complexity. The diagram below (Figure 67) illustrates the project development path and introduces the research's four models:

The actual modelling activity performed in *Abaqus* will be divided here into seven stages for didactic purposes. Those stages are ordered in the flowchart in Figure 68 that precedes the descriptive explanation of how each was executed. The colour-coded legend in the Figure is used in the flowchart to point out stages that changed for the model in question compared to Model I. The same colour code will be used inside each stage description to signal to the reader where the feature was implemented.

Figure 67 – Progressive methodology.

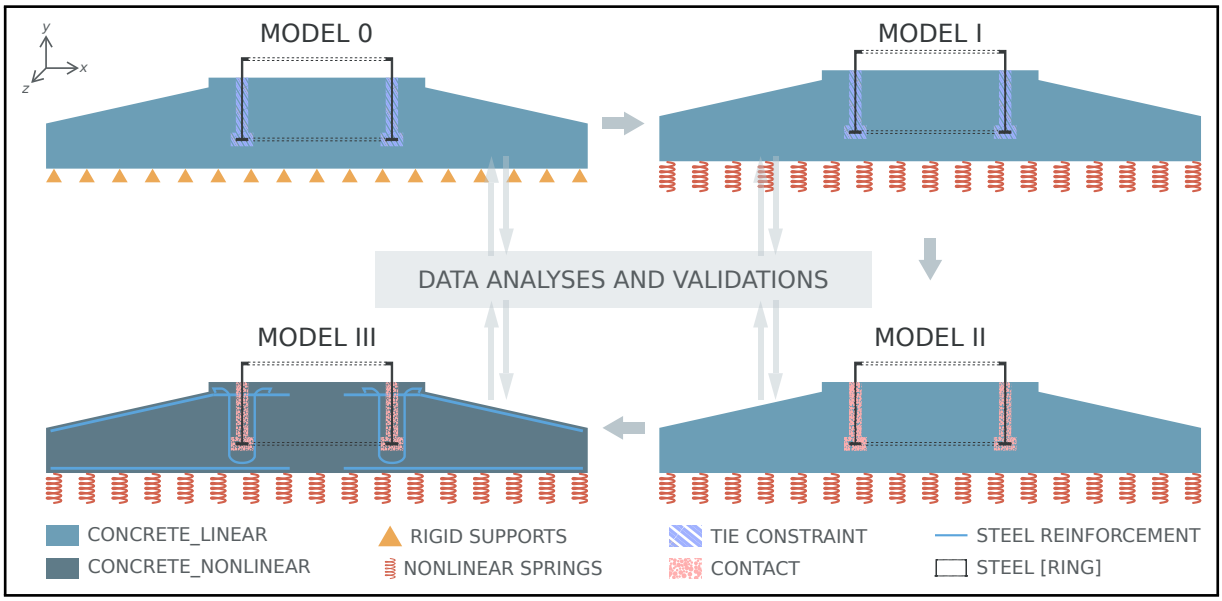

Source: The Author (2022)

Figure 68 – The modelling stages.

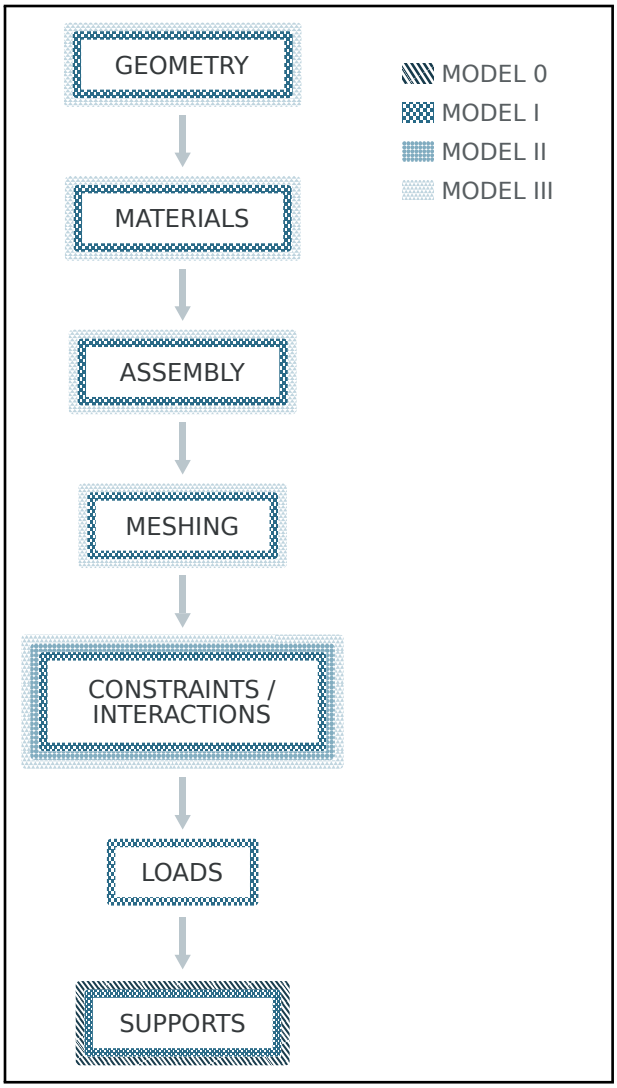

Source: The Author (2022)

Regarding the iteration method and convergence conditions of the analyses, Model III, which presented the nonlinearity condition of the material, was the only one that required incrementation. The *static, general* step was used for a force control method, with automatic incrementation type for a maximum number of 10000 increments, with an initial increment size of 0.01 limited from 1E-8 to 0.1. The equation solver used the direct method with unsymmetric matrix storage.

- Geometry

Firstly, each element that composes the structural foundation had to be created by drawing the geometries for the concrete base, the embedded ring, and the steel reinforcement bars. Figure 69 displays the resulting *parts* (nomenclature employed by *Abaqus*).

Figure 69 – 3D geometries - *parts*.

(a) Concrete base.

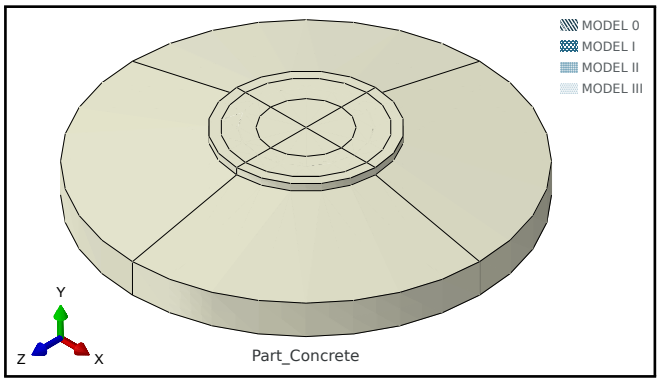

(b) Embedded ring.

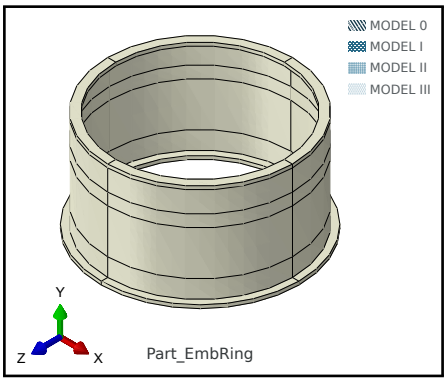

(c) Reinforcement bars.

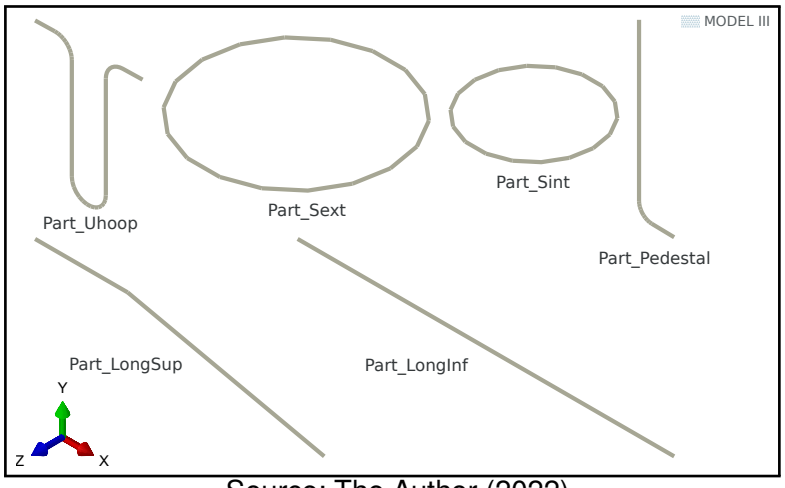

Source: The Author (2022)

- Materials

Throughout the research, four material models had to be defined in *Abaqus* for the simulations, their behaviours and properties having been derived in Section 3.3.

- *MatConc_lin*: linear-elastic concrete, for the foundation;
- *MatSteel_lin*: linear-elastic steel, for the embedded ring;
- *MatConc_CDP*: damaged-plasticity concrete, for the foundation submitted to nonlinear analysis;
- *MatSteel_epp*: elastic perfectly-plastic, for the steel reinforcement bars.

For all the cited materials, *Abaqus* requires the input of E and ν, displayed in Table 13. For the linear-elastic materials, these are the only data necessary. For *MatConc_CDP*, in addition to the elastic properties, *Abaqus* requires data on plasticity parameters, compressive and tensile behaviours, and damage evolution.

Table 13 – Elastic properties.

Material model	**Strength grade**	E **(MPa)**	ν **(-)**	**Model presence**
MatConc_lin	C30/37	32837	0.2	0, I, II
MatSteel_lin	Q345B	206000	0.3	0, I, II, III
MatConc_CDP	C30/37	32837	0.2	III
MatSteel_epp	B500B	200000	0.3	III

Source: The Author (2022)

The use of the plasticity parameters in Table 14 is detailed in Section 3.3.1. ψ took the value of 40° from (EARIJ et al., 2017), and the values adopted for ϵ, K and σ_{b0}/σ_{c0} were *Abaqus*'s default values, a common practice in the literature. However, the default value for the viscosity parameter (μ) is 0 to characterise an inviscid system. A different value implies that *viscoplastic regularisation* will be used. That is a relaxation technique available in *Abaqus* to conquer severe convergence difficulties that arise from analysing materials with softening behaviour and stiffness degradation (the scenario of Model III, which could not be analysed without the technique). In practical terms, the viscoplastic regularisation allows the stress values to be outside the yield surface, so the tangent stiffness of the softening material becomes positive for sufficiently small time increments. Therefore, assuming a small value for μ compared to the characteristic time

increments, this strategy can improve the convergence rate without compromising the results (SIMULIA, 2017). After performing a sensitivity analysis of μ based on Szczecina e Winnicki (2017) on a simpler model, the value of 0.001 was defined.

Table 14 – Plasticity parameters.

Dilation Angle (ψ)	**Eccentricity (ϵ)**	σ_{b0}/σ_{c0}	K	**Viscosity parameter (μ)**
40°	0.1	1.16	0.6667	0.001

Source: The Author (2022)

Regarding the uniaxial stress-strain relationships, as seen in Section 3.3.1, the CDP model behaves differently for tensile and compressive conditions. From the relations obtained in Section 3.3.1.3, the data in Tables 15 and 17 must be passed onto *Abaqus*. They show how compression hardening and tension softening were given in terms of inelastic and cracking strains, respectively. Those are automatically converted into plastic strains by *Abaqus*, which must obey the previously established rule of positive values increasing monotonically – except for $\sigma_c \leq \sigma_{cu}$, where $\varepsilon_c^p = 0$. Moreover, the post-failure tensile yield stress must not be lower than one-hundredth of the initial failure stress ($\sigma_t \geq \frac{\sigma_{t0}}{100}$).

Finally, the damage behaviour is assigned to the material in the form of damage-strain relationships, exactly as shown in Section 3.3.1.3. Tables 16 and 18 display the values for d_c x ε_c^{in} and d_t x ε_t^{ck}, respectively, in the tabular format *Abaqus* requires.

Table 15 – Tensile behaviour.

Yield stress σ_t (Pa)	**Cracking strain ε_t^{ck} (-)**
2027528	0
1244117	0.0000588
804754	0.0001175
569349	0.0001763
440364	0.0002350
360697	0.0002938
301302	0.0003525
249644	0.0004113
201644	0.0004701
156870	0.0005288
116018	0.0005876
79785	0.0006463
48483	0.0007051

Source: The Author (2022)

Table 16 – Tension damage.

Damage parameter d_t (-)	**Cracking strain ε_t^{ck} (-)**
0	0
0.39	0.0000588
0.60	0.0001175
0.72	0.0001763
0.78	0.000235
0.82	0.0002938
0.85	0.0003525
0.88	0.0004113
0.90	0.0004701
0.92	0.0005288
0.94	0.0005876
0.96	0.0006463
0.98	0.0007051

Source: The Author (2022)

Table 17 – Compressive behaviour.

Yield stress σ_c (Pa)	**Inelastic strain ε_c^{in} (-)**
15200000	0
18064953	0.0000543
21482714	0.0000918
24586772	0.0001389
27374711	0.0001956
29844095	0.0002619
31992459	0.0003381
33817313	0.0004241
35316143	0.0005201
36486408	0.0006260
37325540	0.0007420
37830945	0.0008682
38000000	0.0010046
37848219	0.0011431
37391367	0.0012908
36627162	0.0014479
35553298	0.0016144
34167448	0.0017904
32467261	0.0019760
30450361	0.0021712
28114350	0.0023762
25456805	0.0025909
22475278	0.0028156

Source: The Author (2022)

Table 18 – Compression damage.

Damage parameter d_c (-)	**Inelastic strain ε_c^{in} (-)**
0	0
0	0.0000543
0	0.0000918
0	0.0001389
0	0.0001956
0	0.0002619
0	0.0003381
0	0.0004241
0	0.0005201
0	0.000626
0	0.000742
0	0.0008682
0	0.0010046
0	0.0011431
0.02	0.0012908
0.04	0.0014479
0.06	0.0016144
0.10	0.0017904
0.15	0.001976
0.20	0.0021712
0.26	0.0023762
0.33	0.0025909
0.41	0.0028156

Source: The Author (2022)

Only one step is lacking to fulfil all the materials' definitions: the designation of the plastic behaviour for the steel reinforcement bars (*MatSteel_epp*). Given the assumption of elastic perfectly-plastic behaviour, no more than the yield stress paired with a plastic strain value of zero is needed (see Table 19), in which case *Abaqus* assumes a constant response outside the range of stress provided: the stress on the bars will never reach beyond 435MPa (SIMULIA, 2017).

Table 19 – Plastic behaviour for *MatSteel_epp*.

Yield stress - f_y (MPa)	**Plastic strain - ε_y (-)**
435	0

Source: The Author (2022)

Note that for all these tabular data inputs, *Abaqus* interpolates linearly between

the points provided to build the material response. Furthermore, for all the materials, it was important to inform the density property to allow the software to compute the gravitational load. Table 20 presents the values adopted.

Table 20 – Materials' densities.

Material model	**Density - ρ (kg/m³)**
MatConc_lin	2400
MatSteel_lin	7850
MatConc_CDP	2400
MatSteel_epp	7800

Source: The Author (2022)

After the materials' behaviours are specified, they can be assigned to the corresponding geometries.

- Assembly

Until this stage, the software recognises separate geometrical entities – the *parts* defined in the first step – with specific material properties. In order to get a structural system which can be numerically analysed, an assembly of those geometries must be formed. That means placing the *parts* together in their appropriate amount and relative positions.

Before effectively joining different parts, *Part_Concrete* and *Part_EmbRing* were placed together to generate a new one: *Part_Concrete_Cut*, resulting from the removal of volume corresponding to *Part_EmbRing* from *Part_Concrete* (Figure 70).

Figure 70 – *Part_Concrete_Cut*.

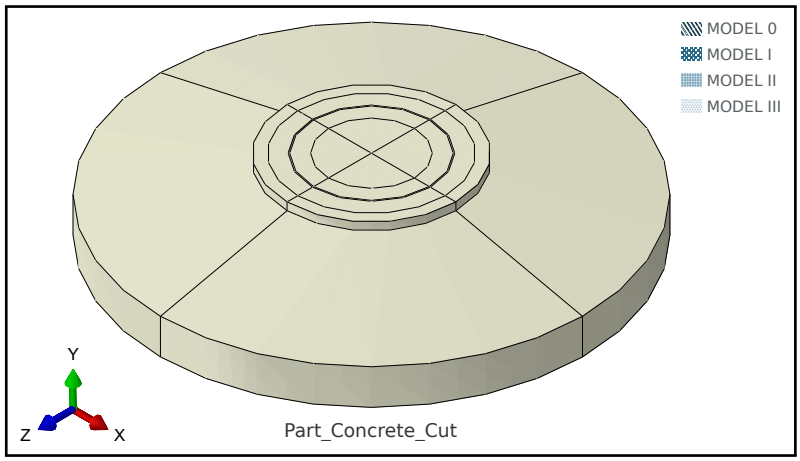

Source: The Author (2022)

Figure 71a shows the *assembly* formed for Model I and also used for models 0 and II. For Model III, the reinforcement bars were added to the structural system. Figure 71b schematises the *assembly* for that model, with "*All_bar_parts*" used to represent all the different reinforcement steel *parts* and their copies created in the *assembly*.

Figure 71 – *Assembly*.

(a) Simple concrete *assembly*.

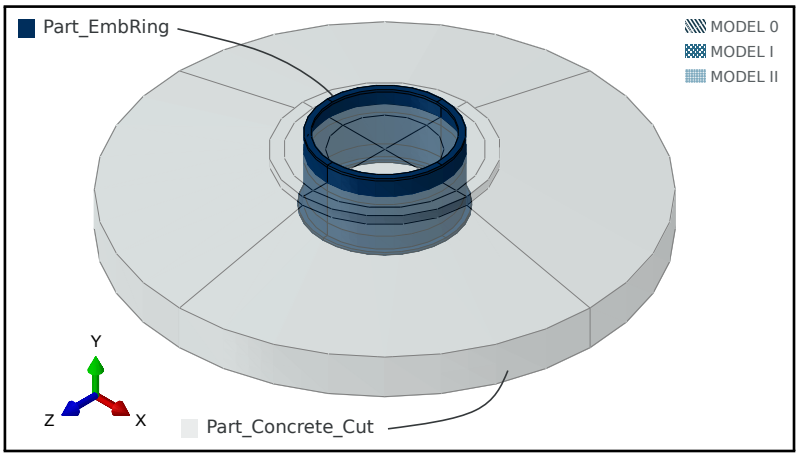

(b) Reinforced concrete *assembly*.

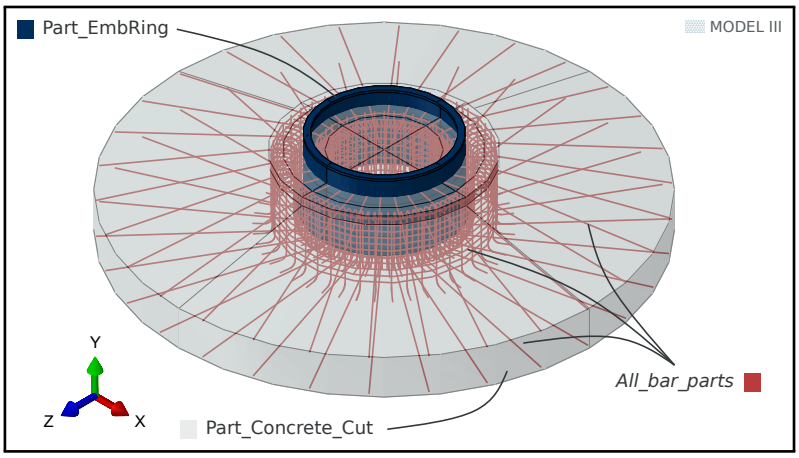

Source: The Author (2022)

- Meshing

Before presenting the mesh used for the models, some issues regarding the mesh generation will be discussed. Note that the model conditions for what will be related here are those of Model I.

First, geometry-imposed hindrances had to be overcome: the circular characteristic of the foundation geometry prevented *Abaqus* from meshing the *assembly* directly without some editing. That took the form of *partitions*, features applied to create simpler

geometrical volumes from the original, more complex structure by cutting through it with user-defined planes. Figure 72 illustrates some of the *partitions* that had to be implemented to allow regular meshing.

Figure 72 – Illustration of *Partitions*.

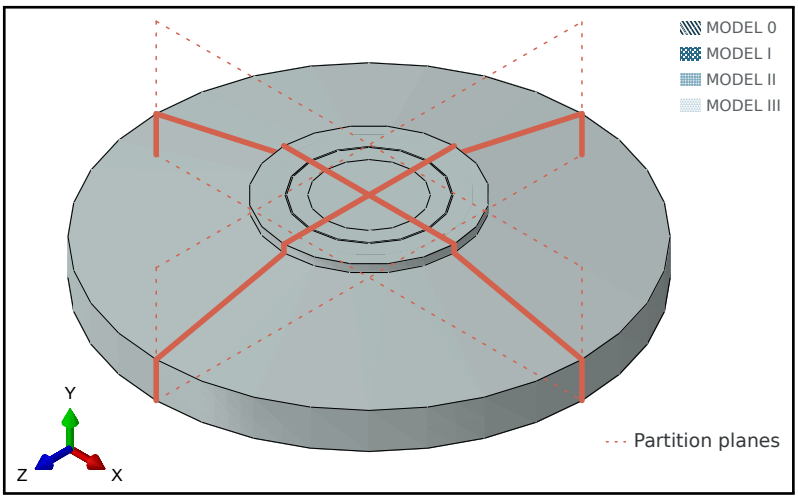

Source: The Author (2022)

Besides those “mandatory” *partitions*, some were made on a discretionary basis to delineate a region for a finer mesh. The finer the mesh, the higher the accuracy of the results. However, the finer the mesh, the higher the computational cost. Refining the entire model is also counterproductive since the increase in cost does not come with significant response changes in areas where stress distribution does not alter abruptly. That is why it is convenient to confine the refinement of the mesh to regions of stress concentration.

To understand where the mesh refinement would most likely improve the results, a base model, grossly meshed, was analysed for regions of stress concentration. With no surprise due to literature-reported results, stress concentrations were found in the concrete surrounding the bottom flange of the ring.

That led to the partitioning of the region highlighted in Figure 73, where the progressive refinement took place. The results for the subsequent mesh sizes were studied in a convergence analysis to determine the appropriate mesh for the models. Details on this study will be presented further in Section 4.1.2.

Abaqus provides a tool for automatic refinement based on analyses’ results and user-defined settings. However, the element type available to use this feature on 3D models was not of interest to the research. The choice of element for the solid concrete base followed the study of a benchmark analysis of the available elements

Figure 73 – Refinement region.

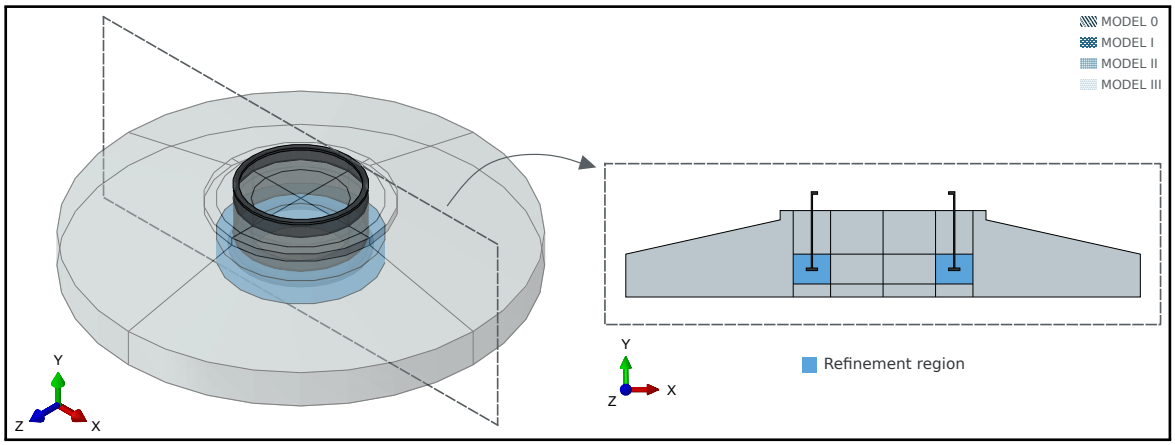

Source: The Author (2022)

(HEMANTH et al., 2010), the understanding of *Abaqus*'s description of its solid elements (SIMULIA, 2017) and the analysis of which elements other researchers in the field of wind turbine foundation modelling tended to work with (BAI et al., 2017a; CHEN; XU; LI, 2020; CHEN et al., 2021). All this culminated in the selection of the C3D8R: an 8-node linear brick, reduced integration (with hourglass control) element (Figure 74a). Its active degrees of freedom are the nodal displacements in all three spatial directions: X (1), Y (2) and Z (3), and due to the reduced integration feature, the element presents only one integration point where element outputs are collected (Figure 74b). These outputs are available in all the six components exemplified in Figure 74b for the stresses. An important advantage of this feature lies in the lesser volume of output generated by analysis, meaning smaller file sizes and computation costs.

Figure 74 – The C3D8R element.

(a) Node ordering and face numbering of the element.

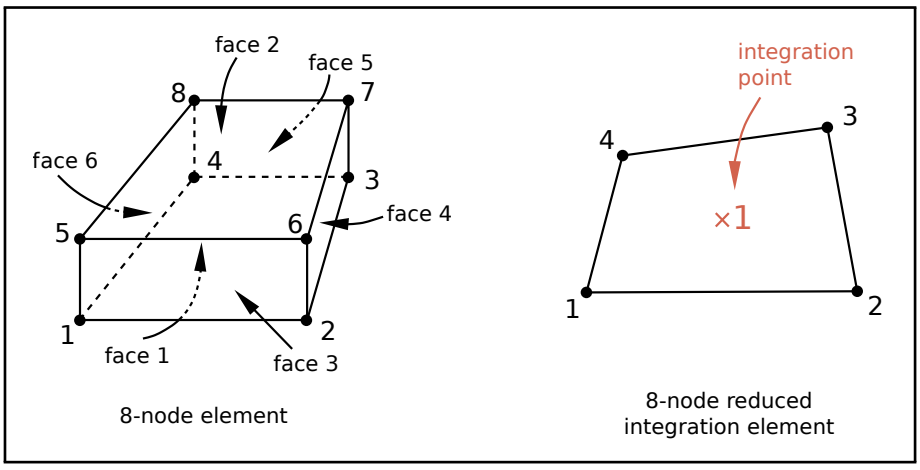

Source: Adapted from Simulia (2017)

(b) Details on nodal and element outputs.

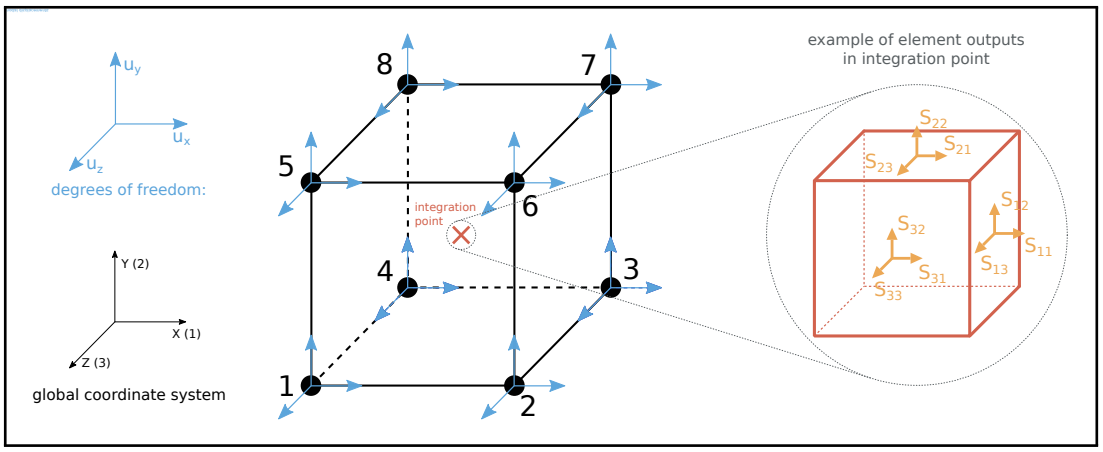

Source: The Author (2022)

This element was used to mesh the embedded ring and the concrete foundation structures. For the reinforcement steel bars, a 3D truss element, the T3D2 (2-nodes, linear element), was used (Figure 75a). Again, active degrees of freedom are nodal displacements in the global 3D space directions, but the element outputs are only available in the local axial direction (Figure 75b).

Figure 75 – The T3D2 element.

(a) Element node ordering.

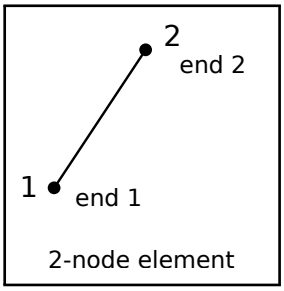

Source: Adapted from Simulia (2017)

(b) Details on nodal and element outputs.

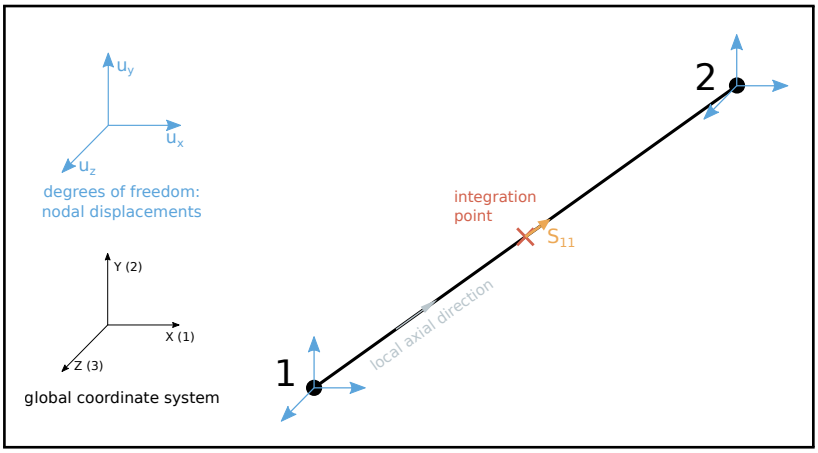

Source: The Author (2022)

As aforementioned, Section 4.1.2 will detail further how the mesh size and configuration were determined. Table 21 only summarises the number of elements for each *part* or referred set.

Table 21 – Number of elements per referred set of *parts*.

Element type	*Part*	Number of elements	Model presence
C3D8R	*Part_Concrete_Cut*	18840	0, I, II, III
C3D8R	*Part_EmbRing*	1520	0, I, II, III
T3D2	*All_bar_parts*	5580	III

Source: The Author (2022)

- Constraints and interactions

One of the previously-described stages – *assembly* – talked about how the *parts* had to be placed together to form a structural system capable of undergoing analysis. However, simply positioning *parts* relative to each other is insufficient to inform *Abaqus* that they will be working together or how this will occur: it is necessary to apply an *interaction* property.

In the interfaces between the embedded ring and the concrete base (see Figure 76), two different conditions were studied: (i) the assumption of perfect adherence between the materials and (ii) the consideration of touching brought on by the loading. For the first scenario, (i), a *tie constraint* was applied to the boundary surfaces. This feature ties distinct surfaces together, preventing relative motion between them, even if their meshes are disparate.

Figure 76 – Surfaces between the embedded ring and the concrete base.

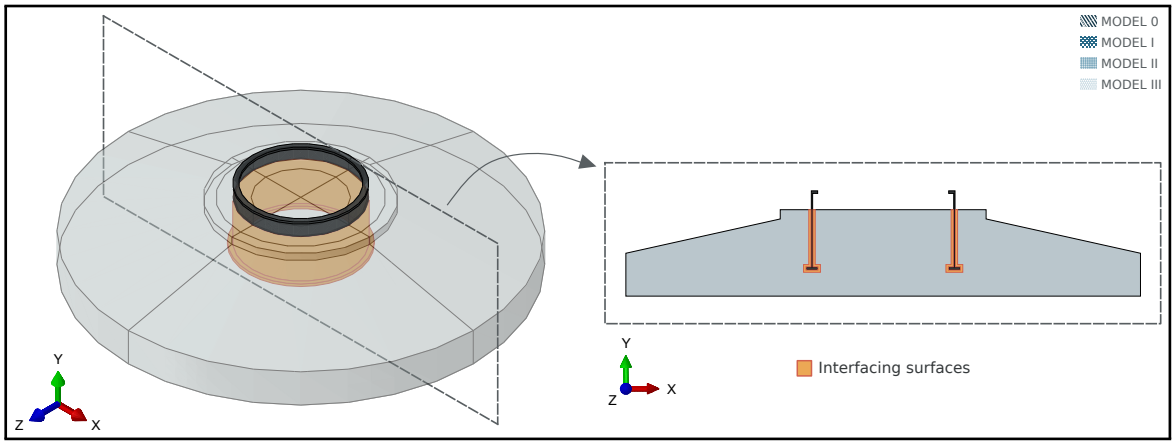

Source: The Author (2022)

For the second circumstance, (ii), a *contact interaction* property had to be defined. That was created as surface-to-surface, with the steel ring as the master surface due to its higher E and the slave adjustment set to remove overclosure only. Important to highlight to the reader how the foundation geometry's circular characteristic required

additional steps to allow the simulation to go through correctly. In FEM, curved geometric surfaces are approximated as a faceted set of connected element faces (SIMULIA, 2017) (Figure 77a). Therefore, unless *Abaqus* is requested to automatically smooth 3D geometry surfaces, which then brings them closer to the true curved geometry (Figure 77b), the contact algorithm might consider that a slave node is behind its master surface reference and apply a considerable force to remove this penetration. If this force is too high, it will lead to local initialisation of stress and strain, and the governing equation will not converge.

Figure 77 – Particularities of a circular geometry.

(a) Faceted surfaces with overlapping edges.

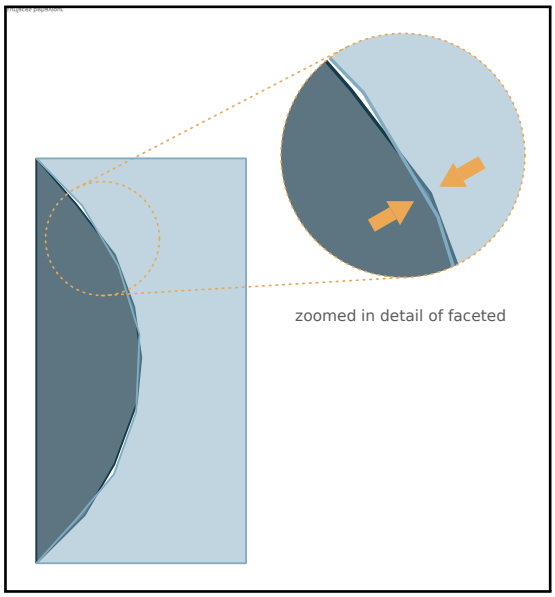

(b) True geometric surface.

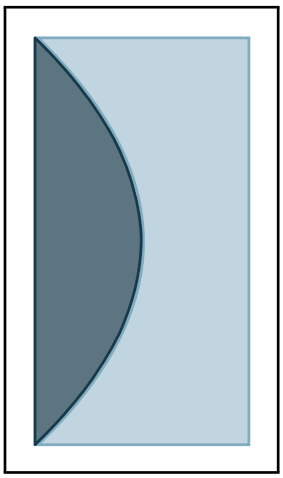

Source: The Author (2022)

In terms of the parameters used to configure the *contact* behaviour, they were based on reports from the literature. Following (HE et al., 2019; ZHOU; KONG; DOW, 2015; CHEN et al., 2021), a Coulomb contact constraint was implemented, with a friction coefficient of 0.3 and a hard contact model for the pressure-overclosure relationship. The latter meant that no penetration of the slave nodes into the master surfaces was allowed.

The *tie constraints* were used for Model 0 and Model I, while the *contact* was applied to Model II and Model III (Figure 78). Those different ways of modelling the interaction between the ring and the concrete mean different load-transfer mechanisms. More on this when the results and discussions are brought forth.

Figure 78 – Embedded ring to concrete interaction types.

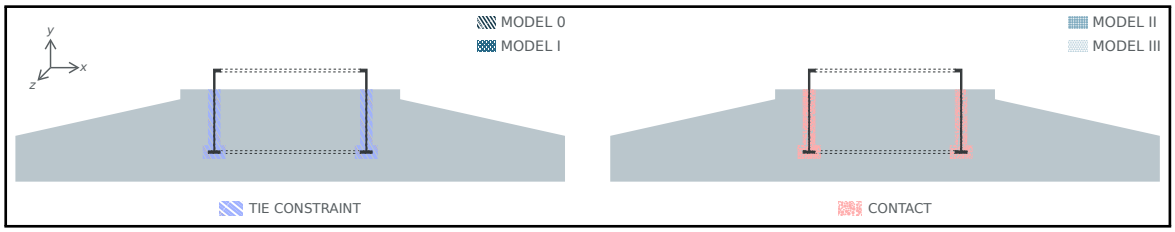

Source: The Author (2022)

In the case of the steel reinforcement bars, the assumption was of perfect bond behaviour between the steel and the concrete. *Abaqus* provides a specific constraint to be applied to the bar elements, called *embedded region*, which creates this type of relation. That works by constraining the translational degrees of freedom of the nodes embedded to those from the host elements. Figure 79 highlights the reinforcement bars which were embedded into the host region of the remaining foundation.

Figure 79 – Embedded reinforcement bars.

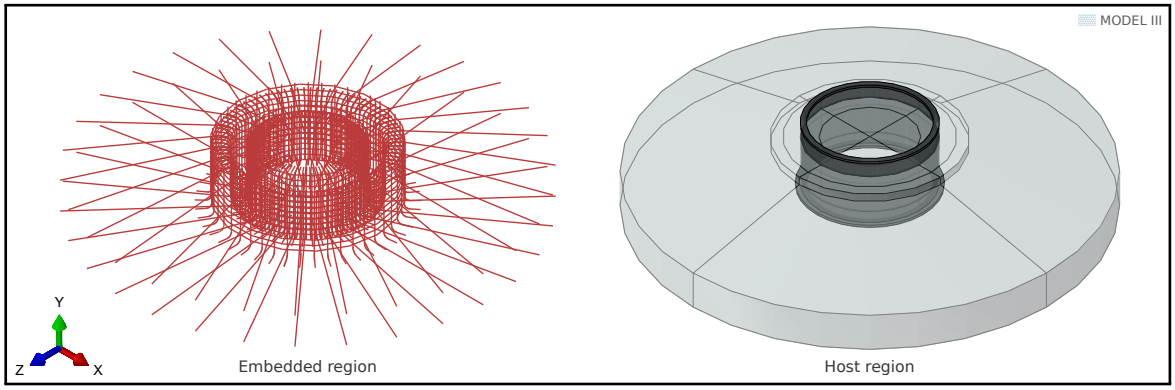

Source: The Author (2022)

Besides the already presented features, one more deserves mentioning: a *rigid body constraint* used to create the setting for applying the concentrated loads on top of the foundation. This constraint was applied to the top flange of the embedded ring, enforcing a rigid-body motion to the nodes on this portion of the structure, governed by a *reference point* (RP) in the centre of the ring's top surface (see Figure 80). The reason for this is not only the definition of a point where loads can be applied to with their effects carried consistently to the structure but also to avoid stress concentrations from spiking in the ring if the high loads were directly applied onto it. This constraint was used in all four models.

Figure 80 – Rigid body constraint.

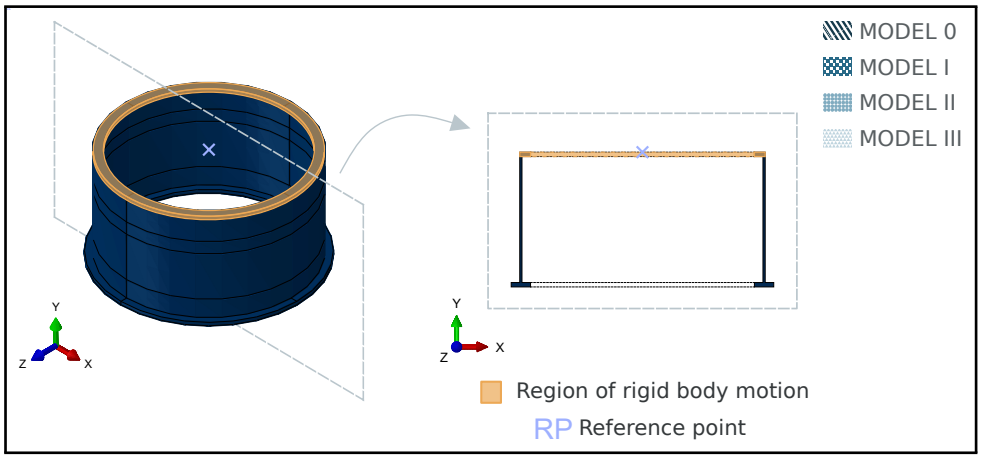

Source: The Author (2022)

- Loads

The reference point introduced in the previous stage served as the point of application for the concentrated loads transmitted from the tower to the foundation, whose values have already been presented in Sections 2.3 and 3.2. Figure 81 replicates the schematics of this system of loads to highlight its association with the RP in question.

Figure 81 – Concentrated loads.

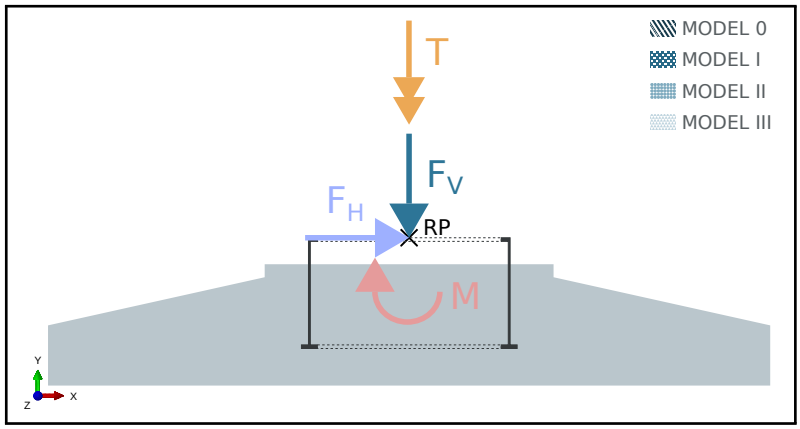

Source: The Author (2022)

The soil backfill was applied as a surface traction kind of load distributed over the tapered surface of the foundation (Figure 82). The weight distribution was approximated to a uniform value of 14.4kN/m² according to the rationale shown in Section 3.2, Figures 34a and 34b.

Finally, the foundation self-weight (sw) was considered through the designation of a gravity-type load. The load was defined as -9.81 - the gravitational acceleration ($g : m/s^2$) - pointing towards the ground and acting over the whole model. Internally,

Figure 82 – Soil backfill load.

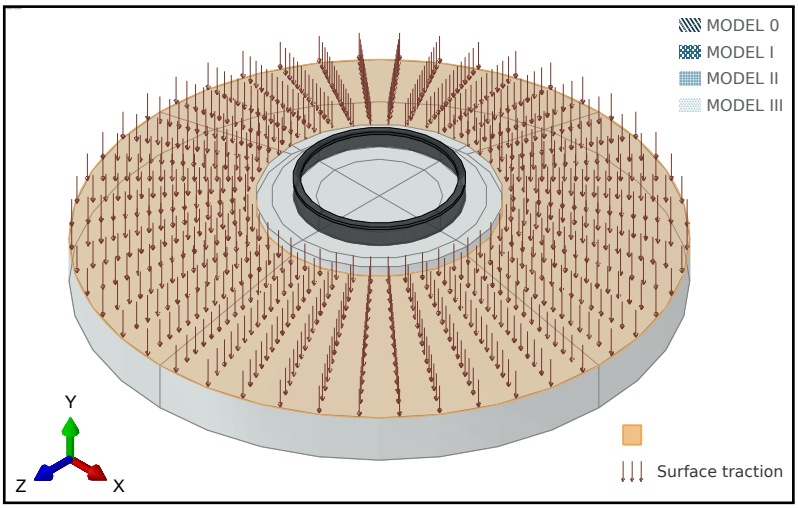

Source: The Author (2022)

Abaqus used g, the materials' densities and corresponding volumes to determine the total weight.

- Supports

Regarding the support conditions, the research studied the behaviour of the foundation with two different assumptions. One was the consideration of rigid supports, blocking translational displacements in all three directions – X, Y and Z. The other was the consideration of elastic supports in the form of springs aiming to take into account the SSI as discussed in Section 3.1. For the first case, it sufficed to define the boundary region as the entire bottom surface of the foundation and set the translational degrees of all its nodes to 0. For the latter, however, a few more steps were necessary.

Firstly, nodes for the edge and the internal region of the bottom surface, besides the nodes for the entire region, had to be collected separately, forming three different sets of nodes (Figure 83) since their vertical moduli of subgrade reaction differed. Then, the spring elements with the correct properties of acting direction and stiffness had to be created for the corresponding set of nodes (Table 22). However, to have the vertical springs active only under compression, the model's input file had to be edited to include the nonlinear behaviour. For that, pairs of force-displacement values that can reproduce the nonlinear relationship (Figure 84) must be defined, noting that *Abaqus* assumes a constant force outside the range of values provided. Table 23 shows the range of data input used to set the edge and internal springs behaviours.

Figure 83 – Sets of nodes on the bottom surface.

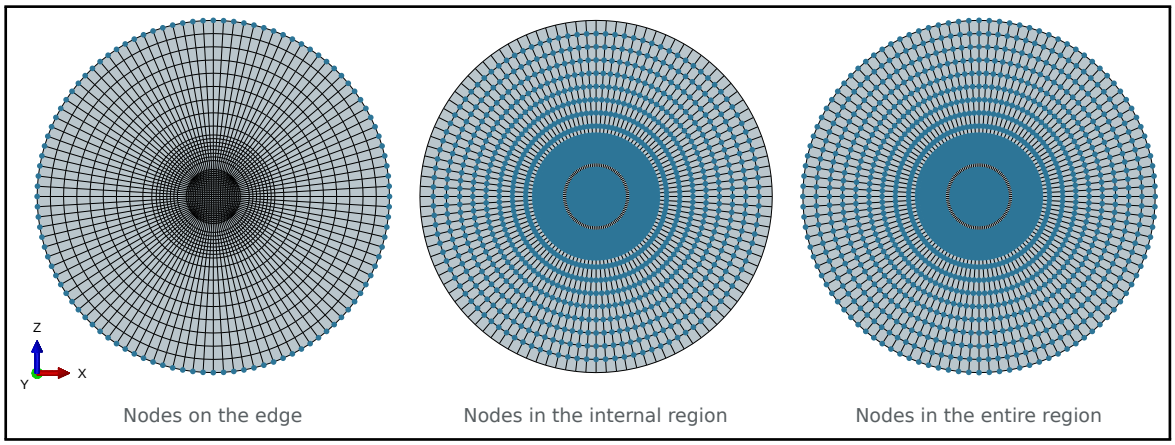

Source: The Author (2022)

Table 22 – Springs configuration.

Sets of nodes	Direction	Stiffness
- nodes in the entire region -	horizontal (x)	$k_H = 32000\,kN/m^2/m$
- nodes in the entire region -	horizontal (z)	$k_H = 32000\,kN/m^2/m$
- nodes in the internal region -	vertical (y)	$k_{Vi} = 160000\,kN/m^2/m$
- nodes on the edge -	vertical (y)	$k_{Ve} = 320000\,kN/m^2/m$

Source: The Author (2022)

Figure 84 – Nonlinear force-displacement spring relationship.

(a) Theoretical.

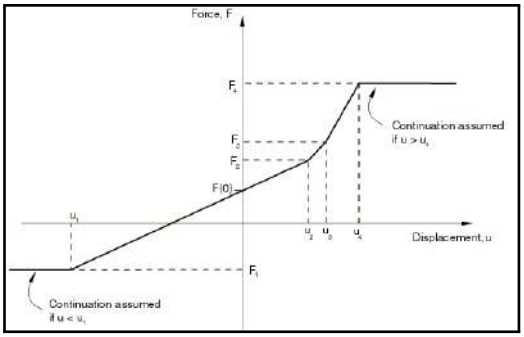

Source: Simulia (2017)

(b) k_{Ve}.

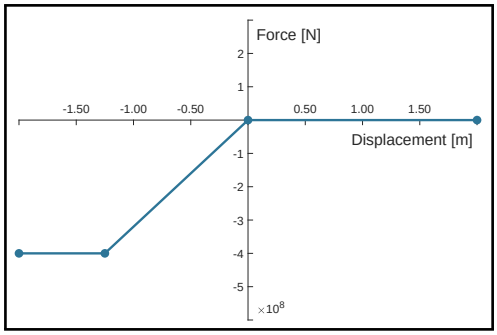

Source: The Author (2022)

Table 23 – Nonlinear data input.

Stiffness	Force (N)	Displacement (m)
$k_{Vi} = 160000\,kN/m^2/m$	$-2 \cdot 10^8$	-1.25
	0	0
$k_{Ve} = 320000\,kN/m^2/m$	$-4 \cdot 10^8$	-1.25
	0	0

Source: The Author (2022)

Figure 85 illustrates which models were built with rigid supports and which used springs (both linear for the horizontal springs and nonlinear for the vertical ones).

Figure 85 – Boundary conditions.

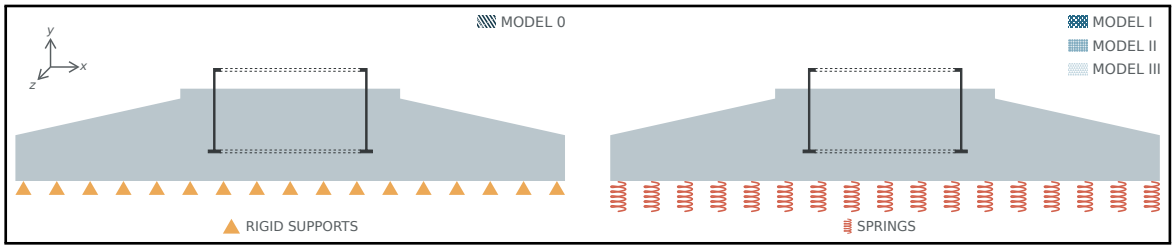

Source: The Author (2022)

4.1.2 Convergence analysis

Following what was introduced, a convergence analysis was executed with five replicas of Model I with different mesh sizes. The upcoming steps were taken to allow consecutive refinement of the region previously presented (Figure 73).

Four subregions of elements, A, B, C and D, plus a circular path of nodes (Figure 86), were defined within the refinement region to control the variation of *Mises* stresses' results obtained with each model. Between the refined region and the remaining mesh,

Figure 86 – Control regions.

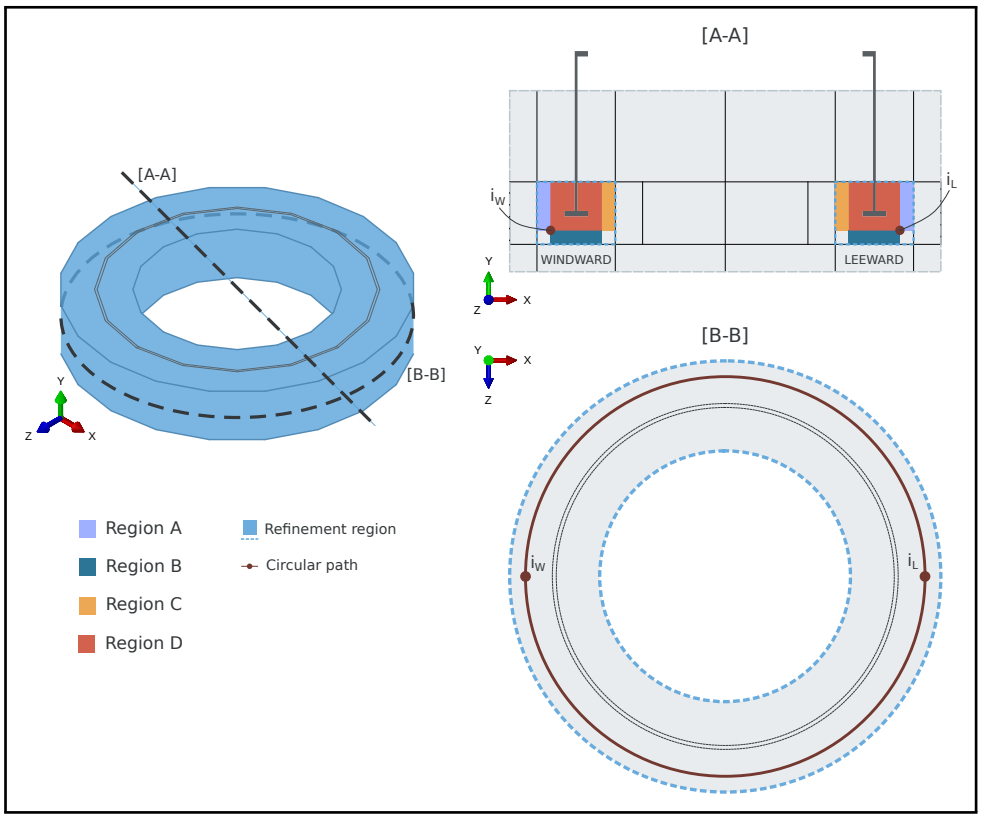

Source: The Author (2022)

a transition zone with element shapes less regular was concocted to connect them (Figure 87), allowing the link between smaller- and standard-sized elements. Lastly, specific edges were used to set the size of elements (Figure 88).

Figure 87 – Transition mesh.

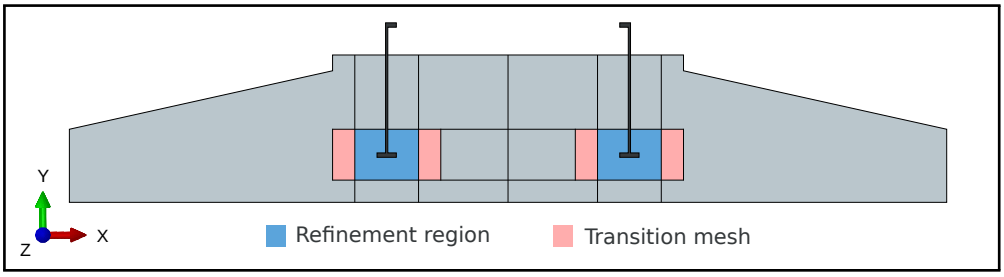

Source: The Author (2022)

Figure 88 – Control edges.

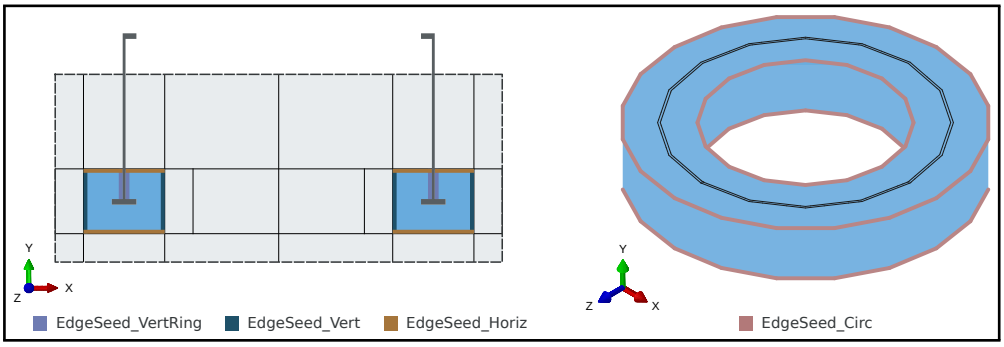

Source: The Author (2022)

Figure 89 presents a cross-section for Model I with the resultant mesh configuration within the above-described design criteria. It helps guide the interpretation of Table 24, which shows the details of the meshes studied, including the size of the elements assigned for each edge of control.

Table 24 – Convergence analysis details.

	Size of elements in control edges (m)				**Mesh size**		
	EdgeSeed_ Circ	**EdgeSeed_ Horiz**	**EdgeSeed_ Vert**	**EdgeSeed_ VertRing**	**Elements**	**Nodes**	**DOF**
Mesh01	0.50	0.50	0.50	0.50	7568	10623	31869
Mesh02	0.30	0.30	0.30	0.30	8720	12027	36081
Mesh03	0.30	0.15	0.15	0.15	10176	13707	41121
Mesh04	0.15	0.15	0.15	0.15	20360	25961	77883
Mesh05	0.15	0.15	0.075	0.075	35524	41351	124053

Source: The Author (2022)

Figure 89 – Mesh configuration example.

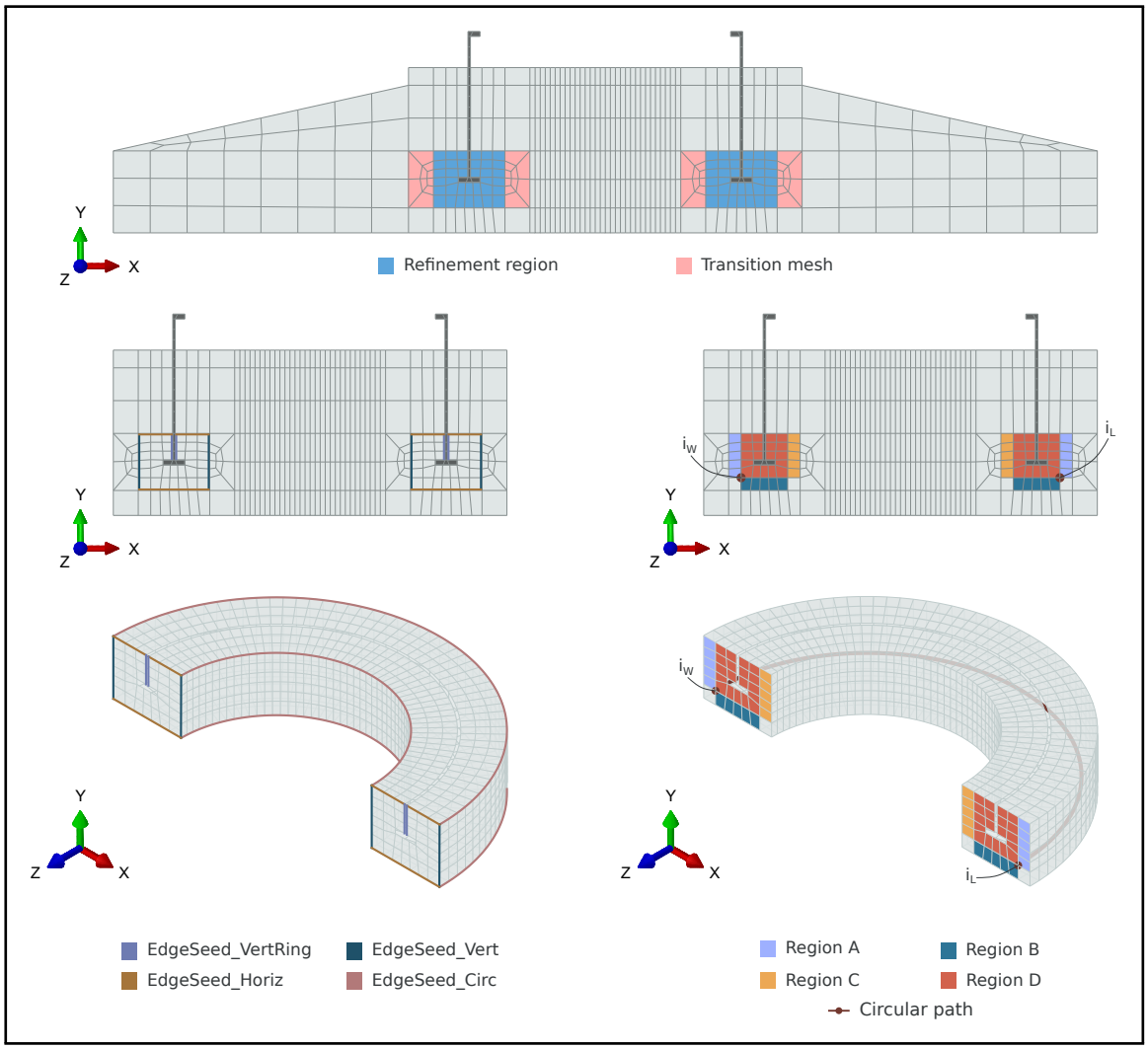

Source: The Author (2022)

The Mises stresses obtained are graphed in Figures 90 to 91. It is clear from the data that Mesh04, with 20360 elements and 25961 nodes, reflects the best cost-effective mesh scenario. Table 25 further confirms this, showing the relative error of each mesh's

Table 25 – Mises' stress error relative to Mesh04.

	Mises stress % error relative to Mesh04							
	Windward regions				**Leeward regions**			
	A	**B**	**C**	**D**	**A**	**B**	**C**	**D**
Mesh01	5%	1%	2%	1%	3%	9%	8%	8%
Mesh02	4%	1%	1%	0%	3%	8%	7%	7%
Mesh03	2%	1%	4%	1%	2%	8%	4%	4%
Mesh05	1%	2%	1%	1%	0%	2%	1%	1%

Source: The Author (2022)

result regarding Mesh04's outputs. From the subregions analysed, the largest offset from the finest mesh (Mesh05) is 2%, which does not justify its high-cost use due to longer execution time.

Figure 90 – Convergence analysis of *Mises* stress – circular path.

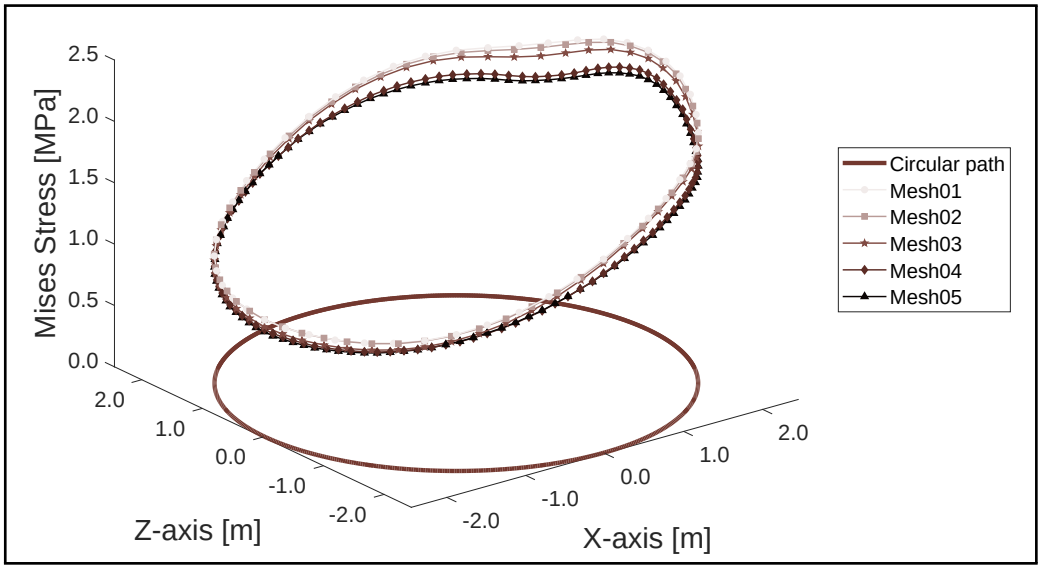

Source: The Author (2022)

Figure 91 – Convergence analysis of *Mises* stress – element regions.

(a) Windward regions.

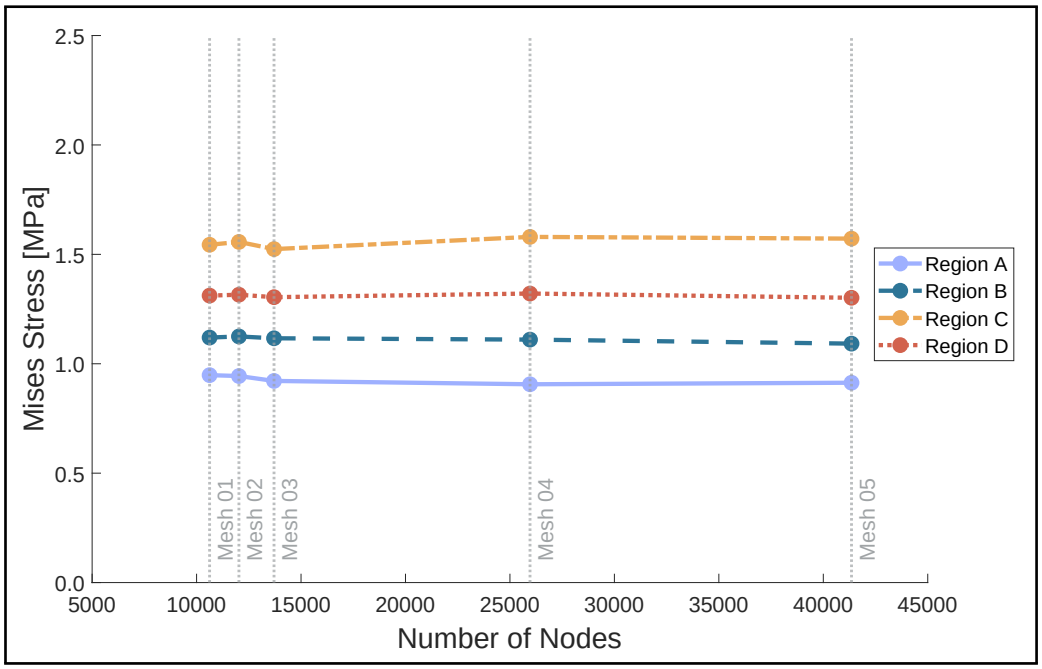

(b) Leeward regions.

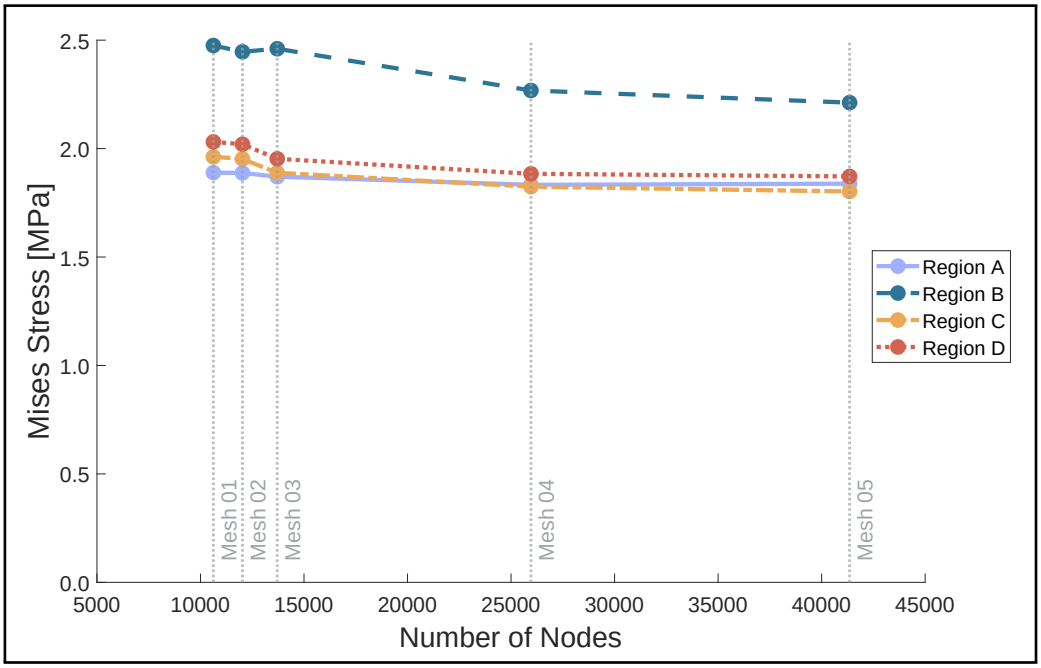

Source: The Author (2022)

4.2 MODEL 0

This section presents the characteristics and results of Model 0.

4.2.1 The model

Model 0 was built with linear concrete and steel, tie constraint as the interaction feature and rigid supports attaching the foundation base to the ground (Figure 92). This latter condition is the model's only difference to Model I since the focus here was to

Figure 92 – Model 0.

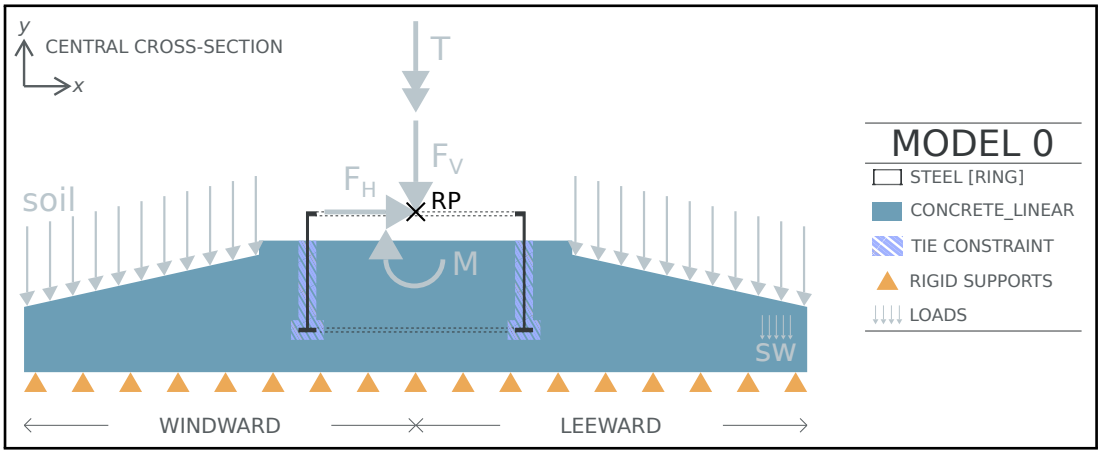

Source: The Author (2022)

understand the impact of the different boundary conditions on the stress distribution.

Section 4.1 unveiled how the mesh was determined and informed on its size (Table 21). Figure 93 shows a cross-section of the mesh configuration for the given model. Note that it will also apply to models I and II.

Figure 93 – Mesh configuration - Models 0, I and II.

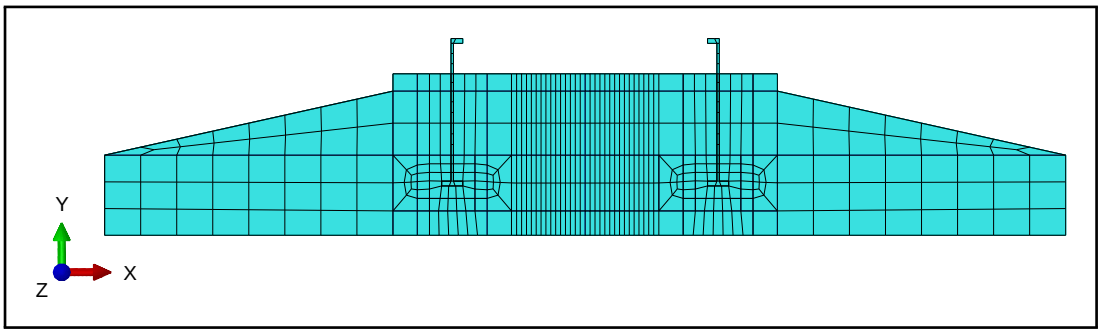

Source: The Author (2022)

4.2.2 The results

The results from the simulation of Model 0, which took 00h01m33s to process, will now be presented.

Regarding the values and distribution of the principal stresses developed on the concrete base, there is a noticeable symmetry in the stress behaviour with respect to the Z-axis (direction of the bending moment, M), as shown in the results in Figure 94. Specifically for Figure 94a, the highlight is on the high values of tensile stresses occurring in the windward region of the pedestal enclosing the embedded ring, which lie outside the material limit (f_t = 2.03MPa). Accordingly, Figure 94b shows stress concentration surrounding the ring walls. Notably, the higher values locate towards the

Figure 94 – Principal stresses – Model 0.

(a) Principal stresses distribution (Pa).

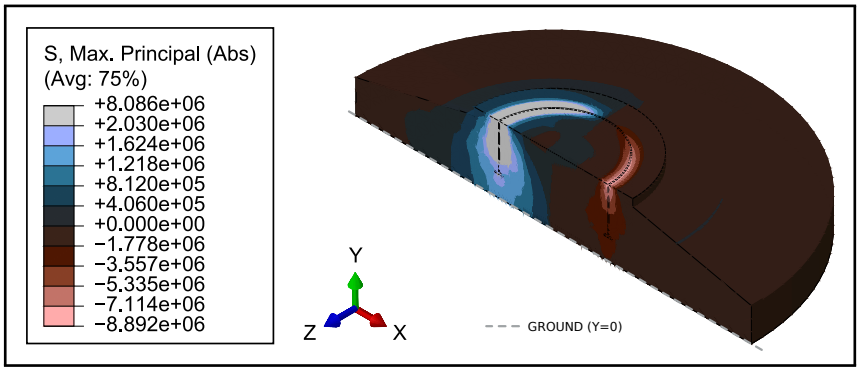

(b) Flow of principal stresses (Pa).

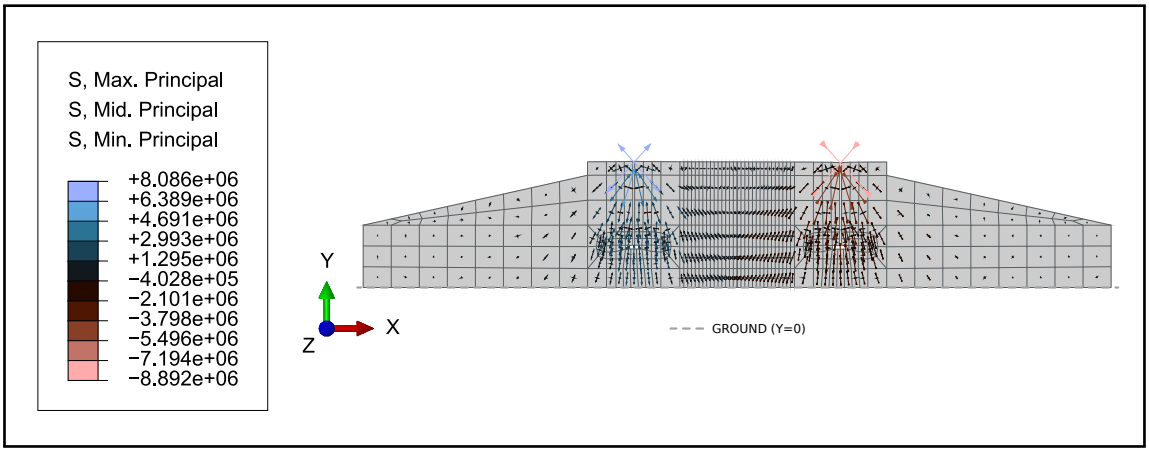

Source: The Author (2022)

top of the foundation, which might indicate that the load transmission mechanism in this model is not the bottom flange of the ring, as desired, but rather the areas near the load application.

Figure 95 presents the distribution of σ_{xx} stresses (S11), highlighting the position of the sections used for the design of the steel reinforcement for future comparisons (design performed with stress information from Model I). It shows stress concentration nearing the top of the ring, with tensile values exceeding f_t. Besides, the footing does not present a flexural behaviour. Instead, it is characterised by sections fully tensioned on the windward side and fully compressed on the leeward side, with values not higher than 0.41MPa and 0.89MPa, respectively.

Figure 95 – σ_{xx} stresses (S11) (Pa) – Model 0.

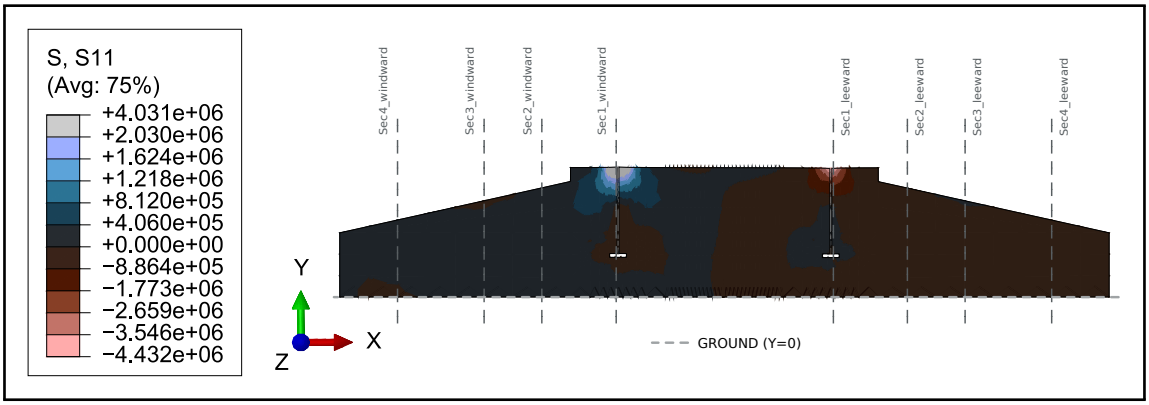

Source: The Author (2022)

Regarding the vertical stresses, σ_{yy} (S22), Figure 96a again shows higher stress values concentrating on the top, but bulbs of stress are visible beneath the bottom flange of the ring. The windward region is tensioned to a maximum value of 2.04MPa (beyond

the material limit), while the leeward side is compressed to a maximum of 2.45MPa (Figure 96b).

Figure 96 – σ_{yy} stresses (S22) – Model 0.

(a) σ_{yy} stresses (S22) (Pa) – cross-section.

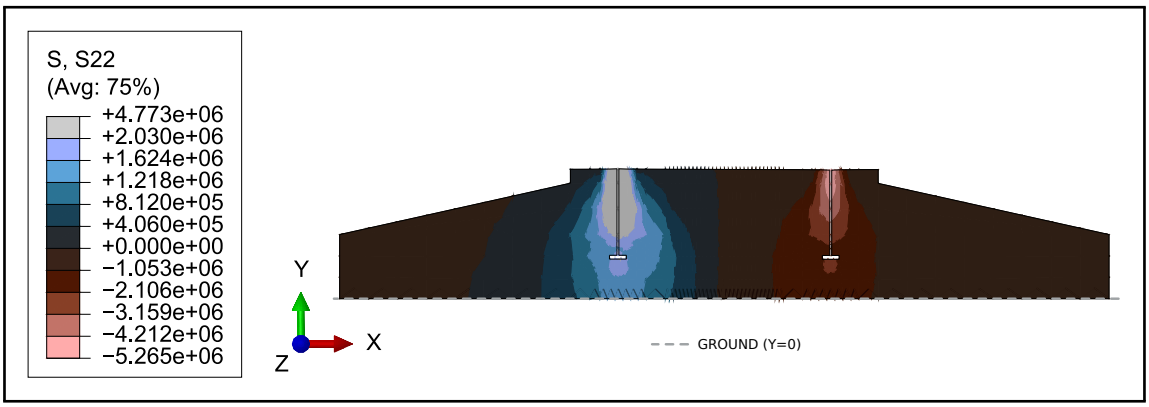

(b) σ_{yy} stresses (S22) (Pa) – refinement region.

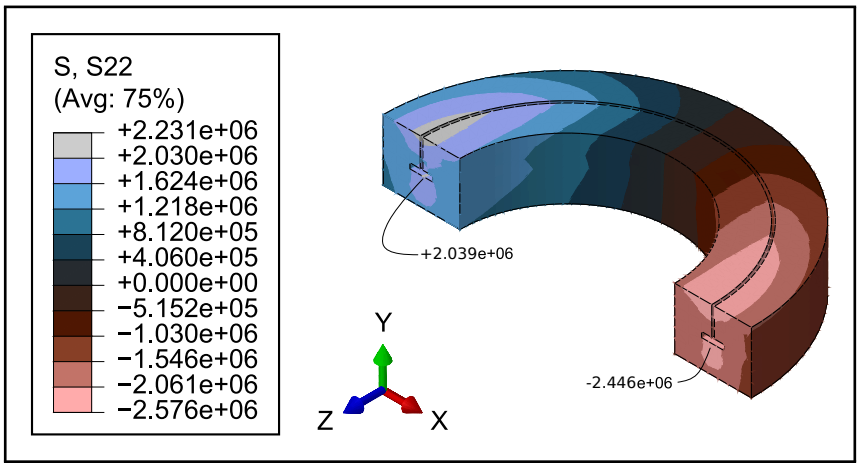

Source: The Author (2022)

Regarding the vertical displacements (U2), Figure 97 shows the behaviour of the ring–concrete set. Given the rigid supports applied to the bottom surface of the concrete, this region presents zero displacements from the ground, as does most of the foundation. Congruently to the σ_{yy} (S22) results, maximum displacement occurs in the top areas of the pedestal and embedded ring, with upwards movement on the windward side and downwards on the leeward side. Both structures displace together along the common boundaries, given the tie constraint, and overall to maximum values of 0.25mm for the concrete and 0.52mm for the embedded ring.

The horizontal (x) displacements (U1), on the other hand, concentrate their highest values on the top region of the pedestal inside the embedded ring (Figure 98).

Figure 97 – Vertical displacements (U2) – Model 0.

(a) U2 displacements (m) – perspective.

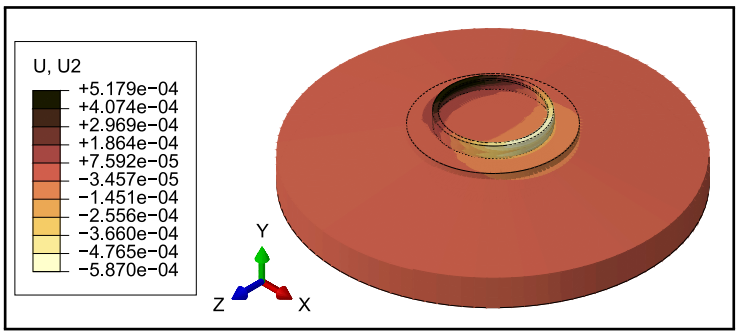

(b) U2 displacements (m) – cross-section.

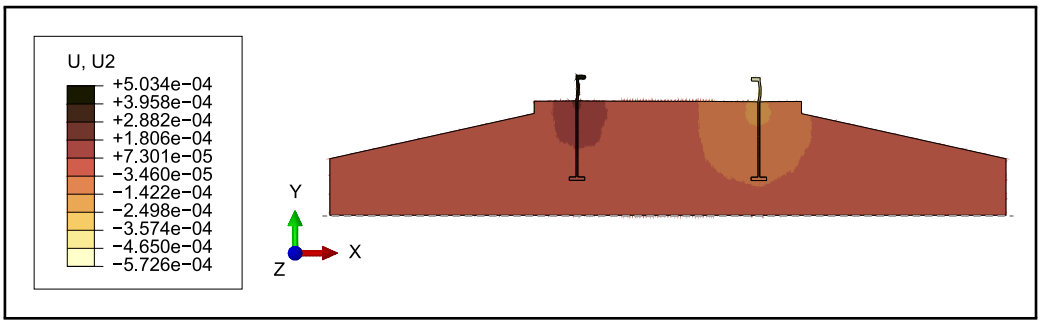

Source: The Author (2022)

Figure 98 – Horizontal displacements (U1) – Model 0.

(a) U1 displacements (m) - pedestal perspective.

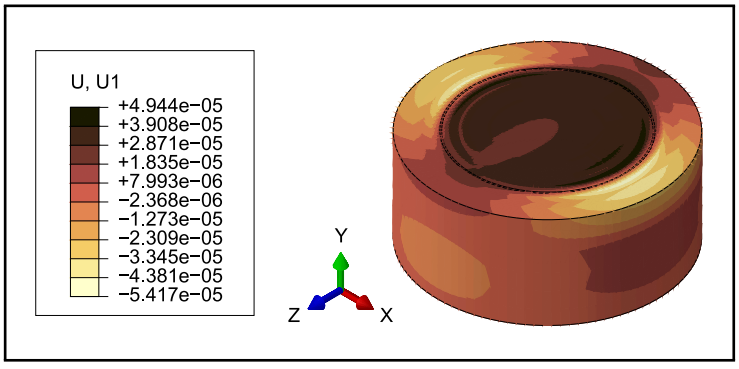

(b) U1 displacements (m) - pedestal cross-section.

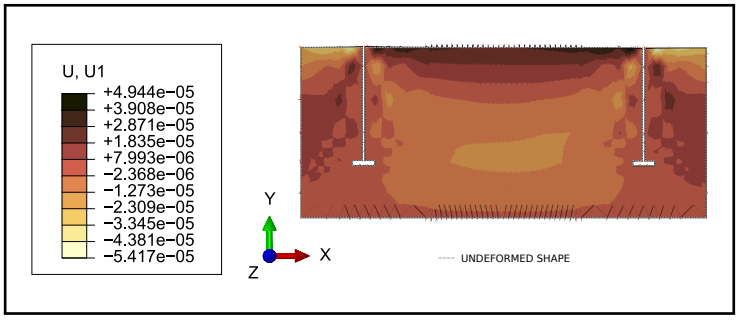

Source: The Author (2022)

4.3 MODEL I

This section presents the characteristics and results of Model I.

4.3.1 The model

Model I is represented in Figure 99. As previously mentioned, it is similar to Model 0 in its main specifications (linear behaviours for both steel-ring and concrete materials and tie constraint between the structural elements) except for the boundary condition: nonlinear springs were used for Model I. The mesh configuration for the model can be checked in Figure 93.

Figure 99 – Model I.

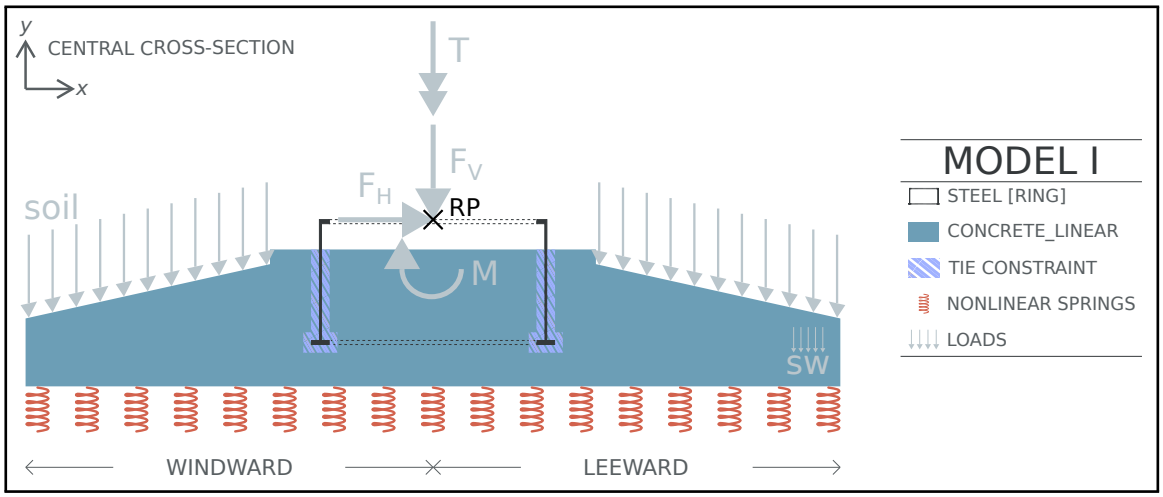

Source: The Author (2022)

4.3.2 The results

The results from Model I were processed in 00h01m42s. The principal stresses on the concrete are distributed according to Figure 100a. High values concentrate on the top of the concrete pedestal, neighbouring the steel ring, with tension reaching beyond f_t on the windward side and compression exceeding 10MPa on the leeward side. The tensile stresses distribute from there to the leeward foundation bottom, where they also surpass the material limit. The stress flow on the model cross-section is available in Figure 100b that provides greater insight into the behaviour of the tensile stress concentration beneath the leeward bottom flange.

Figure 101 shows the horizontal stress distribution with which the longitudinal reinforcement was dimensioned: σ_{xx} (S11). In this model, the footing's flexural behaviour

is clearly visible, with a zero-stress line practically crossing the foundation from one edge to the other, changing the acting stresses' signs as it passes the pedestal.

Figure 100 – Principal stresses – Model I.

(a) Principal stresses distribution (Pa).

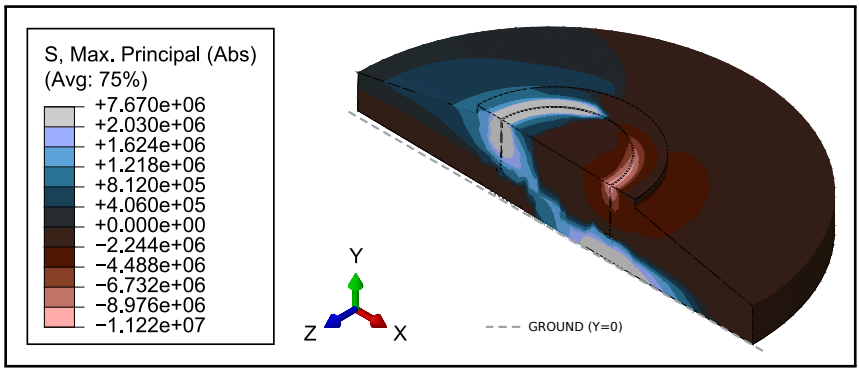

(b) Flow of principal stresses (Pa).

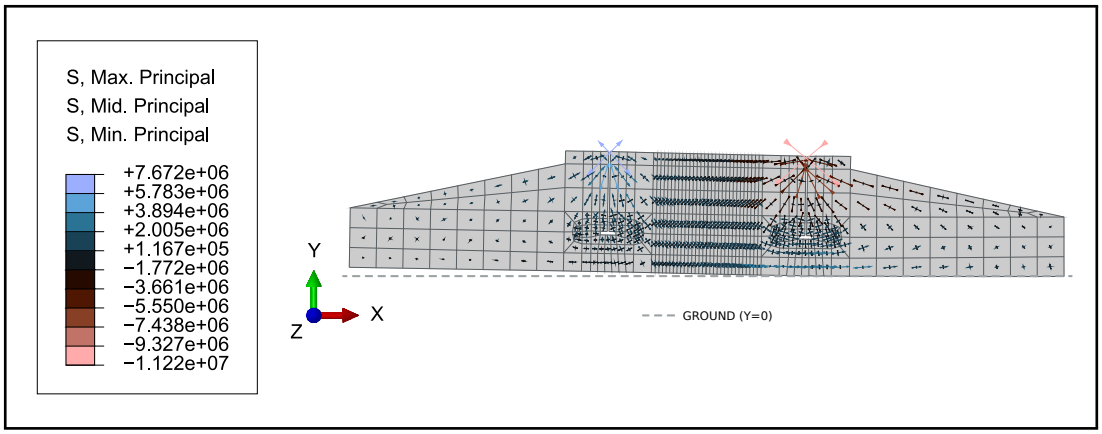

Source: The Author (2022)

Figure 101 – σ_{xx} stresses (S11) (Pa) – Model I.

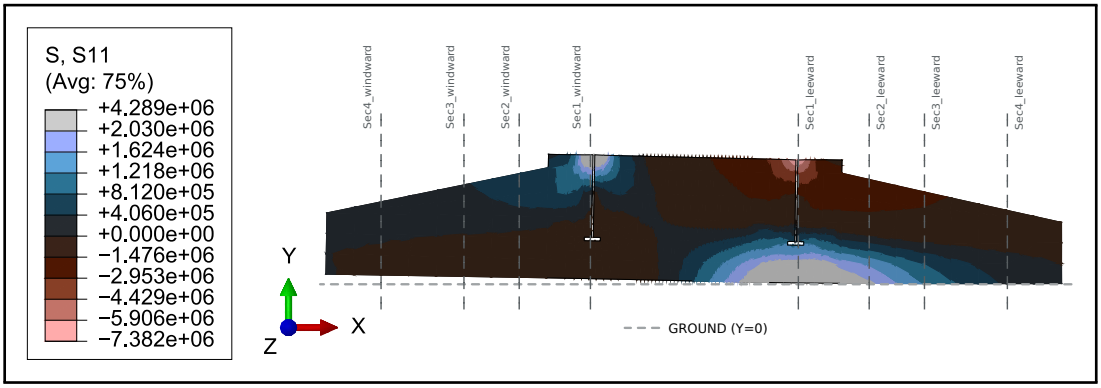

Source: The Author (2022)

The vertical stresses, σ_{yy} (S22), compress the entire leeward half of the foundation while almost entirely tensioning the windward half (Figure 102a). The highest values concentrate around the embedded ring, towards the top of the pedestal, with tensile

values exceeding f_t on the windward side. At the refinement region (Figure 102b), the apparent bulbs of stress beneath the flange are actually continuous with the stress distribution irradiating from the top. The maximum values around the bottom flange do not exceed 0.73MPa for tension and 1.12MPa for compression.

Figure 102 – σ_{yy} stresses (S22) – Model I.

(a) σ_{yy} stresses (S22) (Pa) – cross-section.

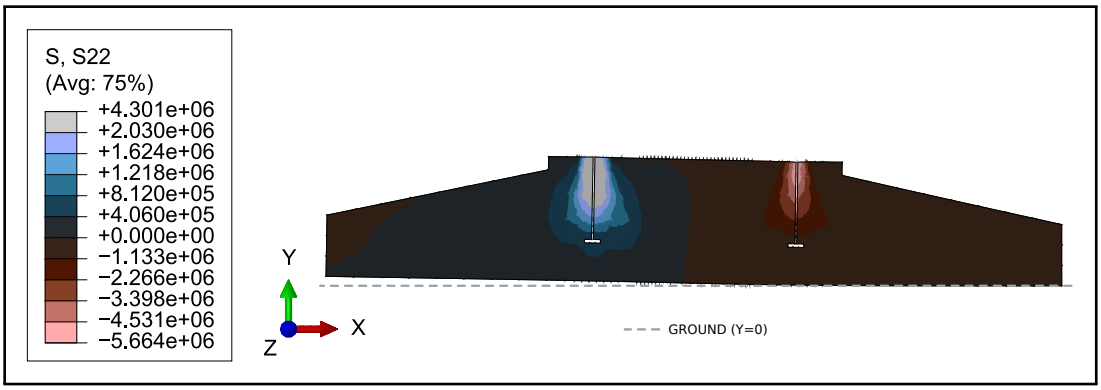

(b) σ_{yy} stresses (S22) (Pa) – refinement region.

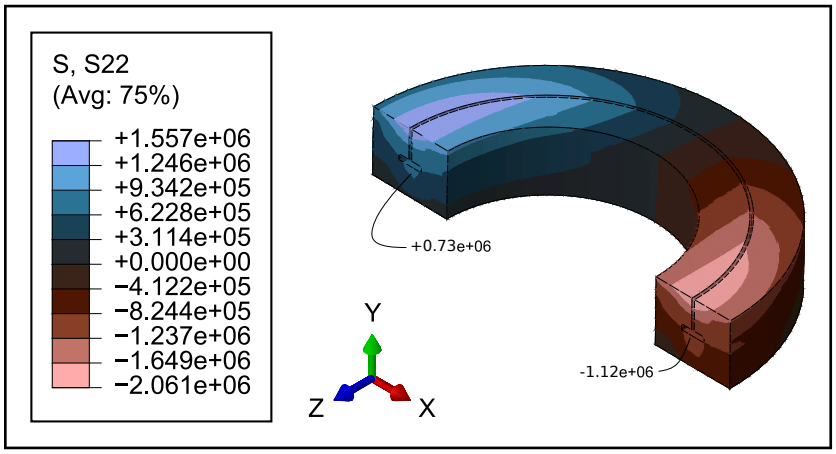

Source: The Author (2022)

The vertical displacements are mainly characterised by the foundation moving upwards in the windward direction (Figure 103), given the elastic supports that do not restrict the base under tensile activity. Accordingly, the maximum displacement value of 3.6mm is located on the foundation's edge over the X-axis, on the windward side. Additionally, the concrete base and the steel ring displace together due to the tie constraint.

The horizontal displacements present the highest values towards the top of the concrete-embedded ring set (Figure 104a). Furthermore, the detail isolating the concrete pedestal in Figure 104b shows how the region displaces a maximum of 0.97mm on its top windward area.

Figure 103 – Vertical displacements (U2) – Model I.

(a) U2 displacements (m) – perspective.

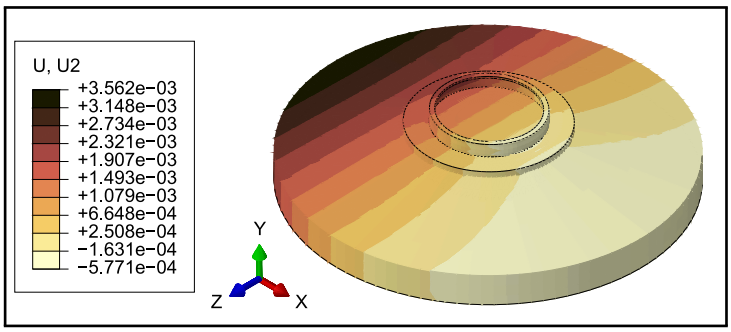

(b) U2 displacements (m) – cross-section.

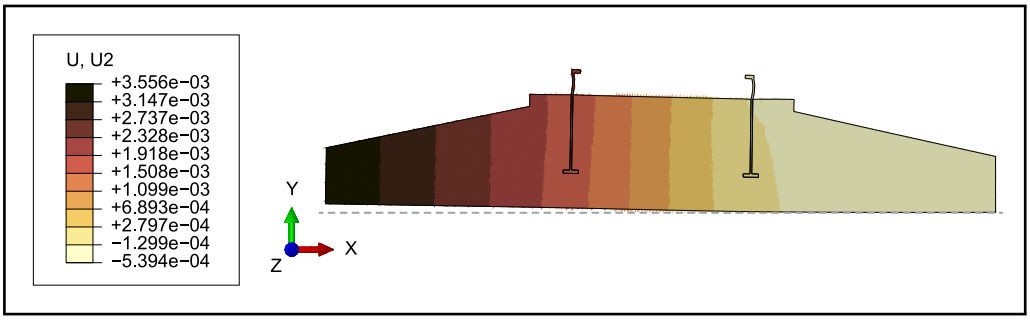

Source: The Author (2022)

Figure 104 – Horizontal displacements (U1) – Model I.

(a) U1 displacements (m) - cross-section.

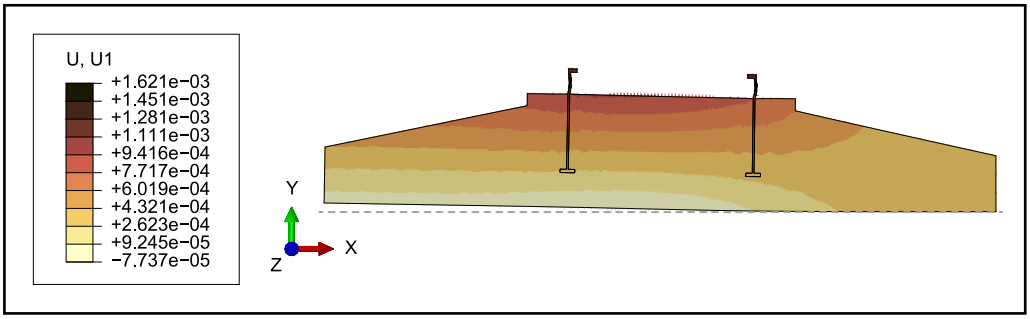

(b) U1 displacements (m) - pedestal perspective.

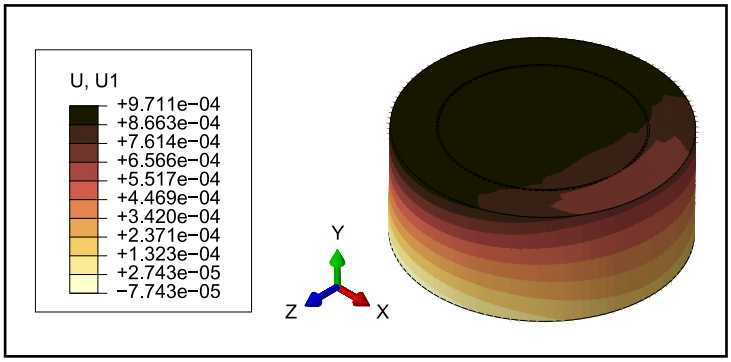

Source: The Author (2022)

4.4 MODEL II

This section presents the characteristics and results of Model II.

4.4.1 The model

Model II builds on Model I changing one feature towards enhanced assumptions and, consequently, higher complexity: the interaction between the embedded ring and the concrete base is modelled through contact, following the configurations described in Section 4.1. Figure 105 outlines the model's main specifications and, again, the mesh configuration for the model can be checked in 93.

Figure 105 – Model II.

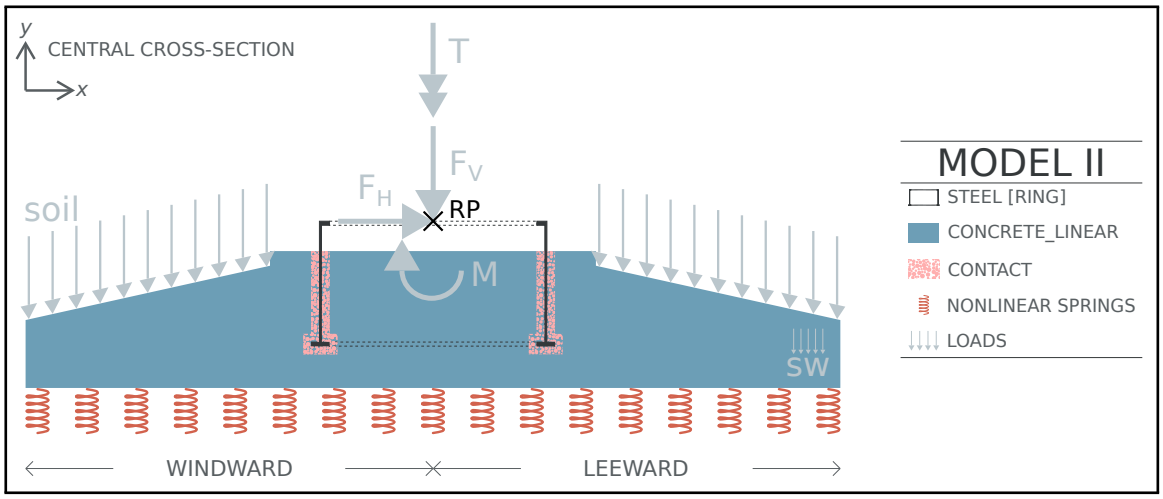

Source: The Author (2022)

4.4.2 The results

The results from Model II took 00h07m00s to be processed. Figure 106a shows the principal tensile stresses distributing from the top windward side of the foundation to the leeward bottom. Stress values exceeding f_t spread over large regions, including the windward top of the pedestal and the concrete beneath the bottom flange on both sides. Looking at Figure 106b, which presents the principal stress flow, it is noticeable how the stress concentration occurs near the flange of the embedded ring for the model in question.

Figure 107 shows the σ_{xx} (S11) stress distribution on the cross-section of Model II. Again, the flexural behaviour of the footing stands out, with regions of stress concentration on the foundation's leeward side irradiating from *Sec1_leeward*: tensile

stresses on the bottom, higher than f_t, and compressive on the top, reaching 6.45MPa. The concrete beneath the bottom flange on the windward side is also tensioned beyond the material limit.

Figure 106 – Principal stresses – Model II.

(a) Principal stresses distribution (Pa).

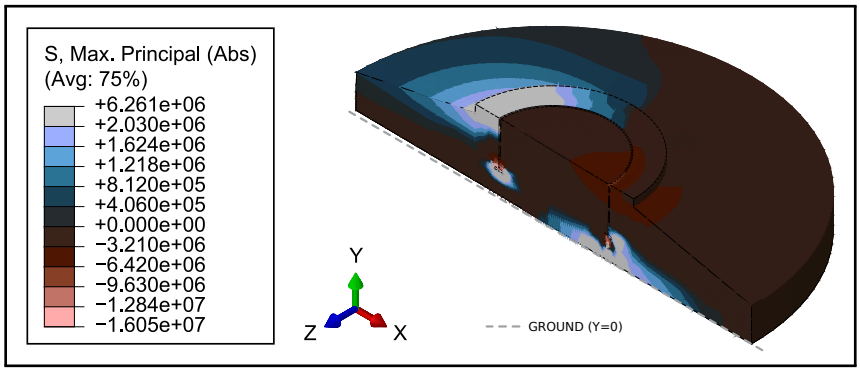

(b) Flow of principal stresses (Pa).

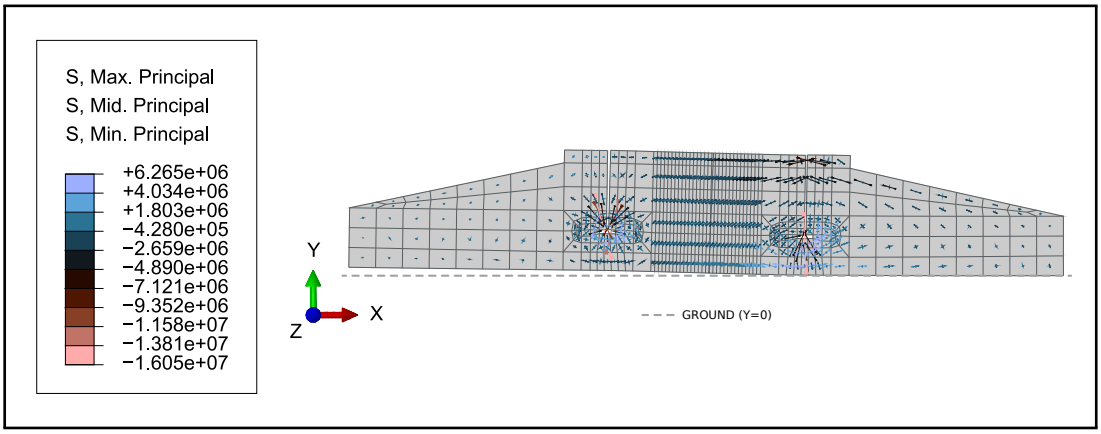

Source: The Author (2022)

Figure 107 – σ_{xx} stresses (S11) (Pa) – Model II.

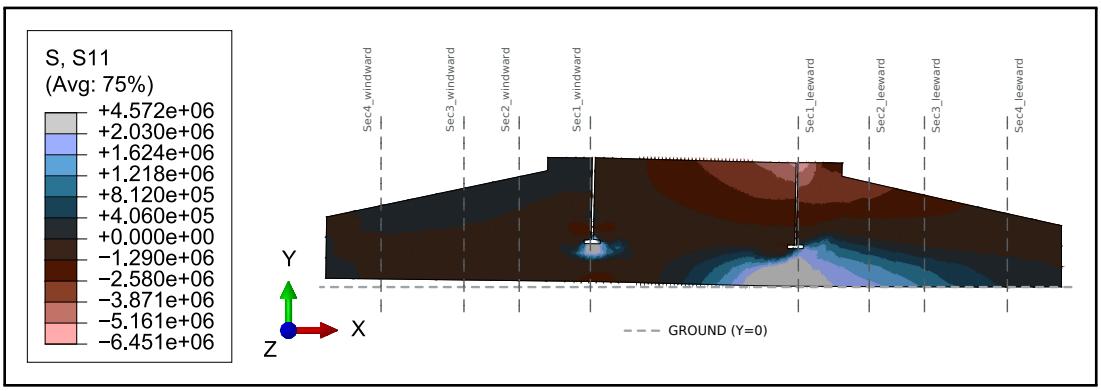

Source: The Author (2022)

Regarding the σ_{yy} (S22) stresses, high values concentrate solely near the bottom flange of the embedded ring (Figure 108a). Tensile stresses going beyond f_t irradiate

from the outside corners of the flange, while above the flange on the windward side and beneath it on the leeward side, bulbs of compressive stress with the maximum value of 14.85MPa (Figure 108b) push the concrete.

Figure 108 – σ_{yy} stresses (S22) – Model II.

(a) σ_{yy} stresses (S22) (Pa) – cross-section.

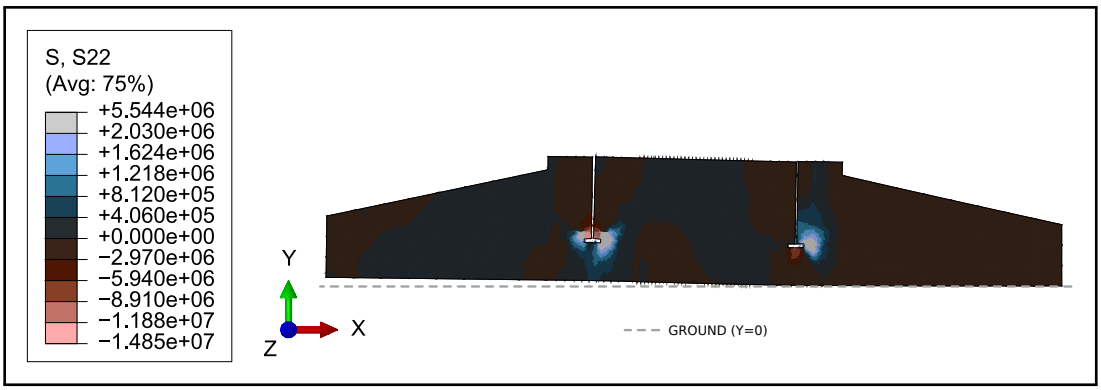

(b) σ_{yy} stresses (S22) (Pa) – refinement region.

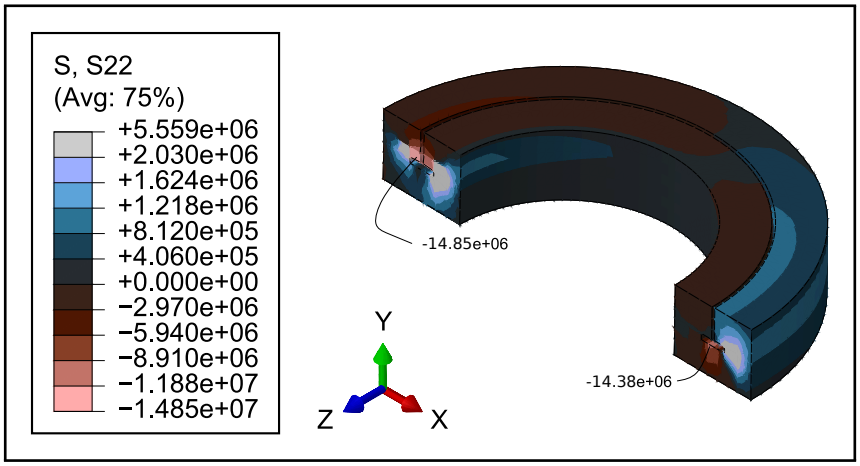

Source: The Author (2022)

Considering the foundation set, the behaviour of the vertical displacements is similar to Model I concerning their progressive increase from the leeward to the windward side (109a). However, it is noticeable that the distribution is not continuous between the concrete and the embedded ring structures (109b). The pedestal displaced according to the detail in Figure 109c, with a maximum displacement of 2.19mm above the bottom flange on the leeward side.

The horizontal displacements also present discontinuity between the structures, as can be seen in Figure 110a. Note how much the top windward region of the pedestal inside the embedded ring displaces (Figure 110b) and how it does so more than the ring wall to its left (Figure 110c), creating a gap between the structures.

Figure 109 – Vertical displacements (U2) – Model II.

(a) U2 displacements (m) – perspective.

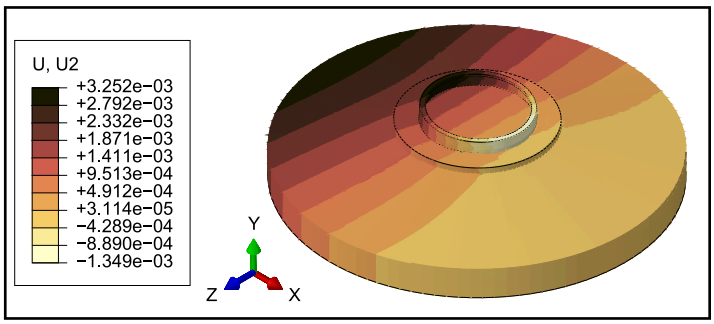

(b) U2 displacements (m) – cross-section.

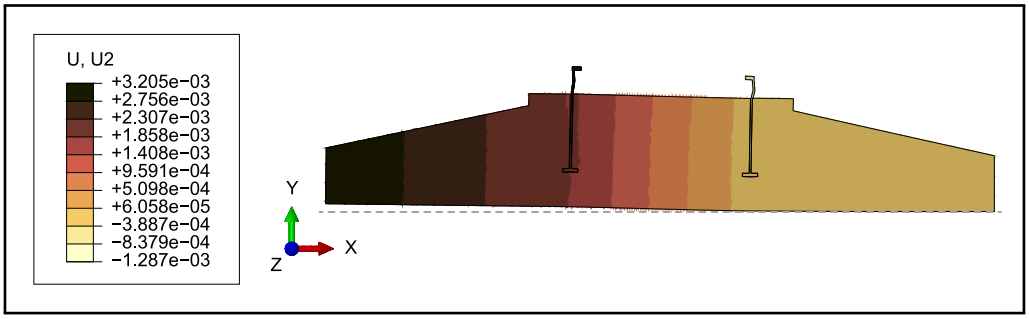

(c) U2 displacements (m) – pedestal cross-section.

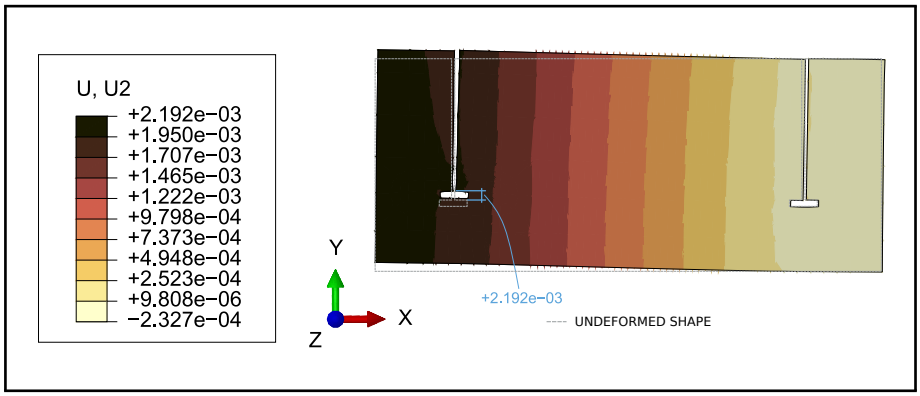

Source: The Author (2022)

Figure 110 – Horizontal displacements (U1) – Model II.

(a) U1 displacements (m) - cross-section.

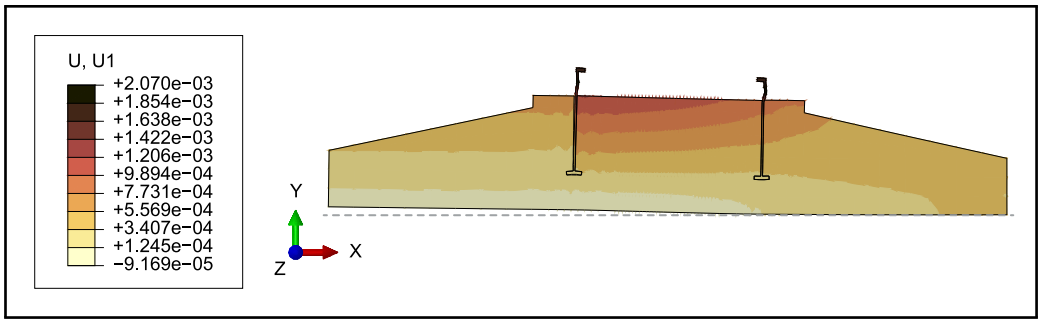

(b) U1 displacements (m) – pedestal cross-section.

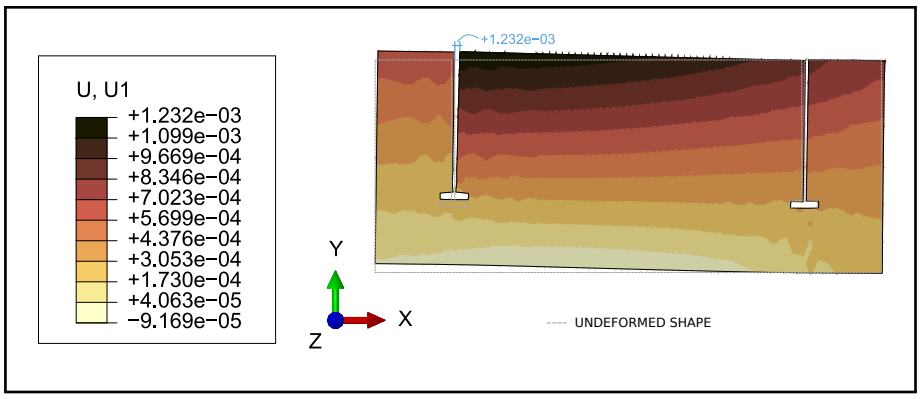

(c) U1 displacements (m) – embedded ring cross-section.

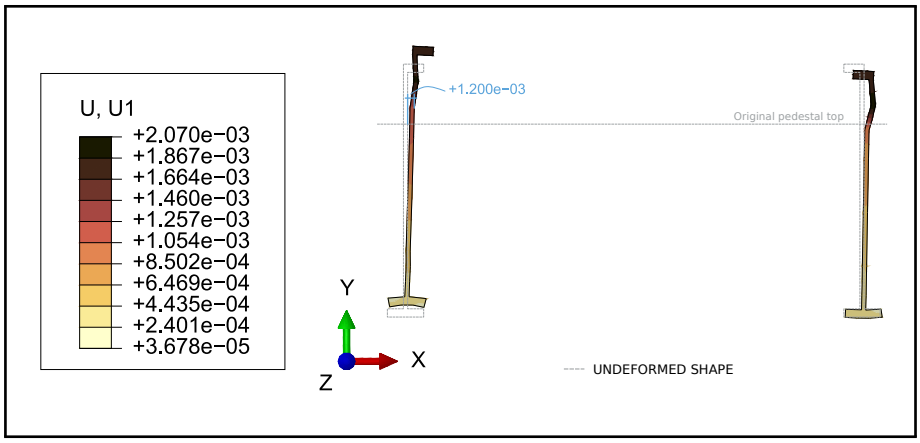

Source: The Author (2022)

4.5 MODEL III

This section presents the characteristics and results of Model III.

4.5.1 The model

Model III continues the increase in complexity, obeying the research proposal. It maintains the nonlinear springs as the boundary conditions and contact as the interaction feature from Model II. However, it updates the concrete behaviour to nonlinear, adopting the CDP material model, and includes the reinforcement steel bars (see Figure 111), both following the procedures described in Section 4.1. The resulting mesh configuration for the model is displayed in Figure 112.

Figure 111 – Model III.

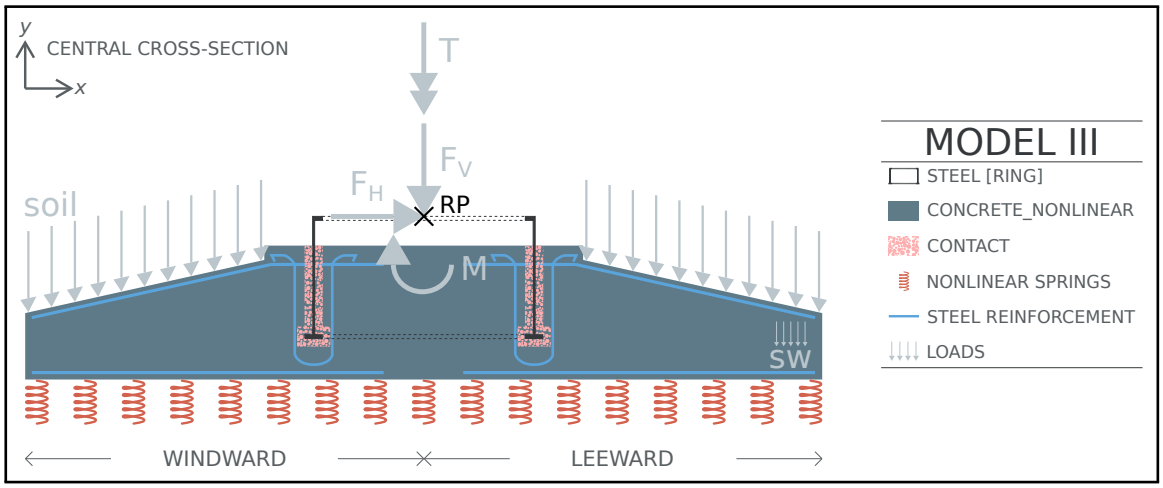

Source: The Author (2022)

Figure 112 – Mesh configuration - Model III.

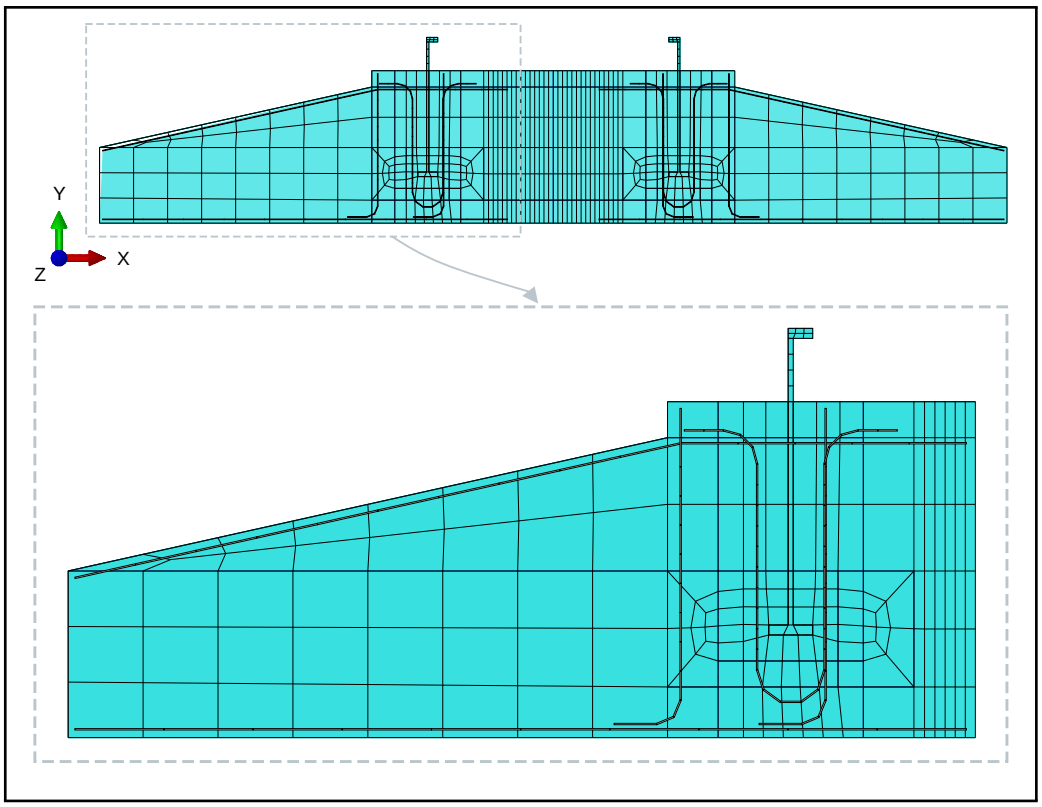

Source: The Author (2022)

4.5.2 The results

The results from Model III were processed in 06h39m42s and will be presented now. The principal stress distribution of Model III (Figure 113a) shows dissipation of tensile and compressive stresses throughout the foundation that does not follow a clear pattern except for compressive bulbs of stress above the bottom flange on the windward

side and beneath the flange on the leeward side. High compression also occurs on the top leeward region of the pedestal nearing the steel ring wall. Figure 113b portrays the stress flow and allows for verification of the model's tendency for stress localisation, mainly around the bottom flange of the ring.

Figure 113 – Principal stresses – Model III.

(a) Principal stresses distribution (Pa).

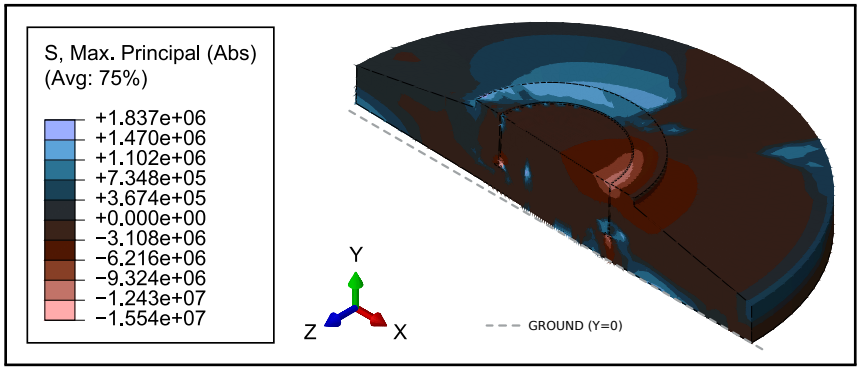

(b) Flow of principal stresses (Pa).

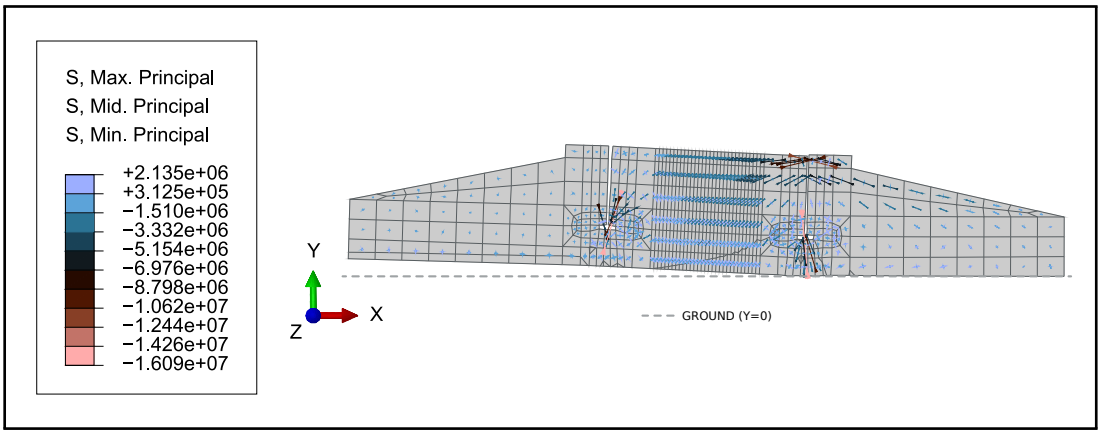

Source: The Author (2022)

The σ_{xx} (S11) stress distribution on the concrete (Figure 114a) is marked mainly by compressive stresses that spread over the cross-section. Irradiating from the top of *Sec1_leeward* is a region of high compression, exceeding 10MPa, mirrored by tensile stress localisation at the bottom of the foundation, between *Sec2_leeward* and *Sec3_leeward*, falling short of 1.33MPa. Those results, of course, are a direct consequence of the presence of reinforcement steel bars in the model. Figure 114b shows the axial stresses absorbed by the bars, with maximum values of 370MPa for tension and 40MPa for compression.

Figure 114 – σ_{xx} stresses (S11) – Model III.

(a) σ_{xx} (S11) stresses on the concrete (Pa) – cross-section.

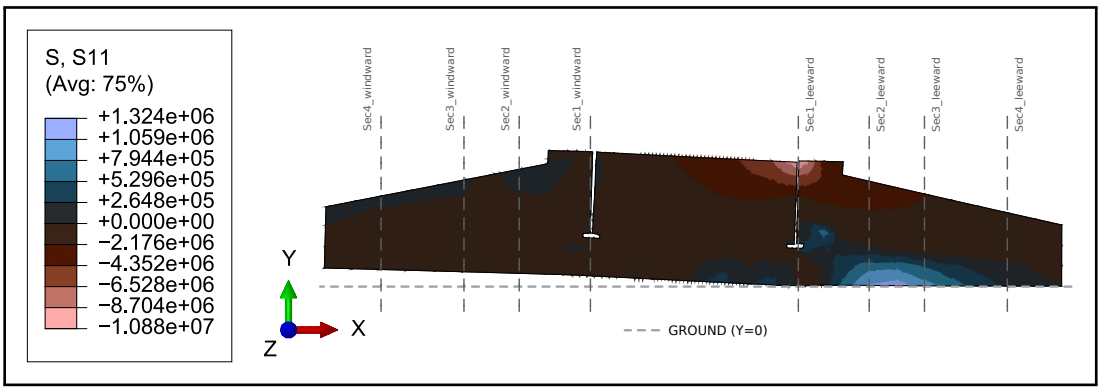

(b) σ_{xx} (S11) stresses on the steel bars (Pa) – perspective.

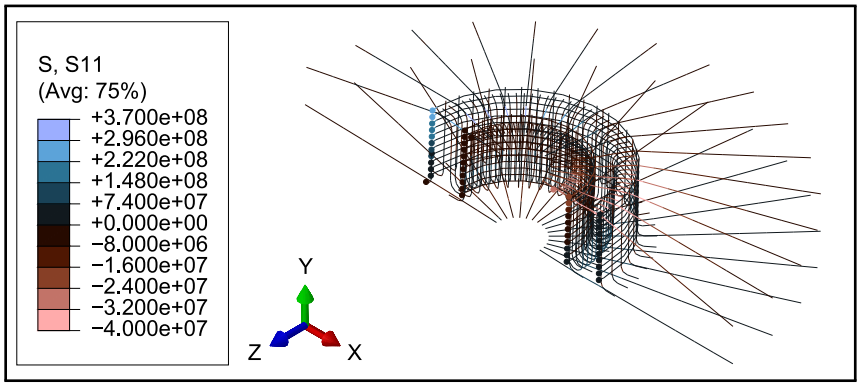

Source: The Author (2022)

For the σ_{yy} (S22) stresses, the highlight is the bulbs of compressive stress above and beneath the bottom flange of the ring, on the windward and leeward sides, respectively (Figure 115a). In addition, regions of tensile stresses develop on the corners of the flange, irradiating opposite from the compressive stresses for each side. Figure 115b details the stresses on the refinement region, improving the visualisation of the

Figure 115 – σ_{yy} stresses (S22) – Model III.

(a) σ_{yy} stresses (S22) (Pa) – cross-section.

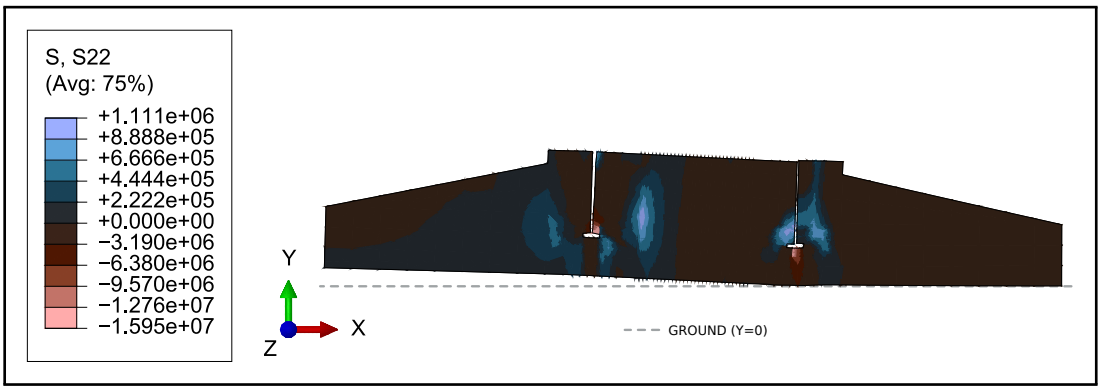

(b) σ_{yy} stresses (S22) (Pa) – refinement region.

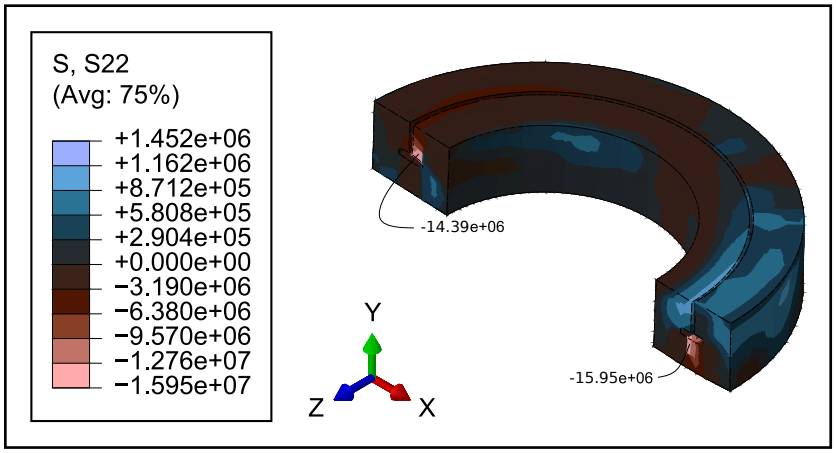

Source: The Author (2022)

distribution around the flange, whose maximum values for compression directly above and beneath the flange are 14.39MPa and 15.95MPa, respectively.

The overall distribution of vertical displacements follows the pattern of previous models, with values increasing towards the windward edge of the foundation (Figures 116a and 116b). The gap between the structures is also present. Looking at the pedestal detail in Figure 116c, we see that the maximum displacement of 4.61mm occurs on its

Figure 116 – Vertical displacements (U2) – Model III.

(a) U2 displacements (m) – perspective.

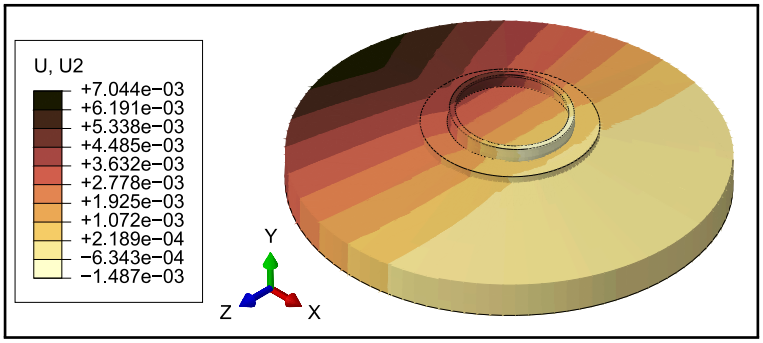

(b) U2 displacements (m) – cross-section.

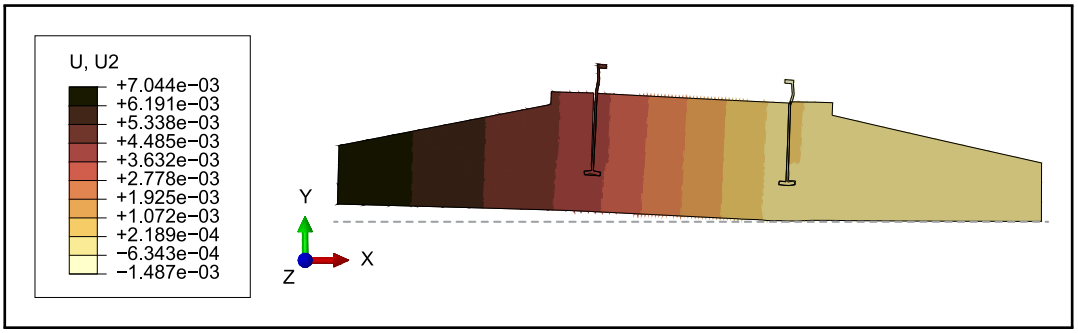

(c) U2 displacements (m) – pedestal cross-section.

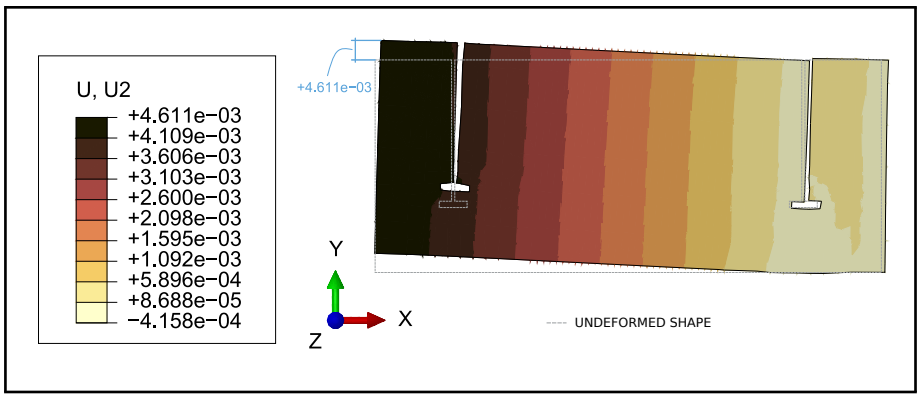

Source: The Author (2022)

top. Regarding the horizontal displacements, the gap between the structures in Figure 117a is further confirmed by the difference in their displacements presented in Figures 117b and 117c.

Figure 117 – U1 displacements (m) – Model III.

(a) Horizontal displacements (m) – cross-section.

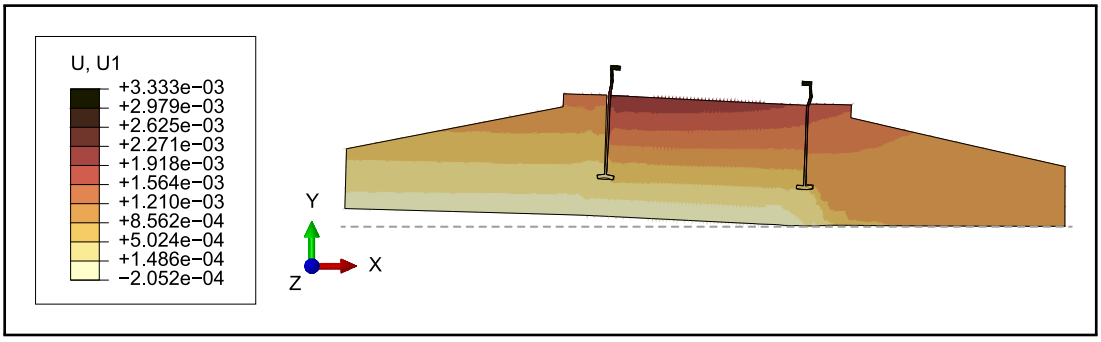

(b) U1 displacements (m) – pedestal cross-section.

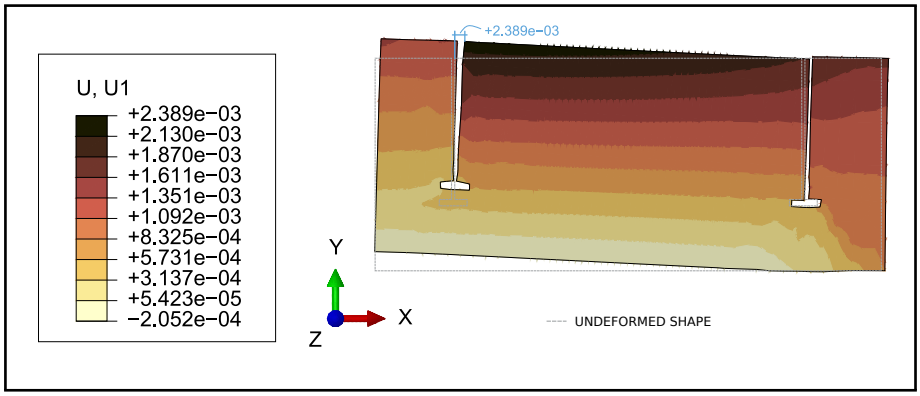

(c) U1 displacements (m) – embedded ring cross-section.

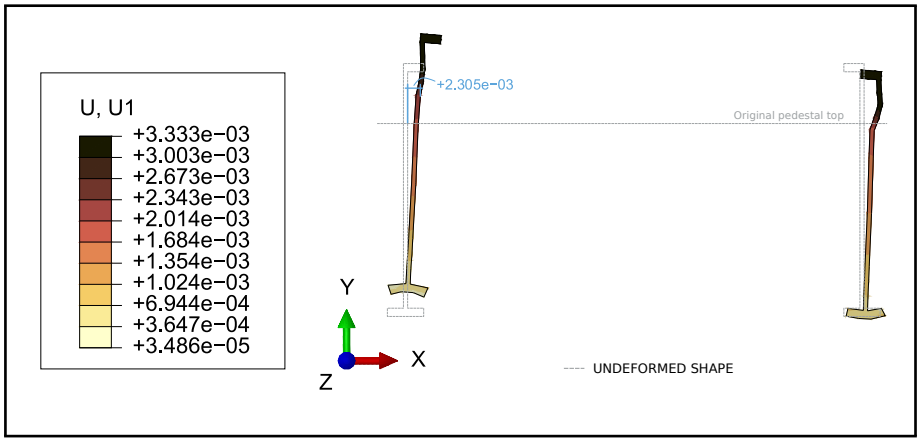

Source: The Author (2022)

Since the concrete material for Model III has a nonlinear behaviour, information on material degradation is expected from the analysis. The CDP model, however, does not allow for cracks to be explicitly output. Nonetheless, *Abaqus* provides two kinds of field output results that can graphically represent the loss of strength and crack patterns. Firstly, the DAMAGET variable, in Figure 118a, presents the foundation behaviour in terms of the tensile damage parameter (d_t), with 1 representing a complete loss of strength. The figure then shows the distribution and degree of material damage, with concrete degraded to levels of d_t=0.98 around the bottom flange of the embedded ring. Then, Figure 118b portrays the assumed crack pattern of the simulation through the symbol plot of the maximum principal plastic strains. The reasoning is that cracking is assumed to initiate at the points where the tensile equivalent plastic strain, ε_t^p, and the maximum principal plastic strain are both positive (LUBLINER et al., 1989). Since the *PE, max principal* is normal to the crack plane, it determines the crack directions.

Figure 118 – Concrete damage – Model III.

(a) DAMAGET – cross-section.

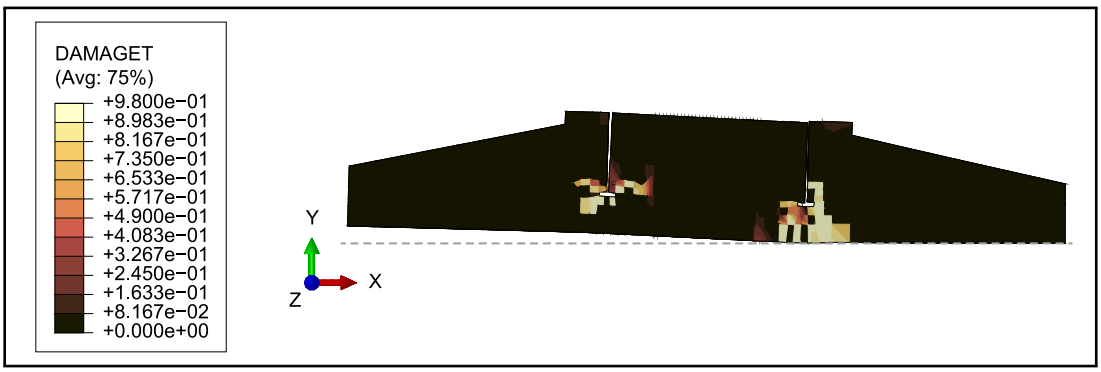

(b) PE, max principal – crack directions.

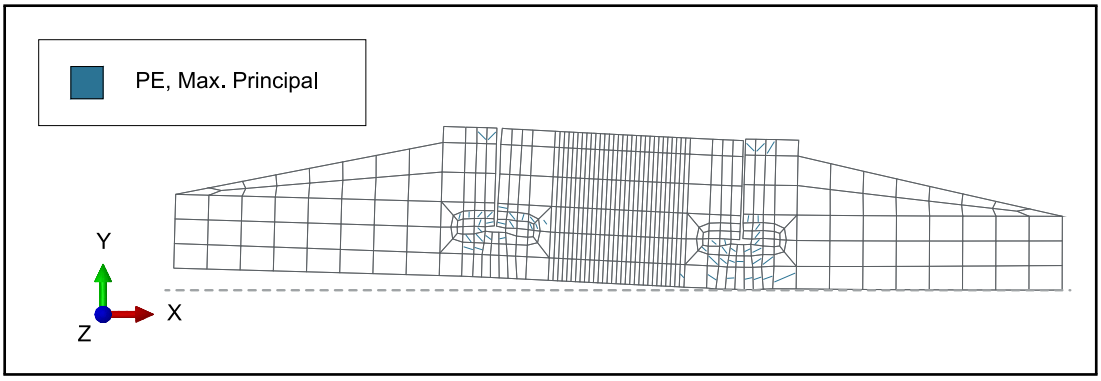

Source: The Author (2022)

4.6 DISCUSSION

The results presented in the previous sections will now be discussed. Firstly, it is clear that they are aligned with the literature findings about the correlation between the wind direction and the damage-incurring displacements of the embedded ring (CURRIE et al., 2015; BAI et al., 2017b). That is verified by the pattern of the distribution of the efforts directly relatable to the fixed wind direction considered and reproduced by $\boldsymbol{M}$ and $\boldsymbol{F_H}$. Now, the results will be analysed under the optics of what makes each model differ and advance on the previous: the boundary conditions, the form of interaction between the embedded ring and the concrete, and the concrete's nonlinear behaviour aided by the reinforcement steel bars.

Starting with the supports, we saw how the $\boldsymbol{\sigma_{xx}}$ (S11) stress distribution changed significantly from Model 0, consisting of rigid supports, to Model I, where the nonlinear springs started being used in the models. In Model 0, the footing presented no flexural behaviour, with sections fully tensioned or compressed up to values of 0.41MPa and 0.89MPa, respectively. In contrast, Model I presented a flexed footing with the tensile stress region crossing downwards from windward to leeward in a 45° diagonal across the pedestal. The stress values on the footing go above $\boldsymbol{f_t}$ for tension and 2.95MPa for compression. The restriction to movement applied to the bottom of the foundation on Model 0 in the form of the rigid supports prevented the expected bending behaviour of the sections and, if adopted, would require no longitudinal reinforcement bars due to the low-stress values. Therefore, the use of the nonlinear springs proved a better assumption.

Attending the discussion of how the interaction type influences the models'

results, we will start by looking at the σ_{yy} (S22) stress distributions. Figure 119 shows the pedestal behaviour regarding the vertical stress for the four models, considering the same stress range. Models 0 and I, built with tie constraint, present high-stress values that irradiate from the top of the concrete pedestal, near the steel ring, towards the bottom. Models II and III, on the other hand, built with contact, concentrate stress closer to the bottom flange of the ring. That agrees with the load-transfer mechanism of the embedded-ring foundations, discussed in Chapter 2. On the contrary, the situation in models 0 and I indicates a load transfer occurring on the top of the ring-pedestal junction.

Figure 119 – Comparison of σ_{yy} (S22) stress distributions (Pa).

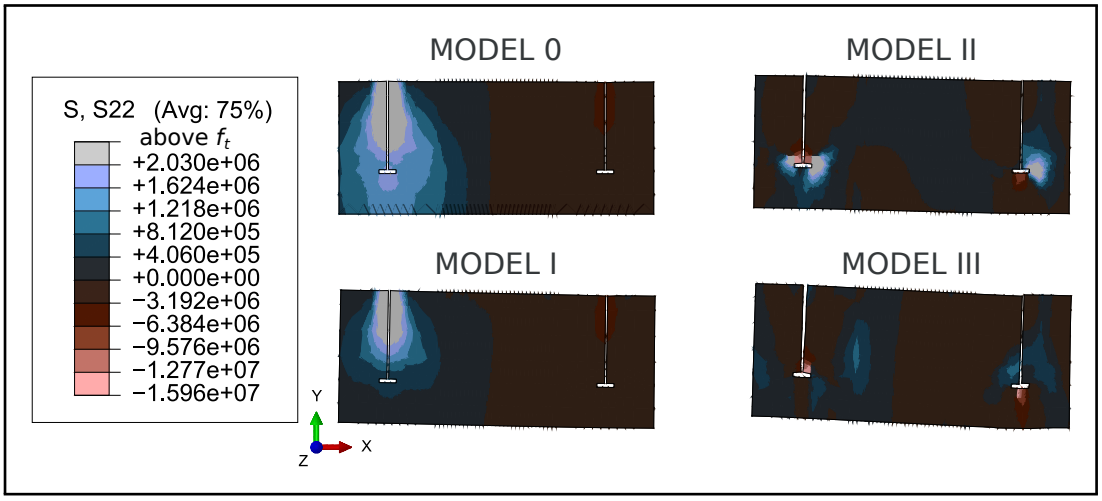

Source: The Author (2022)

The displacements' results confirm that the tie constraint does not allow the model to reproduce the problems found in the field. By preventing the relative movement between the structures, true to the assumption of a perfect bond, the ring cannot displace inside the concrete, which researchers have established as the leading cause of degradation in the concrete around the bottom flange. The results presented for models 0 and I (Figures 97, 98, 103 and 104), along with these models' total displacements in Figure 120, show the continuity in the movement since the concrete base and the ring displace together. Meanwhile, the contact interaction allows for relatively independent movement, as seen from models' II and III results (Figures 109, 110, 116 and 117) and further detailed in Figure 120. Table 26 brings the maximum displacements and gaps between the ring and the concrete base for models II and III for comparison: the nonlinear model presents values up to 62% higher.

Figure 120 – Comparison of total displacements (m).

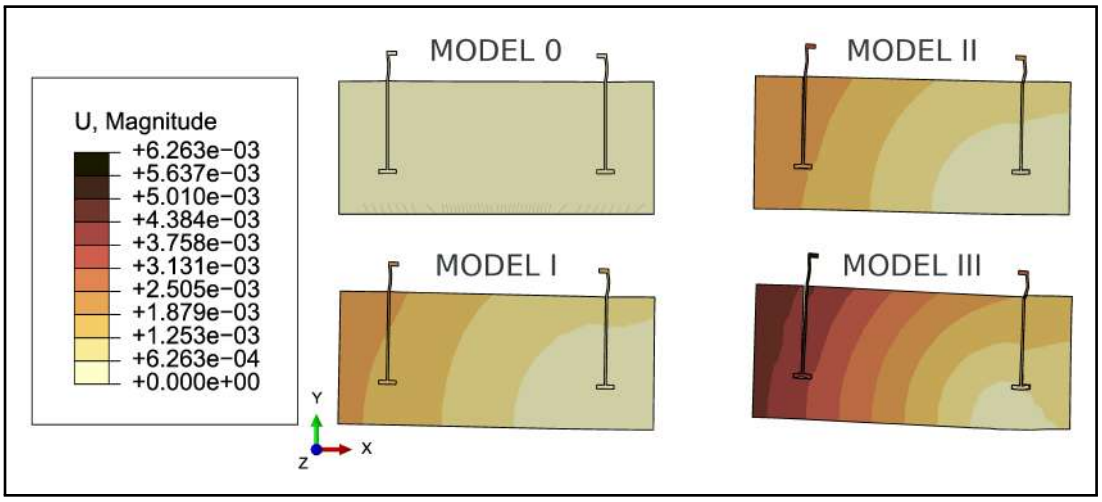

Source: The Author (2022)

Table 26 – Maximum displacements - Models II and III.

	Model II	**Model III**	$\frac{U_{Model\_III} - U_{Model\_II}}{U_{Model\ III}}$
U1 (mm)	1.200	2.389	50%
U1 - *gap* (mm)	0.032	0.084	62%
U2 (mm)	2.192	4.611	52%

Source: The Author (2022)

This relative displacement found in models II and III is related to the design concept of the embedded-ring foundation, as discussed in Section 2.2.2. Gaps between the ring and the concrete were highly discussed, together with the consequent stress concentration in the concrete that resulted in concrete degradation. The simulation results regarding the stress distribution agree with these findings: the concrete was significantly compressed above the flange on the windward side and beneath it on the leeward side. Figure 121 focuses on the σ_{yy} (S22) distribution around the flange for these models, where the only differences were the concrete material model and the presence of steel reinforcement bars. In Model II, the concrete around the flange is compressed to a maximum value of 14.84MPa, whereas Model III presents compressive areas that reach a value just slightly higher: 15.95MPa. Also, Model II has tensile stresses above the material limit irradiating from the flange, while Model III presented somewhat similar tensile behaviour but with lower tensile values, not exceeding 1MPa for the region.

Figure 121 – Comparison of σ_{yy} (S22) stresses around the flange (Pa).

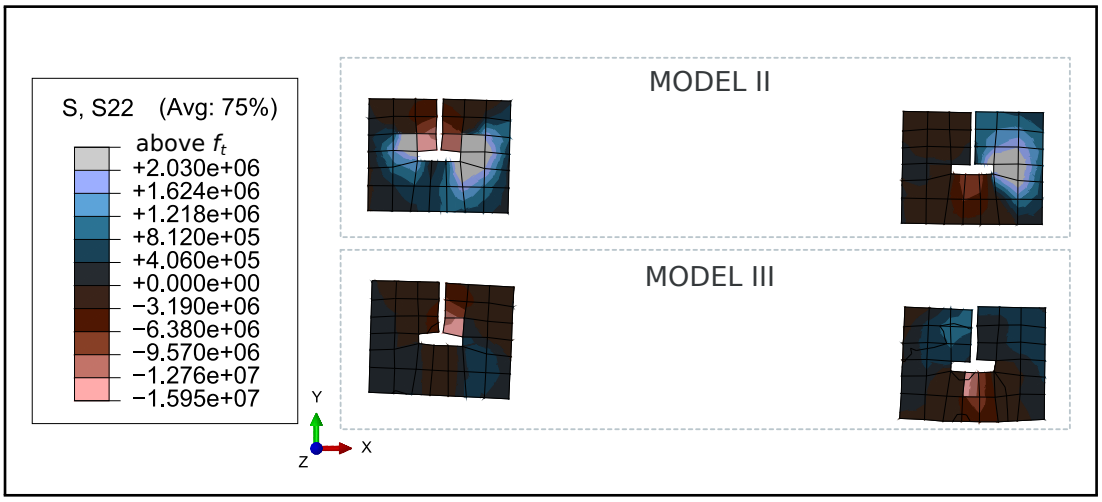

Source: The Author (2022)

The comprehension regarding the differences and similarities between the models can be expanded if the σ_{yy} (S22) stress results are now collected for two different depths across the foundation and submitted to a joint analysis of models II and III. Figure 122 displays those results, where a general data comparison implies a likeness regarding the models' structural responses. The results are practically equal from the embedded ring's outskirts towards the border of the foundation. The disparity in outcomes appears only in the regions approaching the ring and confined by it: the regions susceptible to stress concentrations.

Figure 122 – σ_{yy} (S22) sectional stresses analysis – Models II and III.

(a) Section 1.

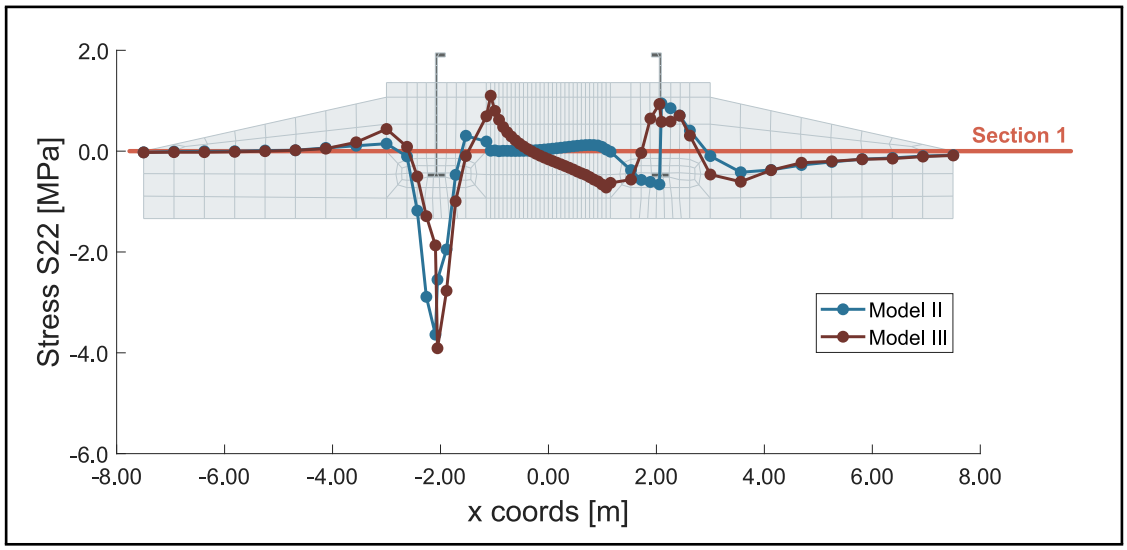

(b) Section 2.

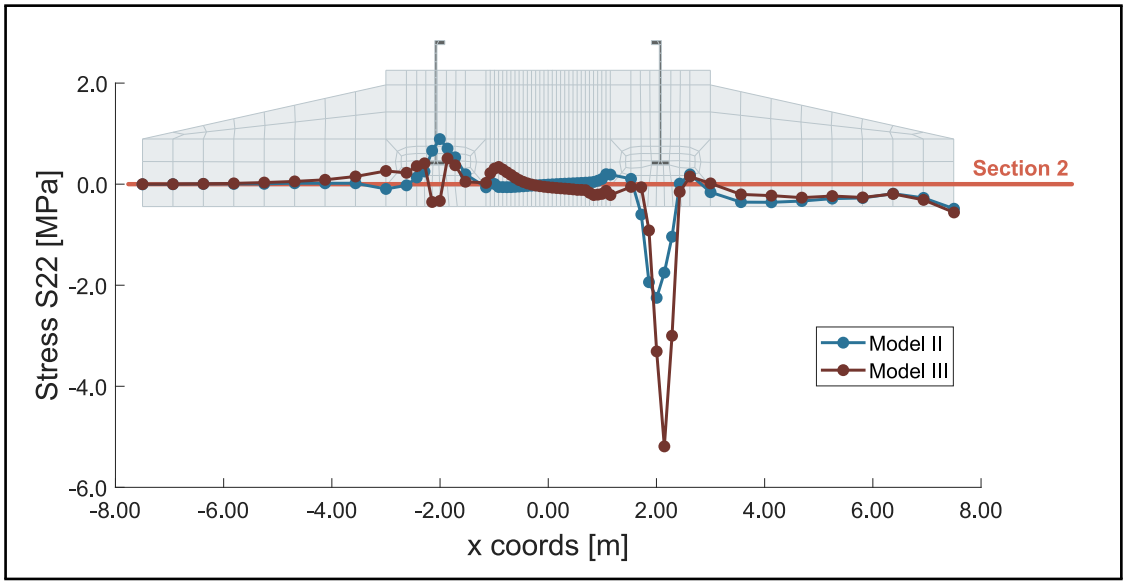

Source: The Author (2022)

Looking at the top-most section (*Section 1*) results in Figure 122a, we see that both models are congruent even concerning the maximum values of tensile and compressive stresses around the bottom flange while strongly differing in the region in-between. While Model II presents a stress distribution with slight variation ($\approx$ 0MPa in compression to 0.12MPa in tension), Model III varies more significantly, from 1.1MPa in tension to 0.72MPa in compression. The results from the bottommost section (*Section 2*, Figure 122b), which crosses the foundation below the flange, also present compatibility between the models for the areas not prone to stress concentrations. Neighbouring the flange, however, the data diverge: on the windward side, Model II captures tensile stresses of up to 0.9MPa, versus low compressive stresses of 0.35MPa captured by Model III; on the leeward side, although both models capture compressive behaviour, Model II reports a maximum value of 2.25MPa against 5.19MPa reported by Model III.

Advancing on this focused analysis of models II and III, we compare the principal stress results developed in Model II against the principal plastic strains in Model III (Figure 123). Model II indicates areas likely to suffer plastification (where the tensile stresses reached above the material limit, Figure 123a) closely related to the plastic regions in Model III (Figure 123b). However, despite this relatively compatible indication of behaviour, a detailed understanding of the material disintegration could only be studied with Model III. Figures 118a and 118b, which plotted the resulting damage parameter and crack pattern on the concrete, respectively, informed the degree of

Figure 123 – Indication of damage - Models II and III.

(a) Principal stresses distribution (Pa) - Model II.

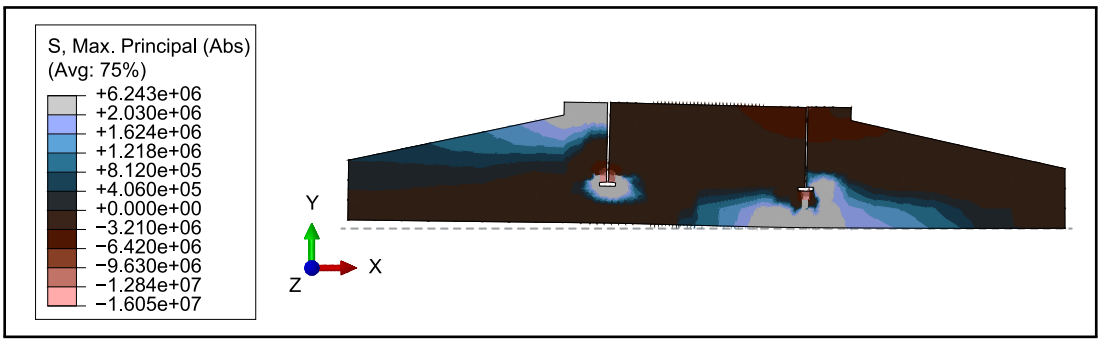

(b) Maximum principal plastic strains – Model III.

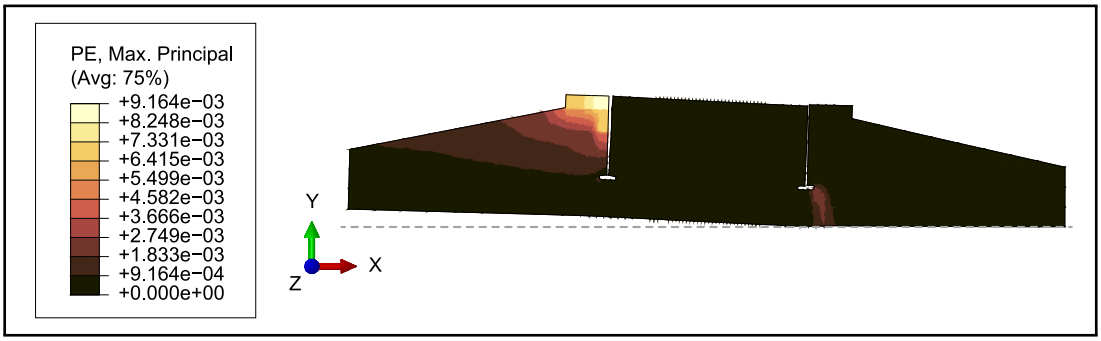

Source: The Author (2022)

degradation, affected regions, and crack directions of the foundation. A significant loss of strength to the concrete surrounding the bottom flange of the ring was identified in agreement with the literature-reported findings regarding the damages inflicting embedded-ring foundations for wind turbines.

The nonlinear analysis also predicts how much applied load the structure can withstand without the concrete being driven past the linear elastic regime. For the loads present in the model (Section 4.1.1) and the conditions of Model III, Figure 124 displays the progress of the damage in the foundation regarding the load percentage. First, damage starts to form in the concrete for 28% of the acting forces, with d_t=0.13.

Figure 124 – Progression of damage - Model III.

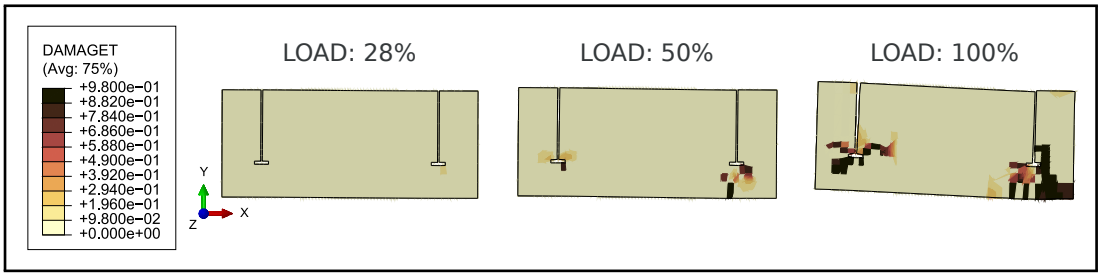

Source: The Author (2022)

Then, at only 50% of the applied loads, the damaged regions expand, and some spots already present an almost complete loss of concrete strength: d_t=0.98. Finally, the resulting state of the foundation under 100% of the loads is a large portion of concrete disintegrated around the bottom flange.

At last, the longitudinal steel reinforcement bars that cross the steel ring are substantial for the analysis. Figure 125 shows in detail the crossing region, where the axial stresses on the bars were the highest due to the relative displacement of the steel ring concerning the concrete. According to the reports from the literature discussed in the second Chapter, Section 2.2.2, bars were found sheared in this region, given the large separations between the structures. Even though the bars in the simulation have not sheared, they still follow the strength demand pattern reported.

Figure 125 – Detail of strained reinforcement bars.

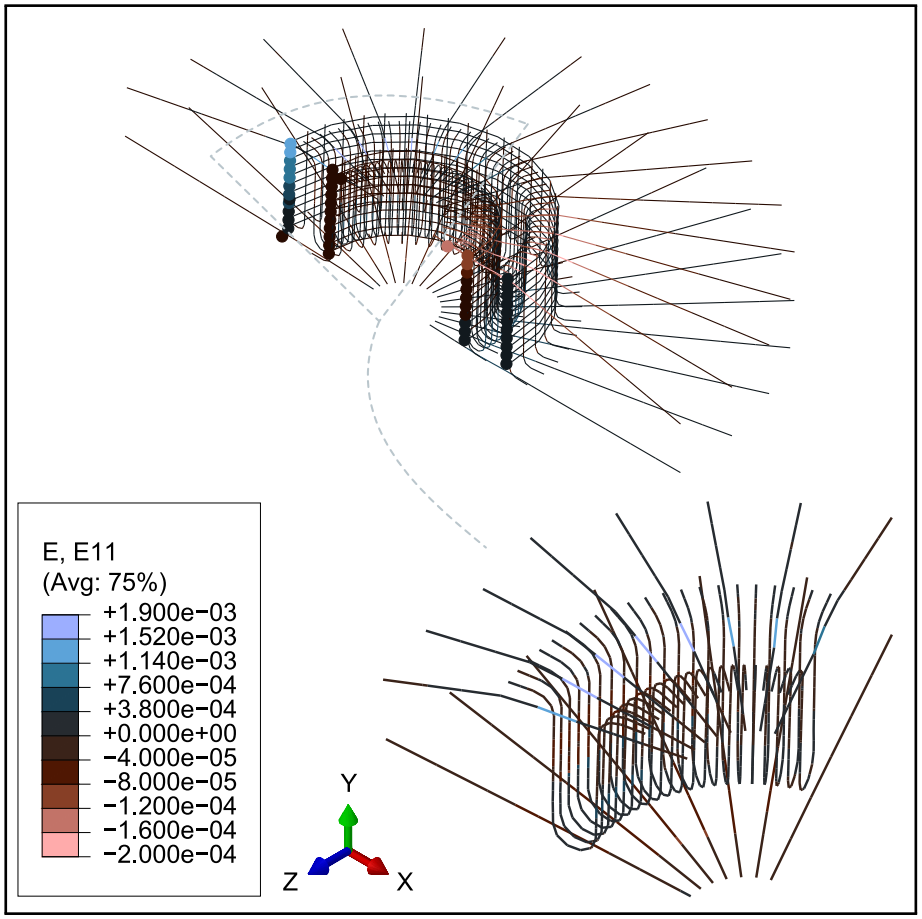

Source: The Author (2022)

5 CONCLUSION

This final chapter synthesizes the discussion in Section 4.6 and presents recommendations for future work on embedded-ring foundations' structural behaviour.

5.1 FINAL REMARKS

When building finite element models to study the structural behaviour of wind turbine embedded-ring foundations, the level of approximation of the model, regarding the assumptions considered for it, must be compatible with its objective. This study presented the development and the responses of four models with differing numerical assumptions so that it would be possible to understand how each assumption affected the structural behaviour and which model better fitted the purpose of investigating the concrete close to the bottom flange of the embedded ring, reported to have deteriorated in foundations of the kind.

The findings showed first that the assumption of rigid supports impeding the foundation's bottom surface displacements prevented the footing's expected bending behaviour. The low stress values paired with the full compression or tension of the sections used to dimension the reinforcement led to significantly low bending moments, culminating in the lack of need for steel. That was considered a problem for the research aim, so the assumption of elastic supports that only respond to compression is the only one defined as correct.

The same is true for considering contact between the structures since the assumption of a perfect bond between the concrete and the embedded ring, in the form of tie constraint, does not allow the steel ring to dislocate inside the concrete. Given that the embedded ring's displacement is painted as one of the leading causes of the concrete degradation inside the foundation, a model that cannot reproduce this problem is not fit for the research's objective.

Lastly, the model needs to have a nonlinear concrete behaviour to model the concrete's disintegration. Using the CDP paired with the steel reinforcement makes it possible to more accurately study the consequences of loading on the structure, including the concrete's loss of strength and crack pattern. That way, targeted enhancements to the design can be made to tackle the spots of fragility.

Of course, we have seen that the higher the complexity of the model, the higher

the cost to compute it. The times necessary to process the analyses were gathered in Table 27, and what stands out is how much longer Model III took to complete than the other models: models 0, I and II were around 99% to 98% faster than Model III. This significantly higher cost comes from the concrete nonlinearity, which, as seen, inserts a factor of high iterative activity into the mathematics, requiring a much longer simulation to solve the finite element system of equations. The author considers this cost valid for the research aim but should be reconsidered if the objective is not too localised. For example, Model II has a set of assumptions that could suffice the understanding of the foundation's general structural behaviour.

Table 27 – Processing time.

Model	**Processing time (hh:mm:ss) -** T	$\frac{T_{Model}}{T_{ModelIII}}$
Model 0	00:01:33	0.39%
Model I	00:01:42	0.43%
Model II	00:07:00	1.75%
Model III	06:39:42	100%

Source: The Author (2022)

5.2 RECOMMENDATIONS FOR FUTURE WORK

This work could be continued to develop further studies about the structural behaviour of the embedded-ring foundation. Following are some recommendations the author considers relevant to study.

- Structural enhancement suggestions of Zhou, Kong e Dow (2015) on Model III, such as welding shear studs to the wall of the ring, using fibre reinforced concrete, and increasing the area of the bottom flange;
- Structural effects of different geometries for the foundation;
- Different soil-structure interaction models.

REFERENCES

ABEEólica. *INFOWIND 21. NOVEMBER 20 - 2021*. [S.l.], 2021. Disponível em: <http://abeeolica.org.br/wp-content/uploads/2021/11/2021_11_InfoWind23.pdf>. Citado na página 16.

ABNT. *ABNT NBR 6118 Projeto de estruturas de concreto - Procedimento*. 2014. Disponível em: <www.abnt.org.br>. Citado 2 vezes nas páginas 51 and 56.

ADEEB, S. *Introduction to Solid Mechanics*. Engineering at Alberta, 2020. Disponível em: <https://engcourses-uofa.ca/books/introduction-to-solid-mechanics/stress/stress-based-failure-criteria/>. Citado na página 59.

ALONSO, U. R. *Exercícios de fundações*. 3. ed. São Paulo: Blucher, 2019. ISBN 9788521213840. Disponível em: <https://books.google.com/books/about/Exerc%C3%ADcios_de_funda%C3%A7%C3%B5es.html?hl=pt-BR&id=QwC5DwAAQBAJ>. Citado na página 25.

Anyang Longteng Heat Treatment Material Co. *Overview of Wind Turbine Anchor Cage Install Process*. –. Disponível em: <https://www.high-strength-steel.com/news/overview-of-wind-turbine-anchor-cage-install-process>. Citado na página 27.

ASSAN, A. E. *Resistência dos materiais*. Campinas: Editora da Unicamp, 2010. v. 1. Citado na página 58.

BAI, X. et al. Modelling fatigue degradation of the compressive zone of concrete in onshore wind turbine foundations. *Construction and Building Materials*, Elsevier Ltd, v. 132, p. 425–437, 2 2017. ISSN 09500618. Citado 4 vezes nas páginas 7, 35, 36, and 101.

BAI, X. et al. Structural condition monitoring of wind turbine foundations. In: *Proceedings of Institution of Civil Engineers: Energy*. [S.l.]: ICE Publishing, 2017. v. 170, n. 3, p. 116–134. ISSN 17514231. Citado 4 vezes nas páginas 7, 31, 32, and 133.

BASTOS, P. S. *Lecture Notes: FLEXÃO NORMAL SIMPLES - VIGAS*. 2020. Disponível em: <wwwp.feb.unesp.br/pbastos>. Citado na página 52.

BFT International. *Precast concrete elements for the energy transition – Part I: wind power plants*. 2017. Disponível em: <https://www.bft-international.com/en/artikel/bft_Precast_concrete_elements_for_the_energy_transition_Part_I_wind_power_2815303.html>. Citado na página 23.

BORST, R. D. et al. *NON-LINEAR FINITE ELEMENT ANALYSIS OF SOLIDS AND STRUCTURES*. 2. ed. [S.l.]: Wiley, 2012. ISBN 9780470666449. Citado 4 vezes nas páginas 59, 61, 62, and 63.

British Petroleum. *Statistical Review of World Energy 2021 | 70th edition*. [S.l.], 2021. Disponível em: <https://www.bp.com/content/dam/bp/business-sites/en/global/corporate/pdfs/energy-economics/statistical-review/bp-stats-review-2021-full-report.pdf>. Citado na página 15.

BSI. *Eurocode 2: Design of Concrete Structures: Part 1-1: General Rules and Rules for Buildings*. London: CEN, 2004. Citado na página 69.

CHANDRA, S. *Lecture Notes: Modelling of Soil behaviour*. 2014. Disponível em: <http://home.iitk.ac.in/~peeyush/mth426/Lec4_schandra.pdf>. Citado na página 45.

CHEN, J. et al. Strengthening mechanism of studs for embedded-ring foundation of wind turbine tower. *Energies*, MDPI AG, v. 14, n. 3, 2 2021. ISSN 19961073. Citado 6 vezes nas páginas 29, 38, 39, 72, 101, and 104.

CHEN, J.; XU, Y.; LI, J. Numerical investigation of the strengthening method by circumferential prestressing to improve the fatigue life of embedded-ring concrete foundation for onshore wind turbine tower. *Energies*, MDPI AG, v. 13, n. 3, 2020. ISSN 19961073. Citado 5 vezes nas páginas 30, 37, 38, 72, and 101.

CRAMERI, F. *Scientific colour maps*. 2018. Disponível em: <https://www.fabiocrameri.ch/colourmaps/>. Citado na página 92.

CTE Wind International. *The Bolt Cage Design*. –. Disponível em: <https://www.cte-wind.com/solution/anchor-cage-design/>. Citado na página 27.

CURRIE, M. et al. Structural integrity monitoring of onshore wind turbine concrete foundations. *Renewable Energy*, Elsevier Ltd, v. 83, p. 1131–1138, 11 2015. ISSN 18790682. Citado 6 vezes nas páginas 7, 27, 28, 30, 31, and 133.

CURRIE, M. et al. Structural health monitoring system for wind turbine foundations. In: . [s.n.], 2013. Disponível em: <https://www.researchgate.net/publication/265403478>. Citado 5 vezes nas páginas 7, 28, 29, 30, and 31.

DAY, R. W. *Foundation Engineering Handbook. Design and Construction with the 2006 International Building Code*. [S.l.: s.n.], 2005. ISBN 978-0071447690. Citado 2 vezes nas páginas 25 and 49.

DNV GL. *DNVGL-ST-0126: Support Structures for Wind Turbines*. DNV GL, 2016. Disponível em: <www.dnvgl.com.> Citado na página 23.

DOURADO, T. T.; AGUIAR, W. B. D.; RIBEIRO, P. M. V. Finite element models for analysis of structural integrity of onshore wind turbine foundations with embedded rings submitted to static and dynamic loads. In: *Cilamce*. [S.l.: s.n.], 2020. Citado na página 33.

EARIJ, A. et al. Nonlinear three–dimensional finite–element modelling of reinforced–concrete beams: Computational challenges and experimental validation. *Engineering Failure Analysis*, Elsevier Ltd, v. 82, p. 92–115, 12 2017. ISSN 13506307. Citado 4 vezes nas páginas 63, 70, 71, and 95.

Ferhan Öztürk. *FINITE ELEMENT MODELLING OF TUBULAR BOLTED CONNECTION OF A LATTICE WIND TOWER FOR FATIGUE ASSESSMENT*. 2016. Disponível em: <https://www.researchgate.net/publication/292610311>. Citado na página 24.

Francesco Miceli. *Embedded ring foundations*. 2012. Disponível em: <https://www.wind-watch.org/documents/embedded-ring-foundations/>. Citado na página 27.

GODOI, M. *Energia eólica chega a 18 GW de capacidade instalada no Brasil*. 2021. Disponível em: <https://www.canalenergia.com.br/noticias/53163929/energia-eolica-chega-a-18-gw-de-capacidade-instalada-no-brasil>. Citado na página 16.

GWEC. *Global Wind Report 2021*. [S.l.], 2021. Disponível em: <https://gwec.net/global-wind-report-2021/>. Citado 2 vezes nas páginas 15 and 16.

HASSANZADEH, M. *Cracks in onshore wind power foundations Causes and consequences Elforsk rapport 11:56*. [S.l.], 2012. Citado 8 vezes nas páginas 18, 22, 23, 26, 27, 28, 29, and 57.

HAU, E. *Wind turbines: Fundamentals, technologies, application, economics*. [S.l.]: Springer-Verlag Berlin Heidelberg, 2013. v. 9783642271519. 1–879 p. ISBN 9783642271519. Citado 4 vezes nas páginas 21, 22, 24, and 25.

HE, M. et al. Field experimental study on the retrofit of cracked onshore wind turbine foundations using externally prestressed anchor bolts. *Structural Concrete*, Wiley-Blackwell, v. 19, n. 3, p. 864–875, 6 2018. ISSN 17517648. Citado 5 vezes nas páginas 28, 29, 30, 36, and 37.

HE, M. et al. Structural monitoring of an onshore wind turbine foundation using strain sensors. *Structure and Infrastructure Engineering*, Taylor and Francis Ltd., 2019. ISSN 17448980. Citado 7 vezes nas páginas 7, 18, 28, 29, 35, 36, and 104.

HEMANTH, R. et al. Performance Evaluation of Finite Elements for Analysis of Advanced Hybrid Laminates. 2010. Citado na página 101.

IEA. *Electricity production*. [S.l.], 2019. Disponível em: <https://www.iea.org/reports/electricity-information-overview/electricity-production>. Citado na página 15.

KAUSEL, E. Early history of soil-structure interaction. *Soil Dynamics and Earthquake Engineering*, v. 30, n. 9, p. 822–832, 9 2010. ISSN 02677261. Citado na página 44.

KAWAI, H.; MICHISHITA, K.; DEGUCHI, A. Design wind loads on a wind turbine for strong wind. In: *BBAA VI International Colloquium on: Bluff Bodies Aerodynamics & Applications*. [S.l.: s.n.], 2008. Citado na página 33.

KREYSZIG, E. *ADVANCED ENGINEERING MATHEMATICS*. 10. ed. Hoboken, NJ: John WIley and Sons, 2011. ISBN 978-0-470-45836-5. Citado na página 74.

KWAK, H.-G.; FILIPPOU, F. C. *FINITE ELEMENT ANALYSIS OF REINFORCED CONCRETE STRUCTURES UNDER MONOTONIC LOADS*. Berkeley, 1990. Citado 2 vezes nas páginas 63 and 86.

LEE, J.; FENVES, G. L. PLASTIC-DAMAGE MODEL FOR CYCLIC LOADING OF CONCRETE STRUCTURES. *Journal of Engineering Mechanics*, n. 124, p. 892–900, 1998. Citado na página 64.

LOGAN, D. L. *A First Course in the Finite Element Method*. 6. ed. Boston, USA: Cengage Learning, 2016. Citado na página 78.

LUBLINER, J. et al. *A PLASTIC-DAMAGE MODEL FOR CONCRETE*. [S.l.], 1989. v. 25, n. 3, 299–326 p. Citado 2 vezes nas páginas 64 and 132.

MENIN, R. C. G.; TRAUTWEIN, L. M.; BITTENCOURT, T. N. Smeared Crack Models for Reinforced Concrete Beams by Finite Element Method Modelos de Fissuração Distribuída em Vigas de Concreto Armado pelo Método dos Elementos Finitos.

IBRACON Structures and Materials Journal, v. 2, n. 2, p. 166–200, 2009. Citado na página 73.

MILITITSKY, J. *Fundações de torres: aerogeradores, linhas de transmissão e telecomunicações*. 1. ed. São Paulo: Oficina de Textos, 2019. ISBN 978-85-7975-323-7. Disponível em: <https://www.ofitexto.com.br/livro/fundacoes-de-torres-aerogeradores-linhas-de-transmissao-e-telecomunicacoes/>. Citado na página 19.

MORAAL, J. R. *3D non-linear finite element modelling of an onshore wind turbine foundation*. Tese (Doutorado) — Delft University of Technology, Delft, 2019. Disponível em: <http://repository.tudelft.nl/.> Citado 2 vezes nas páginas 26 and 79.

OHTANI, Y.; CHEN, W.-F. MULTIPLE HARDENING PLASTICITY FOR CONCRETE MATERIALS. *Journal of Engineering Mechanics*, n. 114, p. 1890–1910, 1988. Citado na página 62.

PERRY, M. et al. Crack monitoring of operational wind turbine foundations. *Sensors (Switzerland)*, MDPI AG, v. 17, n. 8, 8 2017. ISSN 14248220. Citado 2 vezes nas páginas 30 and 33.

PHILLIPS, D. V.; ZIENKIEWICZ, O. C. FINITE ELEMENT NON-LINEAR ANALYSIS OF CONCRETE STRUCTURES. *Proceedings of the Institution of Civil Engineers*, v. 61, n. 1, p. 59–88, 1976. ISSN 1753-7789. Citado 3 vezes nas páginas 86, 87, and 90.

RAO, S. S. *The finite element method in engineering*. [S.l.: s.n.], 2018. ISBN 9780128117682. Citado 4 vezes nas páginas 79, 80, 81, and 85.

REBELLO, Y. C. P. *Fundações: guia prático de projeto, execução e dimensionamento*. 1. ed. [S.l.]: Zigurate, 2008. ISBN 8585570105. Citado na página 44.

REBELO, C. et al. Comparative life cycle assessment of tubular wind towers and foundations - Part 1: Structural design. *Engineering Structures*, Elsevier Ltd, v. 74, p. 283–291, 9 2014. ISSN 01410296. Citado na página 24.

REDDY, J. N. *Introduction to Nonlinear Finite Element Analysis*. 2. ed. [S.l.]: Oxford University Press, 2015. ISBN 978–0–19–964175–8. Citado 3 vezes nas páginas 87, 89, and 90.

RODRIGUES, H. B. *ESTUDO DE FUNDAÇÃO DIRETA DE AEROGERADORES COM MÉTODOS NUMÉRICOS*. Tese (Doutorado) — Universidade Federal de Santa Catarina, Florianópolis, 2019. Citado 7 vezes nas páginas 42, 45, 46, 47, 49, 50, and 53.

Sander David Cardoso Junior. *P-Calc V1.4.0*. –. Disponível em: <https://www.tqs.com.br/apps/p-calc/ejm1se496l>. Citado na página 51.

SHABAN, S. N. *TOWARDS THE DESIGN OF GRAVITY-BASED WIND TURBINE FOUNDATIONS*. Tese (Doutorado) — University of Toronto, Toronto, 2017. Citado 4 vezes nas páginas 25, 26, 50, and 51.

SIMULIA. *ABAQUS/Standard User's Manual, Version 2017*. Providence, RI: Dassault Systèmes Simulia Corp, 2017. Citado 11 vezes nas páginas 65, 67, 68, 69, 70, 96, 97, 101, 102, 104, and 108.

SORIANO, H. L. *Elementos Finitos - Formulações e Aplicação na Estática e Dinâmica das Estruturas.* Rio de Janeiro: Ciência Moderna, 2009. Citado na página 74.

SVENSSON, H. *Design of foundations for wind turbines*. Tese (Doutorado) — Lund University, 2010. Disponível em: <http://www.byggmek.lth.se>. Citado 7 vezes nas páginas 39, 40, 42, 47, 48, 57, and 73.

SZCZECINA, M.; WINNICKI, A. Relaxation Time in CDP Model Used for Analyses of RC Structures. In: *Procedia Engineering*. [S.l.]: Elsevier Ltd, 2017. v. 193, p. 369–376. ISSN 18777058. Citado na página 96.

UNFCCC. *Conference of the Parties (COP)*. 2021? Disponível em: <https://unfccc.int/process/bodies/supreme-bodies/conference-of-the-parties-cop>. Citado na página 14.

UNFCCC. *COP26 Reaches Consensus on Key Actions to Address Climate Change*. 2021. Disponível em: <https://unfccc.int/news/cop26-reaches-consensus-on-key-actions-to-address-climate-change>. Citado na página 14.

UNFCCC. Decision-/CP.26. Glasgow Climate Pact. In: *COP 26*. [s.n.], 2021. Disponível em: <https://unfccc.int/sites/default/files/resource/cop26_auv_2f_cover_decision.pdf>. Citado na página 14.

VELLOSO, D. d. A.; LOPES, F. d. R. *Fundações: critérios de projeto, investigação do subsolo, fundações superficiais, fundações profundas*. [S.l.]: Oficina de Textos, 2011. ISBN 9788579750137. Citado 2 vezes nas páginas 44 and 45.

Vestas. *Product brochure V90-1.8/2.0 MW*. [S.l.], 2009. Disponível em: <https://www.collgarwindfarm.com.au/wp-content/uploads/2015/01/Vestas_Product-brochure-V90-1.8-2.0MW-06-09-EN.pdf>. Citado 2 vezes nas páginas 39 and 40.

WHITTLESEY, R. Chapter 10 - Vertical Axis Wind Turbines: Farm and Turbine Design. In: *Wind Energy Engineering: A Handbook for Onshore and Offshore Wind Turbines*. [S.l.]: Academic Press, 2017. p. 185–202. Citado na página 21.

Wind Insider. *Vestas Secures 46 MW Order In South Korea With The Highest Tubular Steel Tower In The Country*. 2021. Disponível em: <https://windinsider.com/2021/06/22/vestas-secures-46-mw-order-in-south-korea-with-the-highest-tubular-steel-tower-in-the-country/>. Citado na página 24.

Wind turbine models. *Nordex N43 Lattice*. 2014. Disponível em: <https://en.wind-turbine-models.com/turbines/932-nordex-n43-lattice>. Citado na página 23.

ZHOU, X.; KONG, H.; DOW, J. S. Failure case study of reinforcedconcrete foundations of wind turbine towers. *Proceedings of the Institution of Civil Engineers: Forensic Engineering*, ICE Publishing, v. 168, n. 4, p. 158–166, 1 2015. ISSN 20439911. Citado 5 vezes nas páginas 33, 34, 38, 104, and 141.

ZIENKIEWICZ, O. C.; TAYLOR, R. L. *The Finite Element Method*. 6. ed. Oxford, UK: Elsevier, 2005. v. 1. Citado 3 vezes nas páginas 75, 77, and 85.